A STUDY OF THE GEOMETRIC HORIZON CONJECTURE AS APPLIED TO A BINARY BLACK HOLE MERGER

by

Jeremy Peters

Submitted in partial fulfillment of the requirements
for the degree of Master of Science

at

Dalhousie University
Halifax, Nova Scotia
Aug 14, 2020

Table of Contents

List of Figures . . . . . **iii**

Abstract . . . . . **vii**

Acknowledgements . . . . . **viii**

Chapter 1 Introduction **1**

1.1 Black Hole Horizons 1

1.2 Classification of the Weyl Tensor and Scalar Polynomial Invariants . . 2
1.2.1 Petrov Classification 2
1.2.2 Alignment Classification 4
1.2.3 SPIs 7

1.3 Statement of the Geometric Horizon Conjecture 9

1.4 Examples and Motivation for the Geometric Horizon Conjecture . . . 11

Chapter 2 Simulating a Binary Black Hole Merger **14**

2.1 Previous Work 14
2.1.1 Present Work 16

2.2 Overview of Figures 16

2.3 Figures 20

2.4 Discussion 106

Chapter 3 Conclusion **113**

Bibliography **116**

List of Figures

Figure 1 Plots of D_r, D_i, and |D| on a linear and log scale for time T = 0 23

Figure 2 Plots of D_r, D_i, and |D| on a linear and log scale for time T = 1 24

Figure 3 Plots of D_r, D_i, and |D| on a linear and log scale for time T = 2 25

Figure 4 Plots of D_r, D_i, and |D| on a linear and log scale for time T = 3 26

Figure 5 Plots of D_r, D_i, and |D| on a linear and log scale for time T = 4 27

Figure 6 Plots of D_r, D_i, and |D| on a linear and log scale for time T = 5 28

Figure 7 Plots of D_r, D_i, and |D| on a linear and log scale for time T = 6 29

Figure 8 Plots of D_r, D_i, and |D| on a linear and log scale for time T = 7 30

Figure 9 Plots of D_r, D_i, and |D| on a linear and log scale for time T = 8 31

Figure 10 Plots of D_r, D_i, and |D| on a linear and log scale for time T = 9 32

Figure 11 Plots of D_r, D_i, and |D| on a linear and log scale for time T = 10 33

Figure 12 Plots of D_r, D_i, and |D| on a linear and log scale for time T = 11 34

Figure 13 Plots of D_r, D_i, and |D| on a linear and log scale for time T = 12 35

Figure 14 Plots of D_r, D_i, and |D| on a linear and log scale for time T = 13 36

Figure 15 Plots of D_r, D_i, and |D| on a linear and log scale for time T = 14 37

Figure 16 Plots of D_r, D_i, and |D| on a linear and log scale for time T = 15 38

Figure 17 Plots of D_r, D_i, and |D| on a linear and log scale for time T = 16 39

Figure 18 Plots of D_r, D_i, and |D| on a linear and log scale for time T = 17 40

Figure 19 Plots of D_r, D_i, and |D| on a linear and log scale for time T = 18 41

Figure 20 Plots of D_r, D_i, and |D| on a linear and log scale for time T = 19 42

Figure 21 Plots of D_r, D_i, and |D| on a linear and log scale for time T = 20 43

Figure 22 Plots of D_r, D_i, and |D| on a linear and log scale for time T = 21 44

Figure 23 Plots of D_r, D_i, and |D| on a linear and log scale for time T = 22 45

Figure 24 Plots of D_r, D_i, and |D| on a linear and log scale for time T = 23 46

Figure 25 Plots of D_r, D_i, and |D| on a linear and log scale for time T = 24 47

Figure 26 Plots of D_r, D_i, and |D| on a linear and log scale for time T = 25 48

Figure 27 Plots of D_r, D_i, and |D| on a linear and log scale for time T = 26 49

Figure 28 Plots of D_r, D_i, and |D| on a linear and log scale for time T = 27 50

Figure 29 Plots of D_r, D_i, and |D| on a linear and log scale for time T = 28 51

Figure 30 Plots of D_r, D_i, and |D| on a linear and log scale for time T = 29 52

Figure 31 Plots of D_r, D_i, and |D| on a linear and log scale for time T = 30 53

Figure 32 Plots of D_r, D_i, and |D| on a linear and log scale for time T = 34 54

Figure 33 Plots of D_r, D_i, and |D| on a linear and log scale for time T = 38 55

Figure 34 Plots of D_r, D_i, and |D| on a linear and log scale for time T = 42 56

Figure 35 Plots of |D| vs y for fixed x ("slice plots") at time T = 12 and plots of locations of local minima of |D| along these selected constant x slice plots at x = 0 58

Figure 36 Plots of |D| vs y for fixed x ("slice plots") at time T = 12 and plots of locations of local minima of |D| along these selected constant x slice plots at x = 0.03125 59

Figure 37 Plots of |D| vs y for fixed x ("slice plots") at time T = 12 and plots of locations of local minima of |D| along these selected constant x slice plots at x = 0.125 60

Figure 38 Plots of |D| vs y for fixed x ("slice plots") at time T = 12 and plots of locations of local minima of |D| along these selected constant x slice plots at x = 0.28125 61

Figure 39 Plots of |D| vs y for fixed x ("slice plots") at time T = 12 and plots of locations of local minima of |D| along these selected constant x slice plots at x = 0.65625 62

Figure 40 Plots of |D| vs y for fixed x ("slice plots") at time T = 16 and plots of locations of local minima of |D| along these selected constant x slice plots at x = 0 63

Figure 41 Plots of |D| vs y for fixed x ("slice plots") at time T = 16 and plots of locations of local minima of |D| along these selected constant x slice plots at x = 0.0625 64

Figure 42 Plots of |D| vs y for fixed x ("slice plots") at time T = 16 and plots of locations of local minima of |D| along these selected constant x slice plots at x = 0.25 65

Figure 43 Plots of |D| vs y for fixed x ("slice plots") at time T = 16 and plots of locations of local minima of |D| along these selected constant x slice plots at x = 0.3125 66

Figure 44 Plots of |D| vs y for fixed x ("slice plots") at time T = 16 and plots of locations of local minima of |D| along these selected constant x slice plots at x = 0.5 67

Figure 45 Plots of |D| vs y for fixed x ("slice plots") at time T = 16 and plots of locations of local minima of |D| along these selected constant x slice plots at x = 0.75 68

Figure 46 Plots of |D| vs y for fixed x ("slice plots") at time T = 16 and plots of locations of local minima of |D| along these selected constant x slice plots at x = 1.0 69

Figure 47 Plots of |D| vs y for fixed x ("slice plots") at time T = 20 and plots of locations of local minima of |D| along these selected constant x slice plots at x = 0.125 70

Figure 48 Plots of |D| vs y for fixed x ("slice plots") at time T = 20 and plots of locations of local minima of |D| along these selected constant x slice plots at x = 0.375 71

Figure 49 Plots of |D| vs y for fixed x ("slice plots") at time T = 20 and plots of locations of local minima of |D| along these selected constant x slice plots at x = 0.5 72

Figure 50 Plots of |D| vs y for fixed x ("slice plots") at time T = 20 and plots of locations of local minima of |D| along these selected constant x slice plots at x = 0.625 73

Figure 51 Plots of |D| vs y for fixed x ("slice plots") at time T = 20 and plots of locations of local minima of |D| along these selected constant x slice plots at x = 0.75 74

Figure 52 Plotting all local minima from slice plots taken from Figures 35-51 at time T = 12 76

Figure 53 Plotting all local minima from slice plots taken from Figures 35-51 at time T = 16 77

Figure 54 Plotting all local minima from slice plots taken from Figures 35-51 at time T = 20 78

Figure 55 Plotting all local minima from slice plots taken from Figures 35-51 at time T = 24 79

Figure 56 Comparing plots of local minima along the x direction from Figures 52-56 with level 0.0003 sets of |D| at time T = 12 81

Figure 57 Comparing plots of local minima along the x direction from Figures 52-56 with level 0.0003 sets of |D| at time T = 16 82

Figure 58 Comparing plots of local minima along the x direction from Figures 52-56 with level 0.0003 sets of |D| at time T = 20 83

Figure 59 Comparing plots of local minima along the x direction from Figures 52-56 with level 0.0003 sets of |D| at time T = 24 84

Figure 60 Comparing plots of local minima along the x direction from Figures 52-56 with level–0 sets of D_r at time T = 12 86

Figure 61 Comparing plots of local minima along the x direction from Figures 52-56 with level–0 sets of D_r at time T = 16 87

Figure 62 Comparing plots of local minima along the x direction from Figures 52-56 with level–0 sets of D_r at time T = 20 88

Figure 63 Comparing plots of local minima along the x direction from Figures 52-56 with level–0 sets of D_r at time T = 24 89

Figure 64 Magnified Plots of Re{D^2}, Im{D^2}, D_r, and D_i for time T = 12 91

Figure 65 Magnified Plots of Re{D^2}, Im{D^2}, D_r, and D_i for time T = 16 92

Figure 66 Magnified Plots of Re{D^2}, Im{D^2}, D_r, and D_i for time T = 20 93

Figure 67 Magnified Plots of Re{D^2}, Im{D^2}, D_r, and D_i for time T = 24 94

Figure 68 Plotting the MOTSs of the initial BHs 96

Figure 69 Comparing the inner and outer MOTSs, which formed after bifurcation, with the initial two MOTSs of the BHs at time T = 19 98

Figure 70 Comparing the inner and outer MOTSs, which formed after bifurcation, with the initial two MOTSs of the BHs at time T = 20 99

Figure 71 Comparing the inner and outer MOTSs, which formed after bifurcation, with the initial two MOTSs of the BHs at time T = 21 100

Figure 72 Comparing the inner and outer MOTSs, which formed after bifurcation, with the initial two MOTSs of the BHs at time T = 22 101

Figure 73 Comparing the inner and outer MOTSs, which formed after bifurcation, with the initial two MOTSs of the BHs at time T = 23 102

Figure 74 Comparing the inner and outer MOTSs, which formed after bifurcation, with the initial two MOTSs of the BHs at time T = 24 103

Figure 75 Comparing the inner and outer MOTSs, which formed after bifurcation, with the initial two MOTSs of the BHs at time T = 25 104

Figure 76 Comparing the inner and outer MOTSs, which formed after bifurcation, with the initial two MOTSs of the BHs at time T = 26 105

Abstract

We study the algebraic structure of the Weyl tensor by tracing the level–0 set of the complex scalar polynomial invariant, D, through a numerical simulation of a quasi-circular binary black hole merger. We approximate the level–0 sets of D with level–ε sets of $|D|$ for small ε. We locate the local minima of $|D|$ and find that the positions of these local minima correspond closely to the level–ε sets of $|D|$ and we also compare with the level–0 sets of $\mathrm{Re}(D)$. The analysis provides strong evidence that the level–ε sets track a unique geometric horizon. By studying the behaviour of the zero sets of $\mathrm{Re}(D)$, $\mathrm{Im}(D)$ and their product, we observe that the level–ε set that best approximates this geometric horizon is given by $\varepsilon = 10^{-3}$.

Acknowledgements

This work was supported through Dalhousie University and Perimeter Institute. I would like to thank E. Schnetter for running the numerical simulations whose output was used to prepare the figures in this thesis and for useful discussions. I would like to thank A. A. Coley for supervising this project. I would also like to thank Perimeter Institute for hosting me as a summer student during the summer of 2019 through which I first met Erik, and for hosting me as a visitor in November 2019.

Chapter 1

Introduction

1.1 Black Hole Horizons

Black holes are solutions of general relativity and are most naturally characterized by the event horizon. The event horizon of a black hole (BH) is defined as the boundary of the causal past of future null infinity. Intuitively, this means that on one side of the event horizon, light cannot escape to null infinity. Notice that event horizons require knowledge of the global structure of space and time (one could say that the event horizon is a teleological object) [7, 8, 9]. However, for numerical relativity it is more convenient to use an initial value formulation of GR (a 3+1 approach), where initial data is given on a Cauchy hypersurface and is then evolved forward in time. This approach requires a local description of BH solutions [57, 56, 2, 3, 35, 32].

Let Σ be a compact spacelike 2D surface without border, and consider light rays leaving and entering Σ, with directions l and n, respectively. Let q_{ab} be the induced metric on Σ and denote the respective expansions as $\Theta_{(l)} = q^{ab}\nabla_a l_b$ and $\Theta_{(n)} = q^{ab}\nabla_a n_b$ [52]. Then, $\Theta_{(l)}$ and $\Theta_{(n)}$ are quantities which are positive if the light rays locally diverge, and negative if the light rays locally converge, and are zero if the light rays are locally parallel. We say that Σ is a *closed trapped surface* if $\Theta_{(l)} < 0$ and $\Theta_{(n)} < 0$ [46, 50, 47]. Σ is a marginally outer trapped surface (MOTS) if it has zero expansion for the outgoing light rays, $\Theta_{(l)} = 0$ [50, 47, 48, 54, 26, 33]. Σ is a future MOTS if $\Theta_{(l)} = 0$ and $\Theta_{(n)} < 0$ and a past MOTS if $\Theta_{(l)} = 0$ and $\Theta_{(n)} > 0$ [48]. The outermost MOTS is called the apparent horizon (AH) [50, 47, 48, 54, 26, 33]. A dynamical horizon (DH) is a smooth spacelike 3D submanifold of spacetime which is foliated by future MOTSs. [13, 7, 8, 9].

The above definitions serve as a quasi-local description of BHs [22, 21, 7, 8, 9]. For example, tracking an AH only requires knowledge of the intrinsic metric q_{ab} restricted to the spacetime hypersurface and the extrinsic curvature of that hypersurface at a given time [31, 9, 26]. Gravitational fields at the AH are correlated with gravitational

wave signals [31, 38, 37, 34, 33, 52], so AHs are useful to study gravitational waves. AHs are also used to numerically simulate binary BH (BBH) mergers and the collapse of a star to form a BH [12]. For example, the simulations that are used to analyze the gravitational wave data at LIGO use AHs [12, 28, 27]. DHs are also useful, as they could contribute to our understanding of BH formation [7, 8, 9, 12]. In addition, MOTSs turn out to be well-behaved numerically, and can be used to trace physical quantities of a BH as they evolve over time and through a BBH merger [54, 26, 33, 50, 51]. (This will be discussed in more detail in Chapter 2). One possible disadvantage of AHs is that the AHs observed depend on how the spacetime is foliated, so AHs are observer dependent [6].

It is conjectured that one can uniquely define a smooth, locally determined and foliation invariant horizon called the geometric horizon based on the algebraic (Petrov) classification of the Weyl tensor [22, 21]. This is the statement of the Geometric Horizon conjecture. The necessary conditions for the Weyl tensor to be of a certain Petrov type can be stated in terms of polynomials in the Riemann tensor and its contractions, which are called scalar polynomial invariants (or scalar curvature invariants) (SPIs). The Petrov classification (and more generally the alignment classification) of the Weyl tensor and the relevant SPIs are discussed in detail in the next section.

1.2 Classification of the Weyl Tensor and Scalar Polynomial Invariants

1.2.1 Petrov Classification

We describe the Petrov classification of the Weyl tensor. We assume a 4D spacetime. Consider the following decomposition of the Riemann tensor:

$$R_{abcd} = C_{abcd} + E_{abcd} + G_{abcd} \tag{1.1}$$

where C_{abcd} is the Weyl tensor, satisfying

$$C^{a}{}_{bad} = 0 \tag{1.2}$$

E_{abcd} is related to the traceless Ricci tensor, S_{ab} as [55]

$$E^{a}{}_{bad} = R_{ab} - \frac{1}{4} R g_{ab} \equiv S_{ab} \tag{1.3}$$

and G_{abcd} gives the remaining contribution, satisfying [55]:

$$G^{a}{}_{bad} = \frac{1}{4} g_{bd} R \tag{1.4}$$

(Note: the foregoing equations (1.1), (1.2), (1.3) and (1.4) can be generalized to higher dimensions by modifying the fraction, $\frac{1}{4}$). Being completely trace-free, the Weyl tensor has no relation to R_{ab}. Since the matter distribution in a given spacetime (T_{ab}) only affects the Riemann tensor via R_{ab} in the Einstein Field Equations, it follows that the matter distribution has no direct effect on the Weyl tensor. This means that the Weyl tensor is only affected by the spacetime geometry and not matter. Classifying the Weyl tensor then has a direct bearing on the classification of the ambient spacetime geometry. This tensor can be classified by its eigenvalues and eigenbivectors, according to the equation

$$\frac{1}{2} C_{abcd} X^{cd} = \lambda X_{ab} \tag{1.5}$$

Where X_{ab} is a bivector, which is a two-form and in 4D, the bivectors span a 6 dimensional space. It turns out that equation (1.5) can be brought to the equivalent form

$$Q_{ab} X^{b} = \lambda X_{a} \tag{1.6}$$

where Q_{ab} is presently represented as a complex, symmetric, traceless 3×3 matrix (so it has 5 independent degrees of freedom). The possible combinations of eigenvalues and normal forms for Q_{ab} in (1.6) can then be used to classify the Petrov types of the Weyl tensor. Based on this classification, there are five different Petrov types for the Weyl tensor in 4D: types **I**, **II**, **D**, **III**, **N** and **O**. See [55] for details. One can also obtain these Petrov types in 4D by considering the original eigenbivector problem, (1.5) and using the boost weight decomposition to simplify the form of the Weyl tensor.

One can obtain a similar algebraic classification for any symmetric trace free operator, say M_{ab}, by solving the eigenvalue problem, (1.6) for M_{ab} and then enumerating the possible combinations of repeated eigenvalues and normal forms of M_{ab}. One can also use the boost weight decomposition to define whether this M_{ab} is of algebraic type **I**, **II**, **D**, **III**, **N** and **O** which we shall utilize later. We can algebraically classify the symmetric traceless type 2 tensor, $M_{ab} = S_{ab}$, as above, where S_{ab} is the trace

free Ricci tensor given in equation (1.3). This is equivalent to the Segre classification [55].

An equivalent way of obtaining the Petrov types of the Weyl tensor is to classify the roots, E, of the equation

$$\mathbf{\Psi_0}' - 4E\mathbf{\Psi_1}' + 6E^2\mathbf{\Psi_2}' - 4E^3\mathbf{\Psi_3}' + E^4\mathbf{\Psi_4}' = 0 \tag{1.7}$$

where the scalars $\{\mathbf{\Psi_i}'\}_{i=0}^{4}$ are given by contracting C_{abcd} with the null tetrad, $(\mathbf{l}, \mathbf{n}, \mathbf{m}_2, \mathbf{m}_3)$, where $\mathbf{n}' = \bar{\mathbf{l}}'$ [55]. As proven by Penrose, this physically corresponds to principal null directions, $\mathbf{m}_3$, for which $\mathbf{\Psi_0} \equiv C_{abcd}m_3^a l^b m_3^c l^d = 0$ [55]. In terms of this characterization, C_{abcd} is of Petrov type **I** if there are 4 simple principal null directions (4 principal null directions of multiplicity 1), C_{abcd} is of Petrov type **D** if there are two double principal null directions, C_{abcd} is of Petrov type **II** if there is one double and two simple principal null directions, C_{abcd} is of Petrov type **III** if there is a triple principal null direction and a simple principal null direction, and Petrov type **N** if there is a quadruple principal null direction, and Petrov type **O** if $C_{abcd} = 0$ (i.e. the spacetime is conformally flat) [55].

1.2.2 Alignment Classification

The algebraic classification can be generalized to N dimensions [23, 24, 15, 43]. In N dimensions, we start with the frame of N-vectors, $\{\mathbf{l}, \mathbf{n}, \{\mathbf{m}_i\}_{i=2}^{N-1}\}$, where $\mathbf{l}$ and $\mathbf{n}$ are null, $\mathbf{l} \cdot \mathbf{n} = 1$, and the $\{\mathbf{m}_i\}$ are real, spacelike, mutually orthonormal, and span the orthogonal complement to the plane spanned by $\mathbf{l}$ and $\mathbf{n}$. The possible orthochronous Lorentz transformations are generated by null rotations about $\mathbf{l}$, null rotations about $\mathbf{n}$, spins (which involve rotations about $\mathbf{m}_i$), and boosts [43]. With respect to the given frame, boosts are given by the transformation

$$\begin{aligned} \mathbf{l} &\to \lambda \mathbf{l} \\ \mathbf{n} &\to \lambda^{-1}\mathbf{n} \\ \mathbf{m_i} &\to \mathbf{m_i} \end{aligned}$$

for all $i \in \{2, \ldots, N-1\}$ and for some $\lambda \in \mathbb{R}\backslash\{0\}$. (The remaining transformations are given in [23, 24, 15, 43].) Let $T_{a_1 \ldots a_p}$ be a tensor expressed with respect to this

frame. For a fixed set of indices $\{A_1, \ldots, A_p\}$ the resulting object, $T_{A_1 \ldots A_p}$, is denoted a *null-frame scalar*. If this scalar transforms under boosts as

$$T_{A_1 \ldots A_p} \to \lambda^b T_{A_1 \ldots A_p}$$

where $b = b_{A_1} + \ldots + b_{A_p}$, $b_0 = 1,\ b_1 = -1,\ b_i = 0\ \ \forall i \in \{2, \ldots N-1\}$, then we say that b is the *boost weight* of $T_{A_1 \ldots A_p}$. The *boost order* of the tensor T is the highest boost weight of each of its corresponding null frame scalars. Armed with these definitions, we may decompose the Weyl tensor into components organized by boost weight as follows [23, 24, 15]:

$$\begin{aligned} C_{abcd} = & \overbrace{4C_{0i0j} n^0_{\{a} m^i{}_b n^0_c m^j{}_{d\}}}^{+2} + \overbrace{8C_{010i} n^0_{\{a} l^1_b n^0_c m^i{}_{d\}} + 4C_{0ijk} n^0_{\{a} m^i{}_b m^j{}_c m^k{}_{d\}}}^{+1} \\ & + \overbrace{\begin{array}{l} 4C_{0101} n^0_{\{a} l^1_b n^0_c l^1_{d\}} + 4C_{01ij} n^0_{\{a} l^1_b m^i{}_c m^j{}_{d\}} \\ + 8C_{0i1j} n^0_{\{a} m^i{}_b l^1_c m^j{}_{d\}} + C_{ijkl} m^i_{\{\ a} m^j{}_b m^k{}_c m^l{}_{d\}} \end{array}}^{0} \\ & + \overbrace{8C_{101i} l^1_{\{a} n^0_b l^1_c m^i{}_{d\}} + 4C_{1ijk} l^1_{\{a} m^i{}_b m^j{}_c m^k{}_{d\}}}^{-1} + \overbrace{4C_{1i1j} l^1_{\{a} m^i{}_b l^1_c m^j{}_{d\}}}^{-2} \end{aligned} \tag{1.8}$$

where $a, b, c, d \in \{0, \ldots, N-1\},\ i, j, k, l \in \{2, \ldots, N-1\},\ T_{\{pqrs\}} = \frac{1}{2}(T_{[pq][rs]} + T_{[rs][pq]})$, and where we used the symmetries of the Riemann tensor, $R_{abcd} = R_{\{abcd\}}$, the algebraic Bianchi identity, and the trace free condition of the Weyl tensor.

It turns out that the leading term of the Weyl tensor (the term with the highest boost weight) is left unchanged by null rotations about $\mathbf{l}$, but is changed by all other orthochronous Lorentz transformations. Similarly, the trailing term of the Weyl tensor (the term with the lowest boost weight) is left unchanged by null rotations about $\mathbf{n}$, but is changed by all other orthochronous Lorentz transformations [23, 24, 15]. Hence, the boost weight of the leading component of the Weyl tensor (the boost order) is only determined by $\mathbf{l}$ and the boost weight of the trailing term of the Weyl tensor is only determined by $\mathbf{n}$.

We now list the possible algebraic types of the Weyl tensor for general N. The Weyl tensor (and hence the associated spacetime) is of alignment type **G** if for all $\mathbf{l}$ the boost order of C_{abcd} is $+2$ and for all $\mathbf{n}$ the lowest boost weight of the components of C_{abcd} is -2 (i.e. in (1.8) there will always be a boost weight $+2$ term and a boost

weight -2 term). The Weyl tensor is of alignment type 1 if there is a null vector $\mathbf{l}$ for which the boost order of C_{abcd} is $+1$ and for all $\mathbf{n}$ the lowest boost weight of the components of C_{abcd} is -2 (i.e. in (1.8) the $+2$ boost weight term can be made to vanish by a suitable frame choice). The Weyl tensor is of alignment type $(1,1)$ if there is a null vector $\mathbf{l}$ for which the boost order of C_{abcd} is $+1$ and there is a null vector $\mathbf{n}$ satisfying $\mathbf{l}\cdot\mathbf{n}=1$ and the lowest boost weight of the components of C_{abcd} is -1 (i.e. in (1.8) the $+2$ and -2 boost weight terms can be made to vanish by a suitable frame choice). The Weyl tensor is of alignment type 2 if there is a null vector $\mathbf{l}$ for which the boost order of C_{abcd} is 0 and for all $\mathbf{n}$ the lowest boost weight of the components of C_{abcd} is -2 (i.e. in (1.8) the $+2$ and $+1$ boost weight terms can be made to vanish by a suitable frame choice). The Weyl tensor is of alignment type $(2,1)$ if there is a null vector $\mathbf{l}$ for which the boost order of C_{abcd} is 0 and there is a null vector $\mathbf{n}$ satisfying $\mathbf{l}\cdot\mathbf{n}=1$ for which the lowest boost weight of the components of C_{abcd} is -1 (i.e. in (1.8) the $+2$, $+1$, and -2 boost weight terms can be made to vanish by a suitable frame choice). The Weyl tensor is of alignment type $(2,2)$ if there is a null vector $\mathbf{l}$ for which the boost order of C_{abcd} is 0 and there is a null vector $\mathbf{n}$ satisfying $\mathbf{l}\cdot\mathbf{n}=1$ for which the lowest boost weight of the components of C_{abcd} is also 0 (i.e. in (1.8) the $+2$, $+1$, and -2 and -1 boost weight terms can be made to vanish by a suitable frame choice). The Weyl tensor is of alignment type 3 if there is a null vector $\mathbf{l}$ for which the boost order of C_{abcd} is -1 and for all $\mathbf{n}$ the lowest boost weight of the components of C_{abcd} is -2 (i.e. in (1.8) the $+2$, $+1$ and 0 boost weight terms can be made to vanish by a suitable frame choice). The Weyl tensor is of alignment type $(3,1)$ if there is a null vector $\mathbf{l}$ for which the boost order of C_{abcd} is -1 and there is a null vector $\mathbf{n}$ satisfying $\mathbf{l}\cdot\mathbf{n}=1$ for which the lowest boost weight of the components of C_{abcd} is also -1 (i.e. in (1.8) the $+2$, $+1$, 0 and -2 boost weight terms can be made to vanish by a suitable frame choice). The Weyl tensor is of alignment type 4 if there is a null vector $\mathbf{l}$ for which the boost order of C_{abcd} is -2 and for all $\mathbf{n}$ the lowest boost weight of the components of C_{abcd} is also -2 (i.e. in (1.8) the $+2$, $+1$ and 0 and -1 boost weight terms can be made to vanish by a suitable frame choice). The Weyl tensor is of alignment type $\mathbf{O}$ if it vanishes identically. Because of the symmetric roles of $\mathbf{l}$ and $\mathbf{n}$ in (1.8), the foregoing completely characterizes all alignment types of the Weyl tensor [23, 24, 15, 43].

The alignment types of the Weyl tensor, **G**, 1, (1, 1), 2, (2, 1), (2, 2), 3, (3, 1), 4 and **O** are also labelled as **G**, **I**, $\mathbf{I}_i$, **II**, $\mathbf{II}_i$, **D III**, $\mathbf{III}_i$, **N** and **O**, respectively [43]. It turns out in 4D, type **G** does not exist, so for all null rotations of the null frame (and hence for all observers) the highest boost weight of the Weyl tensor is of type **II** and types **I** and $\mathbf{I}_i$, **II** and $\mathbf{II}_i$, **III** and $\mathbf{III}_i$ are pairwise equivalent. Hence, the alignment types of the Weyl tensor reduce to the Petrov types **I**, **II**, **D**, **III**, **N**, and **O** in 4D [23, 24, 15, 43].

Therefore, in a 4D spacetime, the Weyl tensor is said to be *algebraically general* if it is of Petrov type **I**. Otherwise, it is *algebraically special* (or *zeroth-order algebraically special*). The 4D spacetime itself is said to be algebraically general if its associated Weyl tensor is algebraically general (i.e. type **I**), and algebraically special otherwise. It is of particular interest to know whether a given 4D spacetime is of special algebraic type **II** or **D**. We can state the necessary conditions as discriminant conditions in terms of simple SPIs [22, 21, 17, 18]. One can also say that in 4D, any trace free and symmetric rank 2 tensor is is *algebraically general* if it is of algebraic type **I** and *algebraically special* otherwise, as described previously. Just as an SPI is a scalar obtained from a polynomial in the Riemann tensor and its contractions [22, 21], an SPI *of order* k is a scalar given as a polynomial in various contractions of the Riemann tensor and its covariant derivatives up to order k [22, 21]. It turns out that BHs are characterized by SPIs [16].

1.2.3 SPIs

The necessary discriminant conditions on trace-free (ans symmetric) ($s_1 = 0$) 4D Ricci tensor, S_{ab}, for this operator to be of type **II**/**D** are [16]:

$$\mathcal{D} \equiv {}^4D_4 = -s_3^2(4s_2^3 - 144s_2s_4 + 27s_3^2) + s_4(16s_2^4 - 128s_4s_2^2 + 256s_4^2) = 0, \qquad (1.9)$$

where

$$s_2 \equiv -\frac{1}{2}S^a{}_bS^b{}_a, \quad s_3 \equiv -\frac{1}{3}S^a{}_bS^b{}_cS^c{}_a, \quad s_4 \equiv \frac{1}{4}(2s_2^2 - S^a{}_bS^b{}_cS^c{}_dS^d{}_a). \qquad (1.10)$$

Similar conditions hold for any trace-free symmetric tensor T_{ab}.

Similarly, the necessary real conditions for the Weyl tensor to be of type **II**/**D** are [16]:

$$\mathcal{W}_1 \equiv -11W_2^3 + 33W_2W_4 - 18W_6 = 0, \qquad (1.11)$$

$$\mathcal{W}_2 \equiv (W_2^2 - 2W_4)(W_2^2 + W_4)^2 + 18W_3^2(6W_6 - 2W_3^2 - 9W_2W_4 + 3W_2^3) = 0, \quad (1.12)$$

where

$$W_2 = \frac{1}{8}C_{abcd}C^{abcd},\ W_3 = \frac{1}{16}C_{abcd}C^{cd}{}_{pq}C^{pqab},\ W_4 = \frac{1}{32}C_{abcd}C^{cd}{}_{pq}C^{pq}{}_{rs}C^{rsab},$$

$$W_6 = \frac{1}{128}C_{abcd}C^{cd}{}_{pq}C^{pq}{}_{rs}C^{rs}{}_{tu}C^{tu}{}_{vw}C^{vwab}. \quad (1.13)$$

We could also use the type **II**/**D** discriminant conditions for (1.5) directly, but these conditions turn out to be very long [22, 21]. A more practical alternative to obtain necessary type **II**/**D** discriminant conditions for the Weyl tensor is to form the symmetric trace-free operator,

$$T_a{}^e = C_{abcd}C^{ebcd} - 2W_2\delta_a{}^e \quad (1.14)$$

with W_2 as given in (1.13), and formulate the type **II**/**D** discriminant conditions for this operator in analogy with equation (1.9). To figure out whether the covariant derivatives of the Ricci tensor, $R_{ab;cd\ldots}$, are of type **II** or of type **D**, we can also form the associated operators and study their eigenvalues and eigenvectors.

Contracting the null tetrad,
$(\mathbf{l}, \mathbf{n}, \mathbf{m}_2, \mathbf{m}_3)$, with the Weyl tensor, C_{abcd}, one may form the complex scalars, $\boldsymbol{\Psi_0}, \boldsymbol{\Psi_1}, \boldsymbol{\Psi_2}, \boldsymbol{\Psi_3}, \boldsymbol{\Psi_4}$, and in terms of these scalars, as in the Newman-Penrose formalism, one may define

$$I = \boldsymbol{\Psi_0}\boldsymbol{\Psi_4} - 4\boldsymbol{\Psi_1}\boldsymbol{\Psi_3} + 3\boldsymbol{\Psi_2}^2 \quad (1.15)$$

$$J = \begin{vmatrix} \boldsymbol{\Psi_4} & \boldsymbol{\Psi_3} & \boldsymbol{\Psi_2} \\ \boldsymbol{\Psi_3} & \boldsymbol{\Psi_2} & \boldsymbol{\Psi_1} \\ \boldsymbol{\Psi_2} & \boldsymbol{\Psi_1} & \boldsymbol{\Psi_0} \end{vmatrix} \quad (1.16)$$

It can be shown that the two real conditions, (1.11) and (1.12), are equivalent to the real and imaginary parts of the following complex syzygy [55]:

$$D \equiv I^3 - 27J^2 = 0 \quad (1.17)$$

Thus for Petrov types **II** and **D**, (1.17) holds. It also turns out that for Petrov types **III**, **N**, and for **O**, we have $I = J = 0$, so (1.17) is satisfied trivially.

1.3 Statement of the Geometric Horizon Conjecture

Having discussed the Petrov classification, we now turn to the Geometric Horizon Conjecture (GHC). Given a spacetime, one could ask where in the spacetime the Weyl tensor is algebraically special and then define the geometric horizon as the set of such points. Since the vanishing of the SPIs, defined in (1.11) and (1.12), or (1.17) are necessary conditions for the Weyl tensor to be of Petrov type **II** or **D** (or even more algebraically special (i.e. type **III**, **N**, **D** or **O**), it follows that the set of points on which the Weyl tensor is algebraically special would be a (possibly improper) subset of the level–0 set of these invariants [22, 21]. The level–0 sets of these SPIs might not form a horizon with nice properties, however, as these SPIs could vanish additionally on axes of symmetry or fixed points of isometries [22, 21]. We know from (1.9), (1.11), and (1.12) that if the spacetime is of type **II** or **D**, then the given SPIs vanish. The GHC is given as follows [22, 21]:

GH Conjecture: *If a BH spacetime is zeroth-order algebraically general, then on the geometric horizon the spacetime is algebraically special. We can identify this geometric horizon using scalar curvature invariants.*

Comments: Note that when studying the GH conjecture, one would need to ensure that the geometric horizon exists and is unique. If the GH conjecture were true, then one could say that on this horizon, the Weyl tensor is algebraically special, which implies that the SPIs vanish, and one could also say that the level–0 sets of these SPIs completely characterize the geometric horizon. This horizon is foliation independent and quasi-local [22, 21]. In this thesis, we shall study the complex level–zero set of the invariant, $D = I^3 - 27J^2$, as given in (1.17), in 4D during a BBH merger. This could possibly help provide insight as to whether one can define a proper unique horizon based on the algebraic classification of the Weyl tensor. This conjecture might have to be modified so that instead of analyzing level–0 sets of the real SPIs, we analyze instead level–ε sets for small ε. However, further evidence from the anlysis of D_r below perhaps suggests that this is not the case. Such an ε could be determined by locating the local minima of the SPIs. We shall study the level–ε sets for $\varepsilon \in \{3 \times 10^{-4},\ 5 \times 10^{-4},\ 1 \times 10^{-3}\}$. In analogy to the MOTS, one can define

the geometrically outer trapped surface, the GOTS, where $\Theta_{(l)} = 0$, and $\Theta_{(n)} < 0$ for outgoing and ingoing null vectors on the geometric horizon, l and n, respectively [22, 21].

It may also be useful to study the algebraic properties of the covariant derivative of the Weyl tensor. There is a second part of the GHC that states that if a BH spacetime is algebraically special (so that on the Geometric Horizon the BH spacetime is automatically algebraically special), and if the first covariant derivative of the Weyl tensor is algebraically general, then on the geometric horizon, the covariant derivative of the Weyl tensor is algebraically special, and this Geometric Horizon can be identified as the level–0 set of certain differential SPIs [22, 21]. Differential SPIs are scalars obtained from polynomials in the Riemann tensor and its covariant derivatives and their contractions. This second part of the GHC can be applied to arbitrary covariant derivatives of the Weyl tensor so that the statement is one about the n^{th} covariant derivative of the Weyl tensor and its covariant derivative, the $(n+1)^{\text{st}}$ covariant derivative [22, 21]. It follows that by repeatedly taking covariant derivatives of the Weyl tensor, one can study the surfaces defined by the level–0 sets of many (differential) SPIs which may present a clearer picture of the Geometric Horizon.

In addition to algebraic and differential SPIs, one can also define and use Cartan invariants, which are constructed from the Riemann tensor and its covariant derivatives [42, 20]. More specifically, for a fixed set of frame vectors a *Cartan invariant* is a scalar that is obtained from the Weyl or Riemann tensor or any of its covariant derivatives by contracting the Weyl tensor (resp., any of its covariant derivatives) with the frame vectors. Thus, the Cartan invariants can be interpreted as the components of the Weyl tensor and its covariant derivatives. For example, the scalars $\{\mathbf{\Psi_i}\}$ as used in the definitions of I and J in (1.15) and (1.16) are Cartan invariants. Cartan invariants are easier to compute in general than SPIs, because they are linear in the Weyl tensor and its covariant derivatives. Furthermore, it was demonstrated that in 4D and 5D, one can construct other invariants from the Cartan invariants (extended Cartan invariants) which detect the event horizon of any stationary asymptotically flat ((anti) de Sitter) BH solutions [42, 20].

We next discuss applications of the GHC.

1.4 Examples and Motivation for the Geometric Horizon Conjecture

There are many examples to support the plausibility of the GHC [42, 20, 7, 8, 9]. A non-expanding horizon (NEH), Δ, is defined as a null surface with topology $S^2 \times \mathbb{R}$ for which any null normal l^a of Δ has vanishing expansion, $\Theta_l = 0$. This definition can be strengthened to define a weakly isolated horizon and further strengthened to define an isolated horizon [7, 8, 9]. It turns out that a Killing horizon is an isolated horizon [7, 8, 9]. For the Kerr metric, the event horizon and Killing horizon coincide, so the event horizon is an isolated horizon, and hence a non-expanding weakly isolated horizon. It can be proven, using the induced metric and induced covariant derivatives on the submanifold and assuming the dominant energy condition, that the Weyl and Ricci tensors are both of type **II/D** on a non-expanding weakly isolated null horizon [4, 40]. It can also be shown that the covariant derivatives of the Riemann tensor are also of type **II** on an NEH [22, 21].

The BH formed by a collapsing star approximates the Kerr geometry near the event horizon. Thus, there should be a horizon surrounding the event horizon for a collapsing BH that can be identified using the algebraic conditions on the Riemann tensor mentioned earlier. By continuity, the inside of the event horizon should also approximate the Kerr geometry, and the Kerr geometry admits an inner horizon. This inner horizon is shown to be a null surface, but is unstable, leading us to believe that the geometric horizon is unique at later times [7, 8, 9, 4, 40, 22, 21]. At earlier times, a bifurcation is possible, however [22, 21].

Recall that DHs are foliated by MOTSs, which are surfaces for which $\Theta_{(l)} = 0$ and $\Theta_{(n)} < 0$ for outgoing and ingoing normal null vectors, l and n, respectively. The GH conjecture applies to (and was in fact intended for) DHs. For example, BH solutions conformally related to stationary solutions and the imploding spherically symmetric metric are spacetimes that admit a geometric horizon. For the first example, and also for any dynamical spherically symmetric metric, the geometric horizon corresponds to marginally trapped tubes, but this isn't always the case, as the null vectors are not necessarily surface forming or geodesic [22, 21]. Additionally, the Vaidya spacetime for a given mass function provides an example of a spacetime which transitions from a DH to an isolated horizon, and it was proven that on isolated horizons the Weyl and Ricci tensor are of type **II/D** [55].

In addition to spherically symmetric dynamical models, non-spherically symmetric spacetimes could also admit geometric horizons [22, 21]. For example, consider the QS Szekeres dust models. A subset of these models could describe primordial BHs (PBHs). It turns out that these models admit an AH and, via the Cartan-Karlhede algorithm, this AH can be detected by a Cartan invariant [19]. Thus, this AH is a geometric horizon [22, 21].

Another example to support the GH conjecture comes from a family of exact closed universe solutions to the Einstein-Maxwell equations with a cosmological constant representing an arbitrary number of BHs, discovered by Kastor and Traschen (KT) [39]. Note that in this context, the term "merger" denotes two initially disjoint trapping surfaces forming one continuous boundary and the term "coalescence" describes the appearance of new marginal surfaces which enclose the original trapped surfaces [22, 21]. If coalescence does not occur, then the BHs remain apart, or they form a naked singularity (but this violates the cosmic censorship conjecture), so for a merger, coalescence does occur. For information on more than two BHs, see [45]. For the two-BH solution, see [39]. We consider a merger of two BHs. The evolving parameter is $\tau \in (-\infty, 0)$. Let $\mathcal{W}_1$, and $\mathcal{W}_2$ be the scalar polynomial invariants as defined in (1.11) and (1.12). As $\tau \to -\infty$, $\mathcal{W}_1 \to 0$, and there are two 3D disjoint geometric horizons forming around each BH [22, 21]. It turns out that $\mathcal{W}_2 = 0$, but $\mathcal{W}_1 = 0$ only at the coordinate positions of each of the BHs, $r_i = 0$, along certain segments of the symmetry axis, and along a 2D cylindrical surface [22, 21]. As τ increases, the distance between the coordinate positions of the BHs decrease and there is some measure of "closeness" of the BHs, which approaches 0. The 2D cylinder expands to engulf the two BHs as they coalesce. As $\tau \to 0^-$, $\mathcal{W}_1 \to 0$, and the spacetime then settles down to a type **D** Reissner-Nordstrom-de-Sitter BH spacetime with mass $M = m_1 + m_2$. This final spacetime turns out to have a geometric horizon [42, 20]. So a geometric horizon forms at the beginning and end of the coalescence.

During the intermediate process, there are 3D surfaces located at a finite distance from the axis of symmetry for which the traceless Ricci tensor (and hence the Ricci tensor, R_{ab}) is of algebraic type **II**/**D**. There is also evidence of a minimal 3D dynamically evolving surface where $\mathcal{W}_1$ assumes a constant minimum value. This suggests that there is a geometric horizon during the dynamical regime between the spacetimes

[22, 21], but further investigation is needed.

The KT solution for multiple BHs was studied and geometric horizons around each BH were found in [41]. The results were compared with the previously mentioned 2-BH solution. Additionally, three black-hole solutions were studied and geometric horizons were found around these BHs also [22, 21].

Chapter 2

Simulating a Binary Black Hole Merger

We wish to study the behaviour of the complex SPI, $D = I^3 - 27J^2$, as defined in (1.17), through a BBH merger. Since the Kerr geometry is type **D** everywhere, it follows that $D = 0$ everywhere for a Kerr BH. It is also known that in a BBH merger, the merged BHs at late times settle down to a solution well described by the Kerr metric [22, 21]. Thus, for a merger of 2 initially Kerr BHs, a plot of the real part and imaginary part of D should be roughly zero everywhere at early and late times. However, in the intermediate "dynamical" region (during the actual merger and coalescence at intermediate times), these same zero plots should yield important information. This is what we wish to study in this thesis. We first highlight some known features of a BBH merger, as shown by [50, 51, 31].

2.1 Previous Work

The evolution of MOTS during the intermediate stages of a BBH merger was studied in [50, 51]. Event horizons have been used to study a BBH merger, and could possibly motivate the "pair-of-pants" picture of a BBH merger (possibly only at early and late times) [50, 51, 30]. However, event horizons are not useful to study physical properties as they evolve through the merger. MOTSs and AHs are much more useful in studying a BBH merger [46], and it is known that MOTSs and AHs can be used determine and track the time evolution of physical properties of a BH, such as such as mass, and angular momentum [50, 36, 31, 38, 37, 34, 26, 33, 9, 52].

In both [50, 51] and in [31], a head-on collision of unequal mass BHs was numerically simulated. In [50, 51], it was found that there is a connected sequence of MOTSs, which interpolate between the initial and final states of the merger (two separate BHs to one BH, respectively) [50, 51]. The MOTS were found using a horizon finder, which is a robust method for detecting the MOTSs based on the principal eigenvalues of the stability operator [50, 51, 2, 3, 1, 49]. This interpolating sequence

of MOTSs allows physical BH quantities to be traced through the merger. In [31, 14], the dynamics of the head-on collision was studied by modelling the two initial BHs as spacetime punctures and the initial BH separations and mass ratios were varied. The AHs of the initial BHs in the simulations were used to track the location and properties of the BH punctures [31]. Both [50, 51] and [31] have described the structure of the MOTSs through the merger in detail. Initially, there are two BHs with disjoint MOTS (which are AHs at this point [31]), $\mathcal{S}_1$, and $\mathcal{S}_2$, one around each BH. Then, as the two BHs evolve, a common MOTS forms around the two separate BHs and bifurcates into an inner MOTS, $\mathcal{S}_i$, which surrounds the MOTS and an outer MOTS, $\mathcal{S}_c$. (This demonstrates the well-known fact that a single foliation can have up to 4 MOTSs [31, 50, 51, 49, 54, 26, 33]). The outer MOTS $\mathcal{S}_c$, increases in area, encloses the three inner MOTS, $\mathcal{S}_1$, $\mathcal{S}_2$, and $\mathcal{S}_i$, and eventually forms the AH of the common BH after the merger has taken place [31, 50, 51]. The fate of this common AH is well understood [31, 8, 54, 5, 33]. The inner MOTS, $\mathcal{S}_i$, decreases in area and approaches the inner MOTS $\mathcal{S}_1$ and $\mathcal{S}_2$ [31, 50, 51]. This bifurcation and the three inner MOTS, $\mathcal{S}_1$, $\mathcal{S}_2$, and $\mathcal{S}_i$ have also been well studied [31, 8, 54, 5, 33, 50, 51, 36, 44, 49]. In [31], it was found that at late times, $\mathcal{S}_1$ and $\mathcal{S}_2$ continued to exist and intersected in general but remained separate horizons. The BH punctures, while acting effectively as a single puncture, did not completely merge [31]. In [50, 51], it was found that at the time when the inner surface touched the two individual BHs, the inner MOTS displayed self-intersections and thus a topology change, and a slight area increase. Modulo this area increase, it was shown [50] that

$$A_1 + A_2 \leq A_{\text{inner}} \leq A_{\text{outer}}$$

where $A_{1,2}$ are the areas of the original MOTS, and A_{inner} is the area of the inner common MOTS, A_{outer} is the area of the outer MOTS and thus the final BH MOTS. This merger provides a route to proving the Penrose inequality for multiple BHs via the Penrose inequality for one BH [50]:

$$A \leq 16\pi M_{\text{adm}}^2$$

It was also noted that if the initial separations are small enough and the lapse funtion is properly behaved, then the two initial MOTS $\mathcal{S}_1$ and $\mathcal{S}_2$ are approximately null surfaces [54, 26, 33], and hence isolated horizons [31].

2.1.1 Present Work

Instead of studying a head-on collision, in this thesis we shall study a quasi-circular orbit of two merging, equal mass and non-spinning BHs, simulated by E. Schnetter. This simulation has not been presented elsewhere and the results of this simulation are new. In these simulations, the Einstein toolkit infrastructure was used [29] and the simulations are run using 4^{th} order finite differencing on an adaptive mesh grid, with adaptive refinement level of 6 [53, 11]. E. Schnetter used Brill-Lindquist initial data with BH positions and momenta set up to satisfy the QC-0 initial condition [25]. Instead of analyzing a sequence of MOTS throughout the merger, we seek to define and study a geometric horizon as it evolves through the merger, in accordance with the GHC. Since (1.17) sets necessary conditions for the Weyl tensor to be of algebraic type **II**, we seek to analyze the constant contours of the difference $D = I^3 - 27J^2$. In the simulations, the real and imaginary parts of I and J are calculated using the Cartan invariants, $\{\mathbf{\Psi}_i\}_{i=0}^5$, as given in equations (1.15) and (1.16), and the calculations are carried out using the orthonormal fiducial tetrad, as given by [10]. For comparison, we also plot the centroid and average radius of the AHs of the two initial BHs. We have also verified that it is valid to approximate the AH as spherical surface.

2.2 Overview of Figures

Figures 1–34 provide contour plots of the real part, imaginary part, and magnitude of $D = I^3 - 27J^2$ on a linear and log scale (see (1.17)) viewed as a function on $[-1.5, 1.5] \times [-1.5, 1.5] \times \{0.03125\}$, over selected instances of the time parameter, $T \in [0,\ 30] \bigcup \{34,\ 38,\ 42\}$. In each figure (and in Figures 35–68), the data obtained for $x > 0$ was rotated by 180 degrees about the $x = y = 0$ axis to obtain the data for $x < 0$. In each figure, the overlaid deep pink contours on the plots for the real part of D (D_r, pictured at the bottom left of each frame) are the level–0 sets of D_r. Similarly, the overlaid deep pink contours on the plots for the imaginary part of D, (D_i, pictured at the bottom right of each frame) are the level–0 sets of D_i. Since $|D|$ is positive definite, the level–0 sets of $|D|$ sets are impossible to find precisely due to discrete resolution and numerical error. Instead, we highlight the evolution of the level–ε sets, where $\varepsilon \in \{3 \times 10^{-4},\ 5 \times 10^{-4},\ 1 \times 10^{-3}\}$. The overlaid red contours of

the linear and log scale magnitude of D, ($|D|$, pictured at the top left and top right of each frame) are the level–5×10^{-4} sets. The overlaid green and white contours on the log scale plots of $|D|$ (upper right of each frame) are the level–3×10^{-4} and 1×10^{-3} sets, respectively. The blue dots in Figures 1–34 give the centroids of the MOTSs of the two initial BHs as they evolve, and serve to track the positions of these BHs through the merging process. The blue circles in the upper right–hand plots in Figures 1–34 give the (x, y) coordinates corresponding to $z = 0.03125$ of the sphere centred at the centroids of the MOTS and whose radius is equal to the average radius of the MOTSs of the initial BHs ("radius averaged" MOTSs). In the upper right plot (the plot for $|D|$) in each of Figures 1–34, the data for D_r and D_i was "cut off" to lie in the range $[-1, 1]$ in the sense that for any point $\mathbf{x_0}$ in the domain, if $D_r(\mathbf{x_0}) > 1$ (resp. $D_i(\mathbf{x_0}) > 1$), then we have set $D_r(\mathbf{x_0}) = 1$ (resp. $D_i(\mathbf{x_0}) = 1$). This means that any data for D whose real (resp. imaginary) part lies in the range $[-1, 1]$ has an unaltered real (resp. imaginary) part, but any data whose real (resp. imaginary) part does not lie in the range $[-1, 1]$ is recorded as 1 if the real (resp. imaginary) part is positive, and -1 if the real (resp. imaginary) part is negative. This process was done to suppress high values of D_r and D_i, and $|D|$ in the plots to make them clearer. Similarly, for Figures 64–67, the data for D_r, D_i, and the real and imaginary part of D^2 was cut off to lie in the range $[-1, 1]$. However, the level–0 and level–ε sets are unaltered by this "cutoff" procedure, since in all cases, $\varepsilon < 1$.

In order to investigate further the level–0 sets of $|D|$, we examine 1D plots of $|D|$ as functions of y for fixed x henceforth referred to as "slice plots". Each of Figures 35–51 highlight the slice plots of $|D|$ for a fixed value of x at a fixed time T, where $T \in \{12,\ 16,\ 20,\ 24\}$. Each of the upper plots in Figures 35–51 are contour plots of $|D|$ vs x and y with the level–3×10^{-4}, 5×10^{-4} and 1×10^{-3} contours in green, red and white, respectively, and the blue points mark the positions of the centroids of the MOTSs, as before. In these upper plots, the local minima of $|D|$ when viewed along these slice plots are recorded as green points. In each of Figures 35–51, the lower plots give directly the 1D slice plots of $|D|$ vs y, whose x position and time T is indicated. These slice plots are given at various resolutions to locate the local minima of $|D|$ and highlight the behaviour of $|D|$ in this region. In at least one of these plots, the behaviour of $|D|$ vs y in the range $[0, 1.2 \times 10^{-3}]$ is indicated for comparison with

the level–ε sets for $\varepsilon \in \{3 \times 10^{-4},\ 5 \times 10^{-4},\ 1 \times 10^{-3}\}$.

Figures 52–55 record the contour plots of $|D|$ at times $T = 12,\ 16,\ 20,\ 24$, respectively in the upper left and right–hand corners, along with the green, red and white level–$3 \times 10^{-4},\ 5 \times 10^{-4}$ and 1×10^{-3} sets of $|D|$, respectively and the blue MOTS centroids. In each of Figures 52–55 in the upper left–hand corner, we plot with green points all local minimum points of $|D|$ vs y taken among all slice plots of fixed x at a fixed time, T (i.e. the union of all green points recorded in the upper Figures 35–51). The upper right–hand plots of $|D|$ in each of Figures 52–55 are the same as the upper left–hand plots except instead of considering all slice plots D vs y taken over constant x, we find and plot with green points the local minima of $|D|$ vs x for a fixed y. For comparison, the lower plots record the 3D contour plots of D_r with its associated deep pink level–0 sets and blue MOTS centroids, as in the lower left–hand plots of Figures 1–34.

Figures 56–59 give the contour plots of $|D|$ at times $T = 12,\ 16,\ 20$, and 24, respectively, with green level–3×10^{-4} sets of $|D|$, white level–1×10^{-3} sets of $|D|$ and the blue points marking the MOTS centroids. The green points record the local minima of $|D|$ along all slice plots of $|D|$ vs y for all fixed x whose corresponding values of $|D|$ lie in the range $[1 \times 10^{-4},\ 1.2 \times 10^{-3}]$. The upper plot of each figure is of original resolution, and the lower plot is zoomed in to highlight the relative positions of the local minima of $|D|$ and the green level–3×10^{-4} sets.

In Figures 60–63, the local minima of $|D|$ are plotted in green points along with the deep pink level–0 sets of D_r at times $T = 12,\ 16,\ 20$, and 24, respectively. The blue MOTS centroids are plotted for reference. The upper plot of each figure is of original resolution, while the lower plot is zoomed in to highlight the relative positions of the local minima of $|D|$ and the deep pink level–0 sets of D_r near the origin.

In order to gain more information on the geometric horizons, we plot quantities which change sign through zero. Figures 64–67 highlight the level contours of the real and imaginary part of D^2, (given by $\mathrm{Re}(D^2) = D_r^2 - D_i^2$ and $\mathrm{Im}(D^2) = 2 * D_r * D_i$, respectively), along with plots of D_r and D_i for selected instances of time. Figures 64–67 correspond to times $T = 12,\ 16,\ 20$ and 24, respectively. The upper left figure, upper right figure, middle left figure, and middle right figure of each of Figures 64–67 show a magnified contour plot of $\mathrm{Re}(D^2)$, $\mathrm{Im}(D^2)$, Dr, and Di, respectively. In each

of these four figures, the level–1×10^{-3} sets of $|D|$ are plotted in white, and the level–-0.01 and level–$+0.01$ sets of the quantities in question are given by the yellow and lime green contours, respectively. The lower left and lower right figures also provide magnified contour plots of D_r and D_i, respectively, with the saddle brown level–-0.1 sets, yellow level–-0.01 sets, lime green level–$+0.01$ sets, and cyan level–$+0.1$ sets of the quantities being plotted. In all six plots of Figures 64–67, the quantities being plotted were cut off to lie between $[-1, 1]$, so that the black regions correspond to where the quantities attain a value of 1 and the white regions correspond to where the quantities attain a value of -1.

In the upper right–hand plots of Figures 1–34, the MOTS was approximated as a spherically symmetric surface. Figure 68 compares the "radius averaged" MOTS, as plotted in Figures 1–34 with points corresponding to the "actual" MOTS. Both data sets are provided by E. Schnetter. The upper left, upper right, lower left and lower right plots of Figure 68 are plots of $|D|$ at times $T = 12,\ 16,\ 20$, and 24, respectively with the "radius averaged" and "actual" MOTS outline and centres overlaid in each plot. The blue contours in each frame of Figure 68 are constant z slices of the "radius averaged" MOTSs. The blue point indicates the x and y positions of the centroid of the MOTS. The sky blue points track for better illustration the centroid of the MOTS and points on the "actual" MOTS whose z coordinate values lie in the range $[0.02, 0.04]$.

It should be noted that during the BBH merger, the MOTSs of the initial BHs start out as AHs and then evolve into MOTS, which are no longer AHs. This is because a third MOTS appears and bifurcates into two surfaces, each of which surrounds the (former) AHs of the initial BHs. This has been previously noted and is described in [50, 51, 31]. The outermost of these two surfaces then forms the AH of the merged BH spacetime. In the simulation studied here, the bifurcation occurs between $t = 18$ and $t = 19$, so it is after this time that the AHs are demoted to ordinary MOTSs. These inner and outer "common" surfaces that form and surround the initial BH MOTSs are plotted in Figures 69–76 from times $T = 19$ (after the bifurcation) to $T = 26$. In Figures 69–76, we plot $|D|$ on a log scale at these aforementioned times and superimpose the white level–1×10^{-3} sets of $|D|$ with the blue radius averaged initial BH MOTSs and light sky blue points on the initial BH MOTSs from the exact

calculation. The purple dots in the upper (resp. lower) panel of each figure denote the points on the inner (resp. outer) MOTSs from the exact calculation that forms after the bifurcation whose corresponding z values lie in the range $[-0.1, 0.1]$.

2.3 Figures

Figures 1-34: Plots of D_r, D_i, and |D| on a linear and log scale for times T = 0,…,30, 34, 38, 42.

Note:

- $D = I^3 - 27J^2$
- I and J are scalar curvature invariants of the Riemann Tensor (see main text).
- $D_r = \mathrm{Re}\{D\}$
- $D_i = \mathrm{Im}\{D\}$
- $|D| = |D_r + i * D_i| = \sqrt{{D_r}^2 + {D_i}^2}$
- In the plots for Dr, Di and the linear-scale plot for |D| in Figures 1-34, the values of Dr and Di are cut off to lie in the range [-1,1]. The data for the log-scale plot for |D| is not cut off, however. See main text for details.

Legend for Figures 31-34:

- Upper Left: |D| on a log scale
- Upper Right: |D| on a linear scale
- Lower Left: Dr
- Lower Right: Di
- Green contours: Level 0.0003 sets

- Red contours: Level 0.0005 sets
- White contours: Level 0.001 sets
- Blue circles: “Radius averaged” MOTSs of initial BHs
- Blue dots: Centroids of MOTSs of initial BHs
- Deep pink contours: Level 0 sets

Figure 1: T = 0.

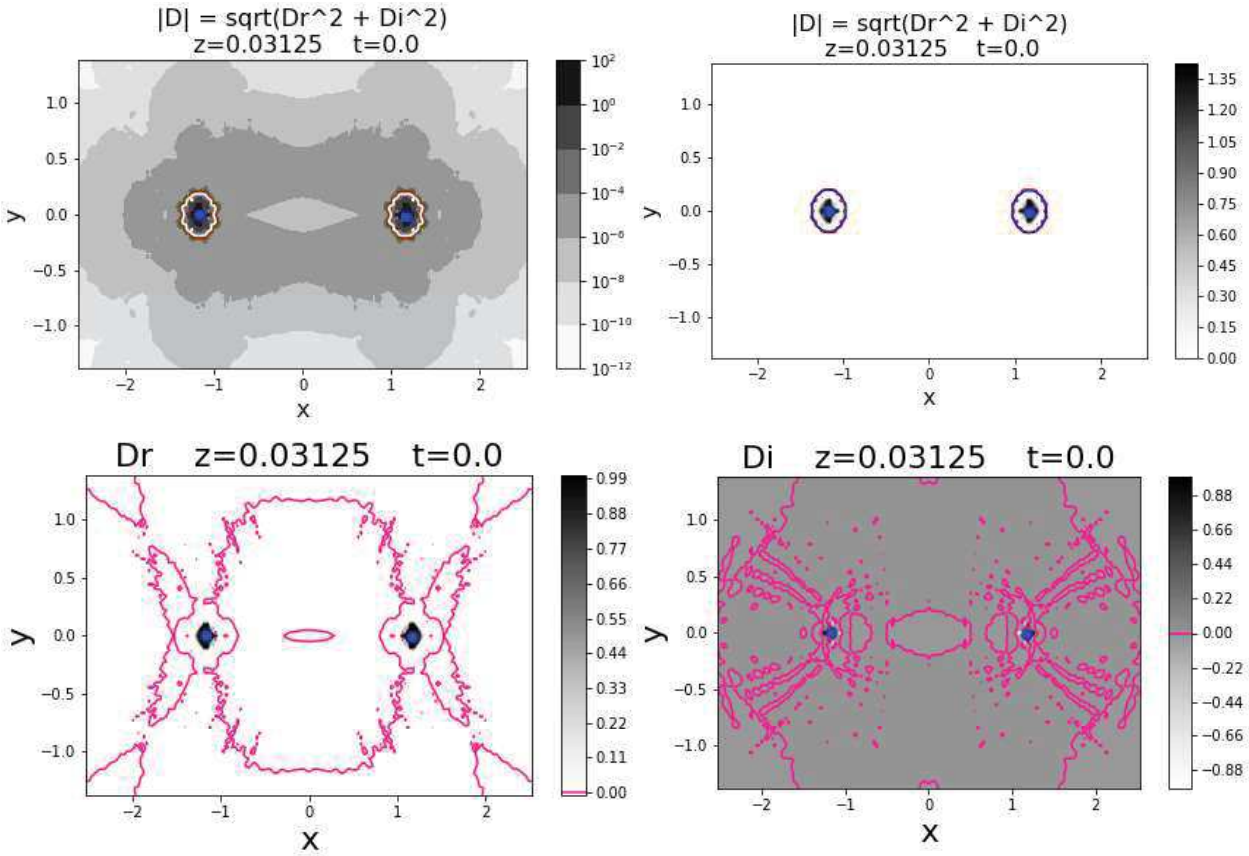
|D| = sqrt(Dr^2 + Di^2)
z=0.03125 t=0.0
|D| = sqrt(Dr^2 + Di^2)
z=0.03125 t=0.0
Dr z=0.03125 t=0.0
Di z=0.03125 t=0.0
x
y

Figure 2: T = 1

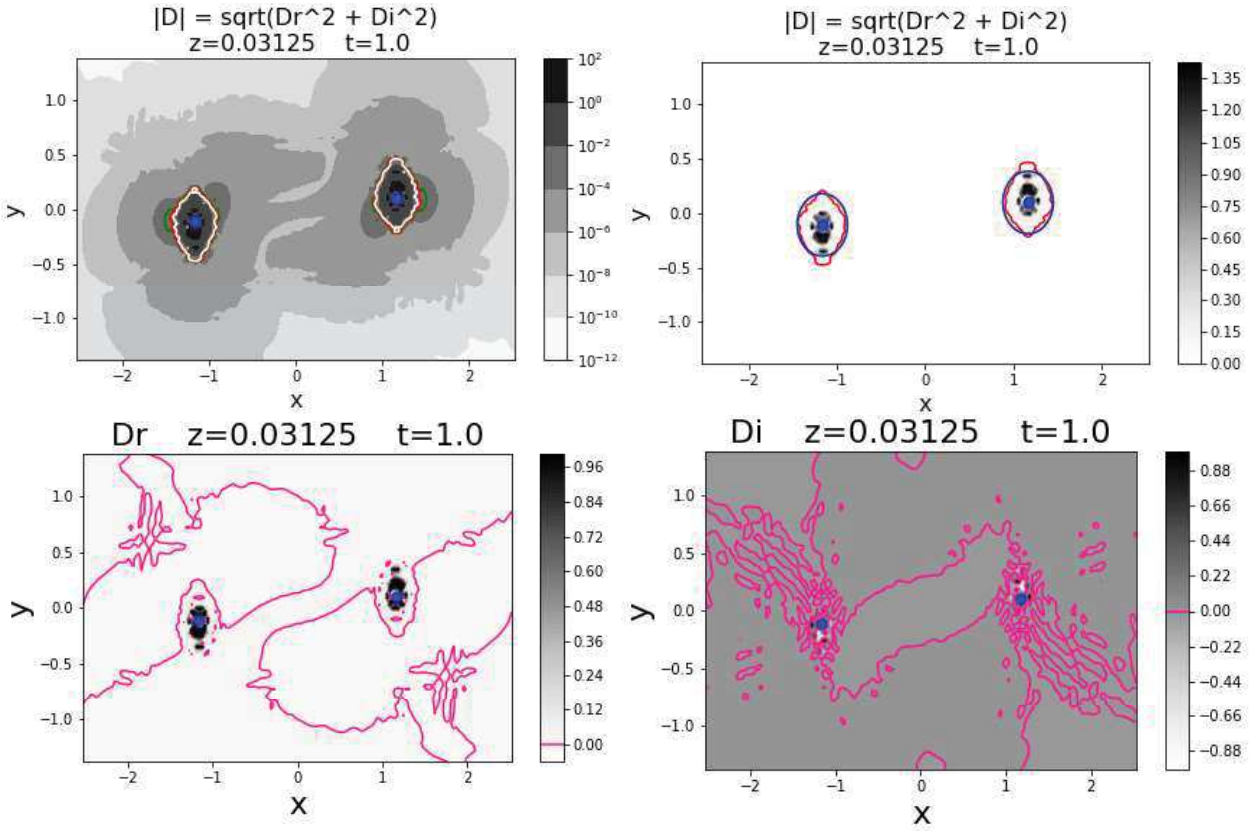
|D| = sqrt(Dr^2 + Di^2)
z=0.03125 t=1.0
|D| = sqrt(Dr^2 + Di^2)
z=0.03125 t=1.0
Dr z=0.03125 t=1.0
Di z=0.03125 t=1.0
x
y

Figure 3: T = 2

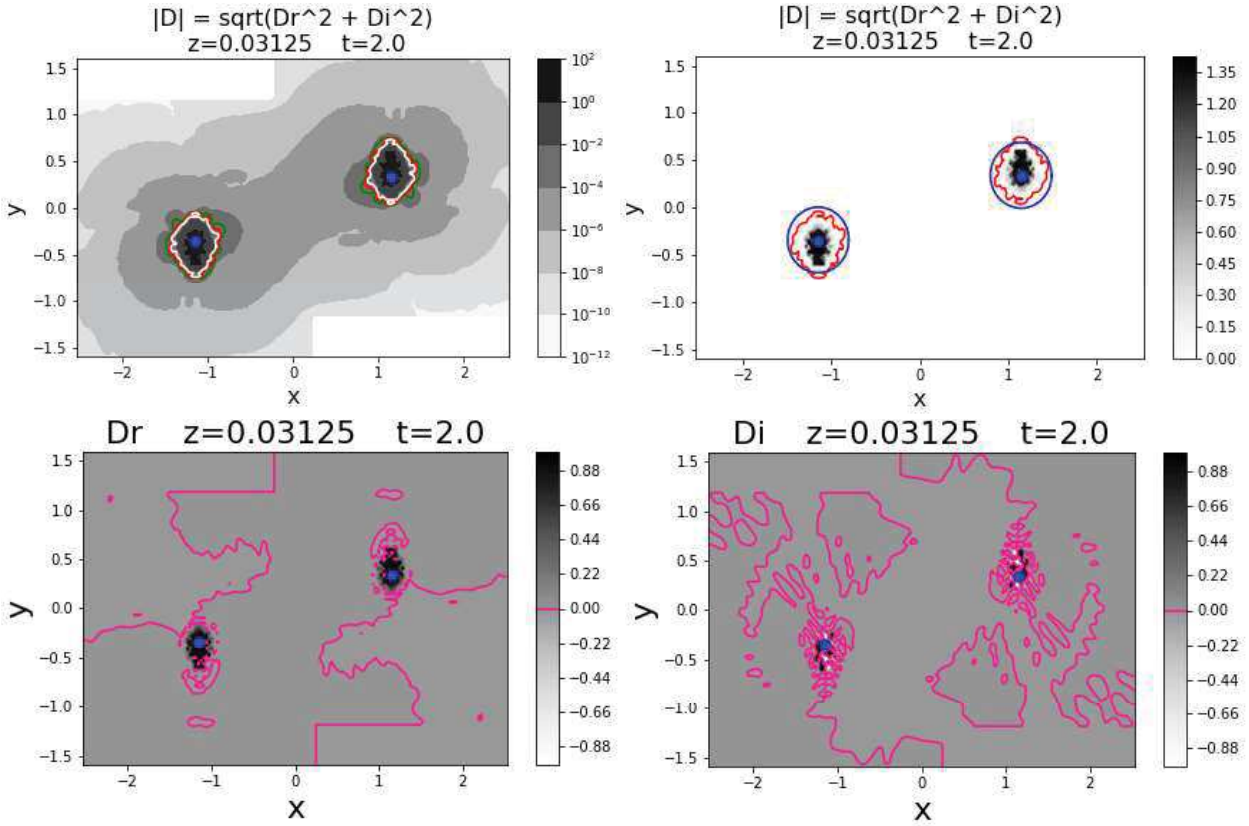
|D| = sqrt(Dr^2 + Di^2)
z=0.03125 t=2.0
|D| = sqrt(Dr^2 + Di^2)
z=0.03125 t=2.0
Dr z=0.03125 t=2.0
Di z=0.03125 t=2.0
x
y

Figure 4: T = 3

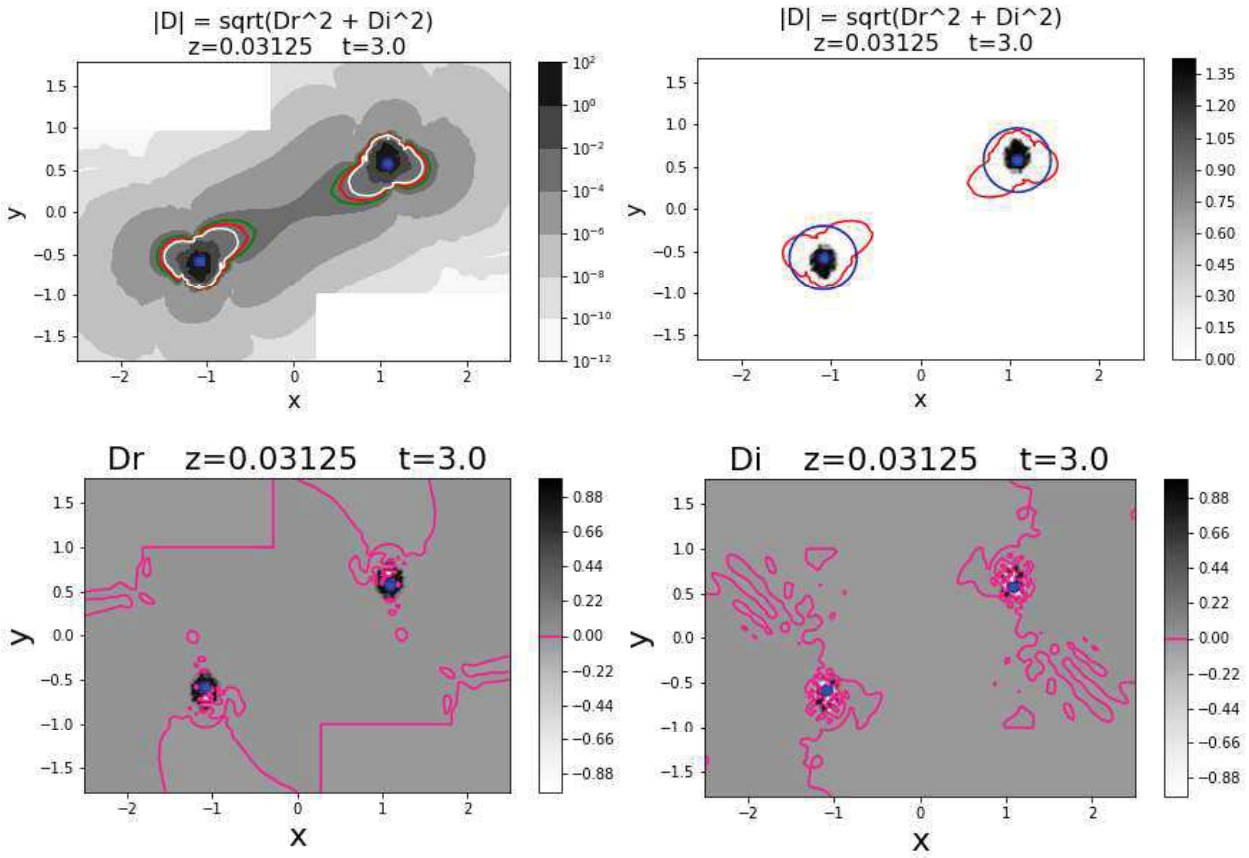
|D| = sqrt(Dr^2 + Di^2)
z=0.03125 t=3.0
|D| = sqrt(Dr^2 + Di^2)
z=0.03125 t=3.0
Dr z=0.03125 t=3.0
Di z=0.03125 t=3.0
x
y

Figure 5: T = 4

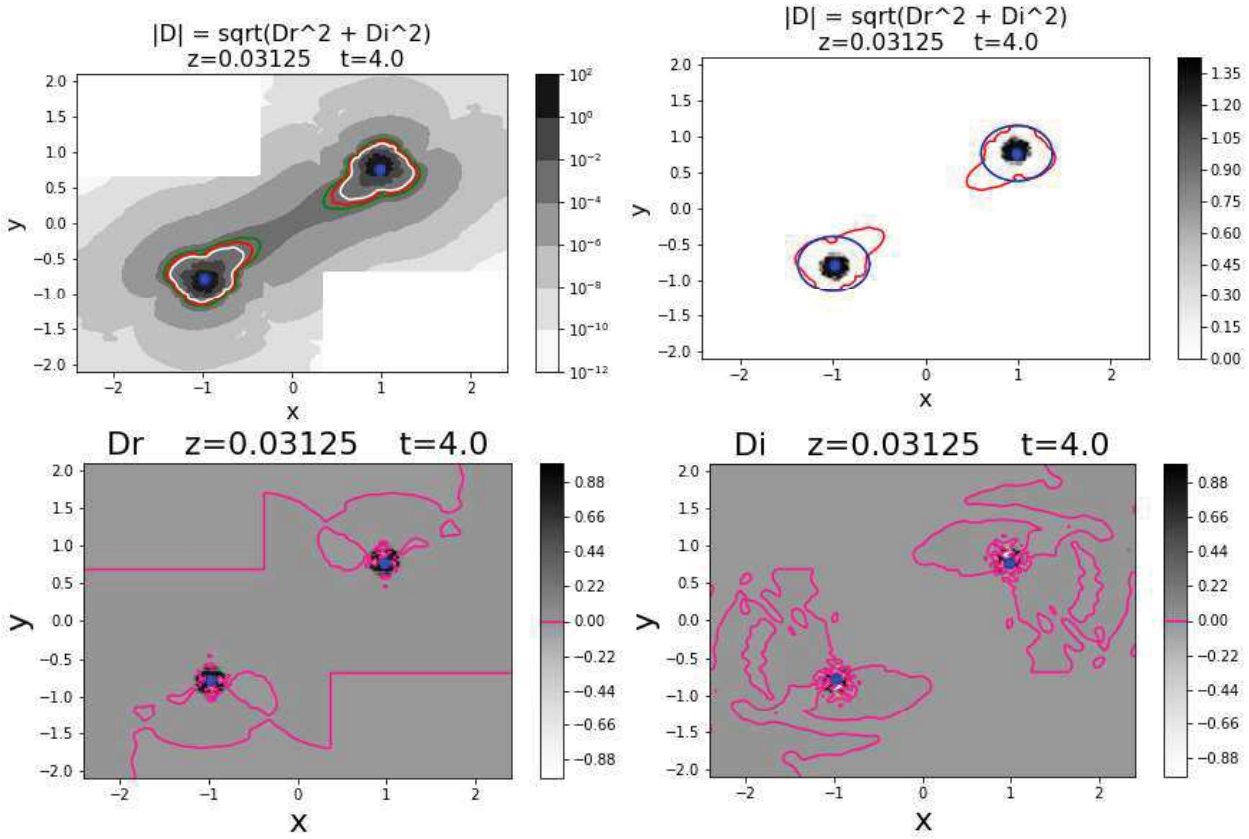
|D| = sqrt(Dr^2 + Di^2)
z=0.03125 t=4.0
|D| = sqrt(Dr^2 + Di^2)
z=0.03125 t=4.0
Dr z=0.03125 t=4.0
Di z=0.03125 t=4.0
x
y

Figure 6: T = 5

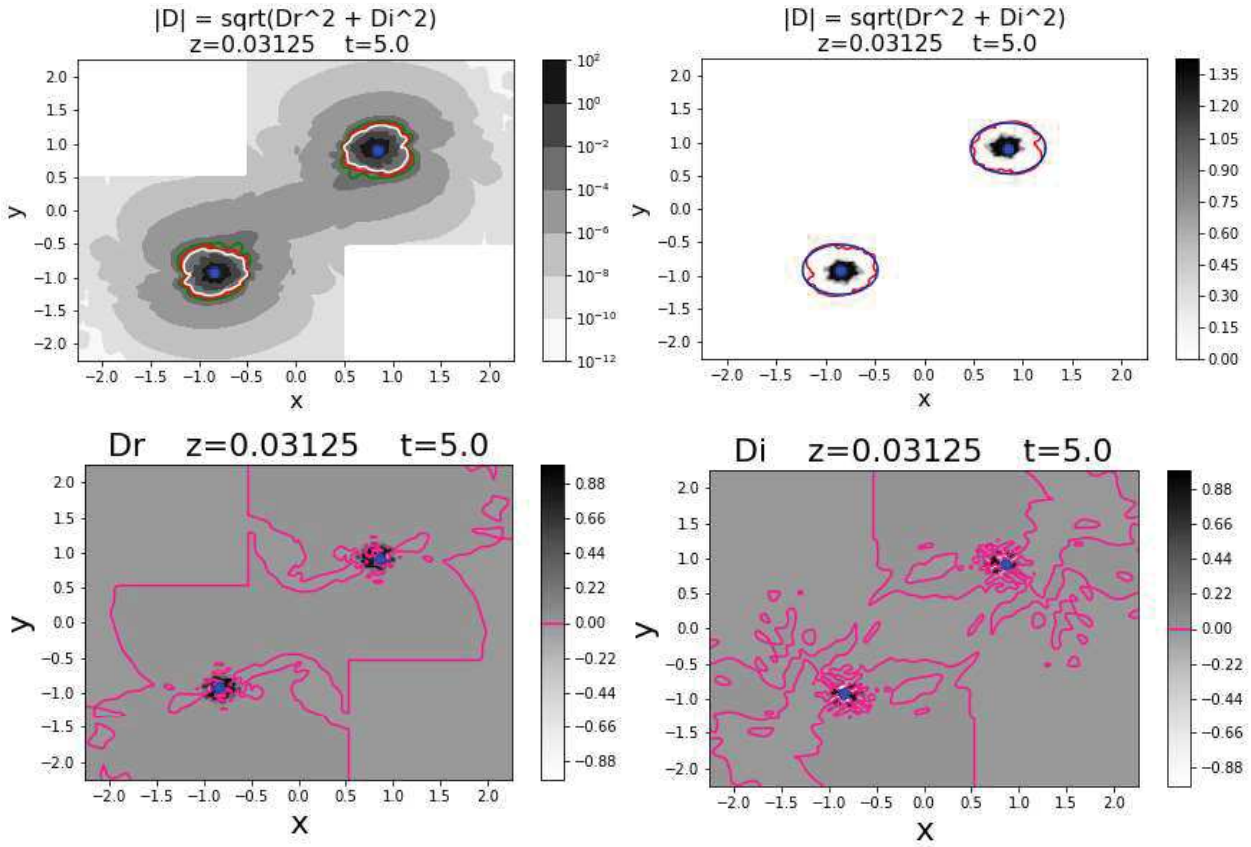
|D| = sqrt(Dr^2 + Di^2)
z=0.03125 t=5.0
|D| = sqrt(Dr^2 + Di^2)
z=0.03125 t=5.0
Dr z=0.03125 t=5.0
Di z=0.03125 t=5.0
x
y

Figure 7: T = 6

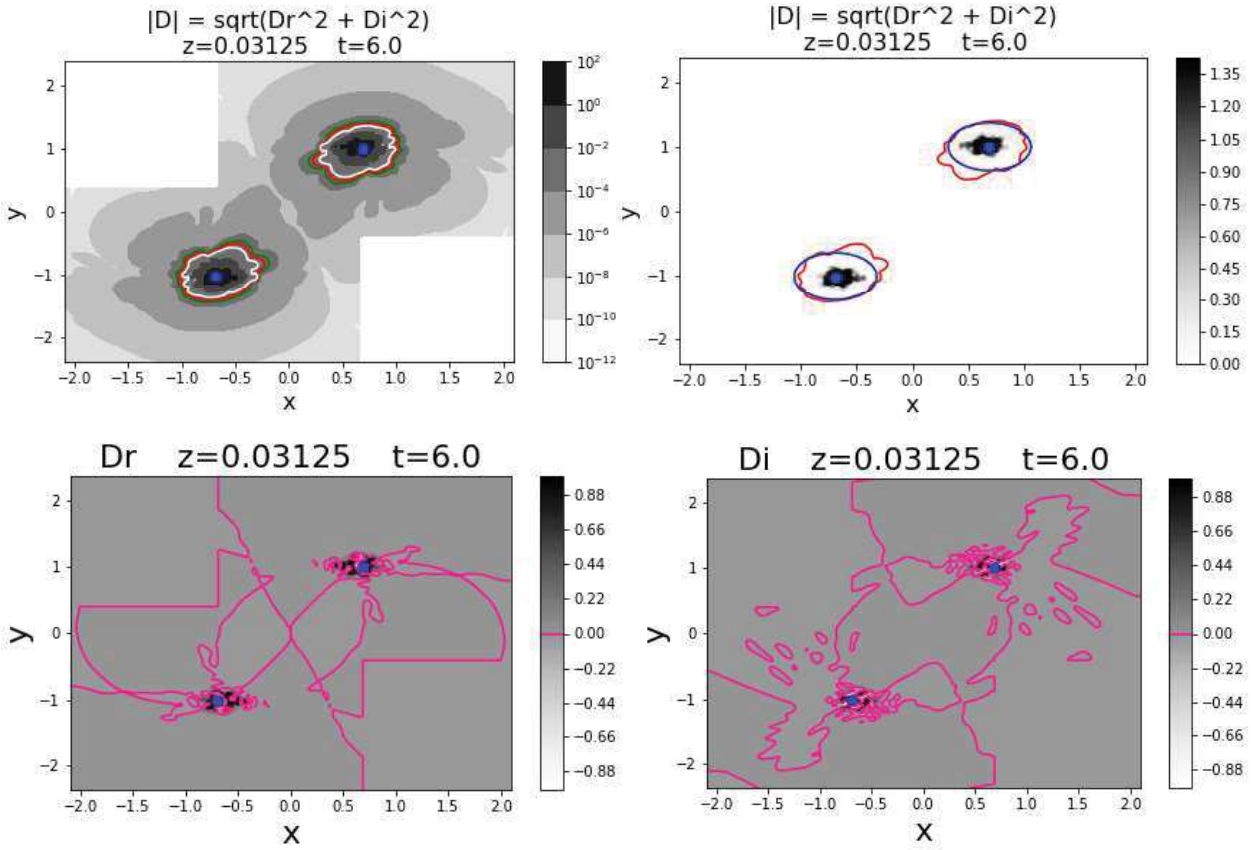
|D| = sqrt(Dr^2 + Di^2)
z=0.03125 t=6.0
|D| = sqrt(Dr^2 + Di^2)
z=0.03125 t=6.0
Dr z=0.03125 t=6.0
Di z=0.03125 t=6.0
x
y

Figure 8: T = 7

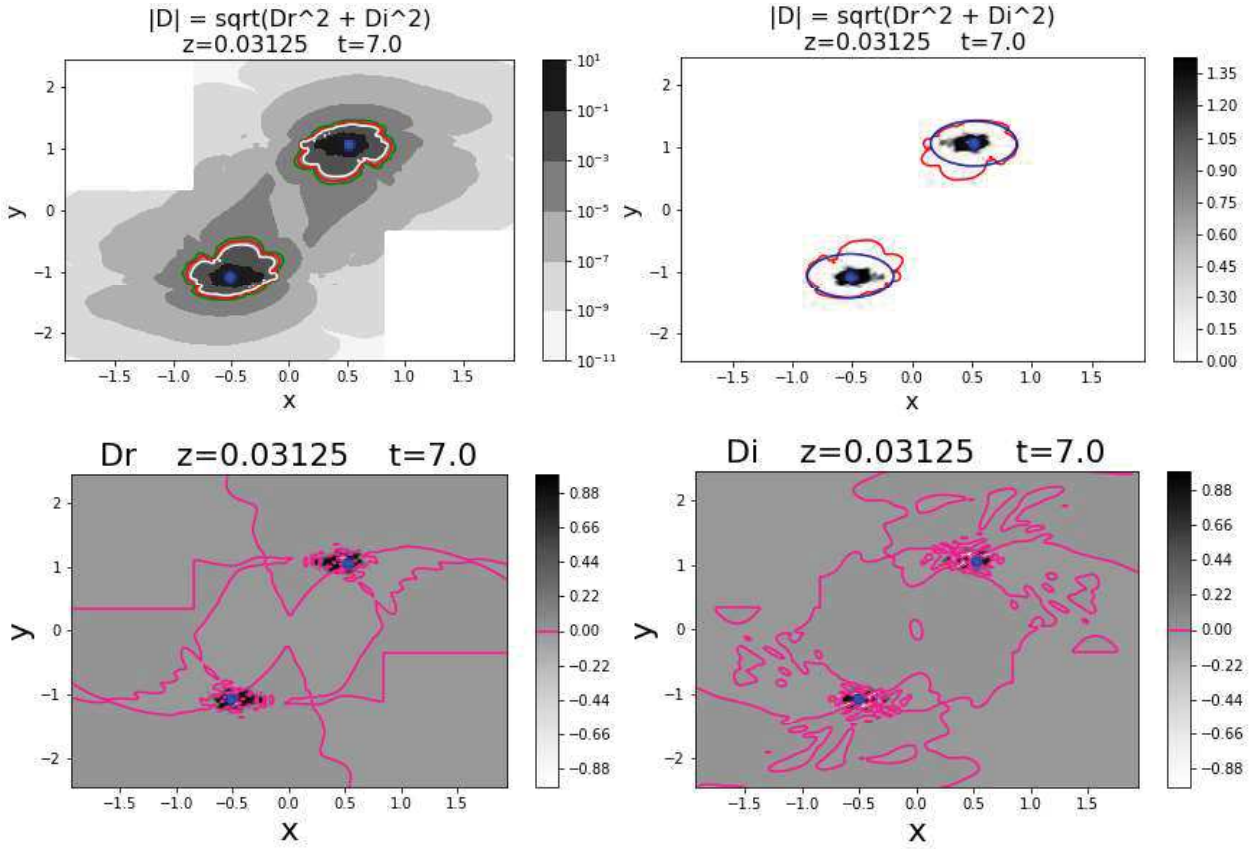
|D| = sqrt(Dr^2 + Di^2)
z=0.03125 t=7.0
|D| = sqrt(Dr^2 + Di^2)
z=0.03125 t=7.0
Dr z=0.03125 t=7.0
Di z=0.03125 t=7.0
x
y

Figure 9: T = 8

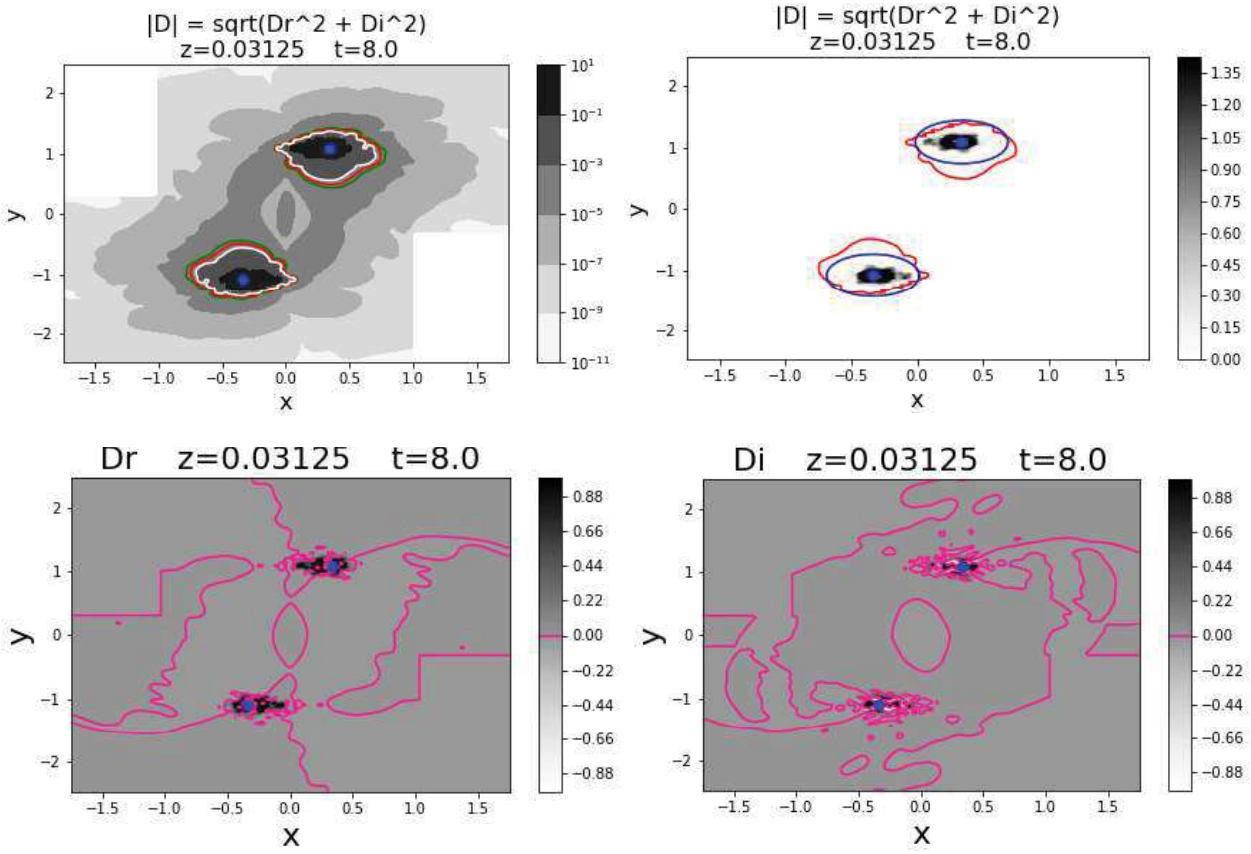
|D| = sqrt(Dr^2 + Di^2)
z=0.03125 t=8.0
|D| = sqrt(Dr^2 + Di^2)
z=0.03125 t=8.0
Dr z=0.03125 t=8.0
Di z=0.03125 t=8.0
x
y

Figure 10: T = 9

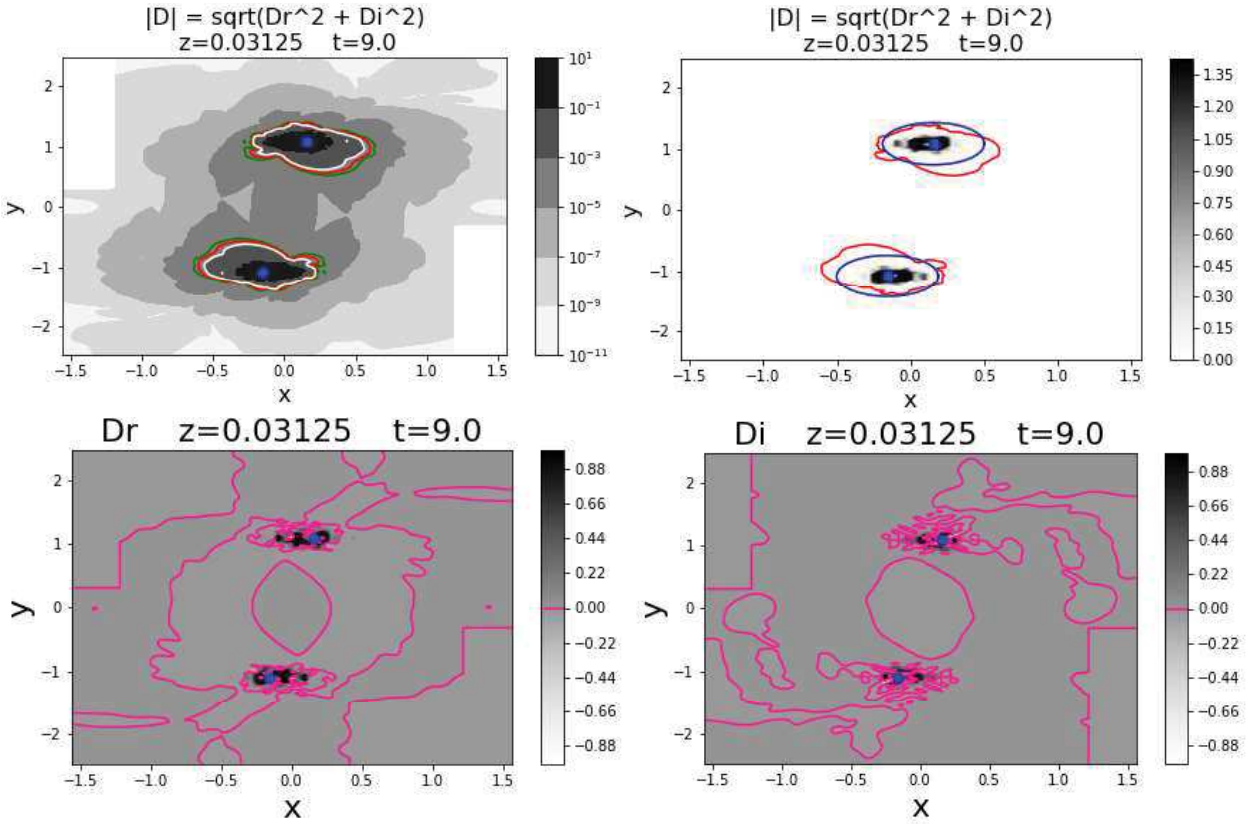
|D| = sqrt(Dr^2 + Di^2)
z=0.03125 t=9.0
|D| = sqrt(Dr^2 + Di^2)
z=0.03125 t=9.0
Dr z=0.03125 t=9.0
Di z=0.03125 t=9.0
x
y

Figure 11: T = 10

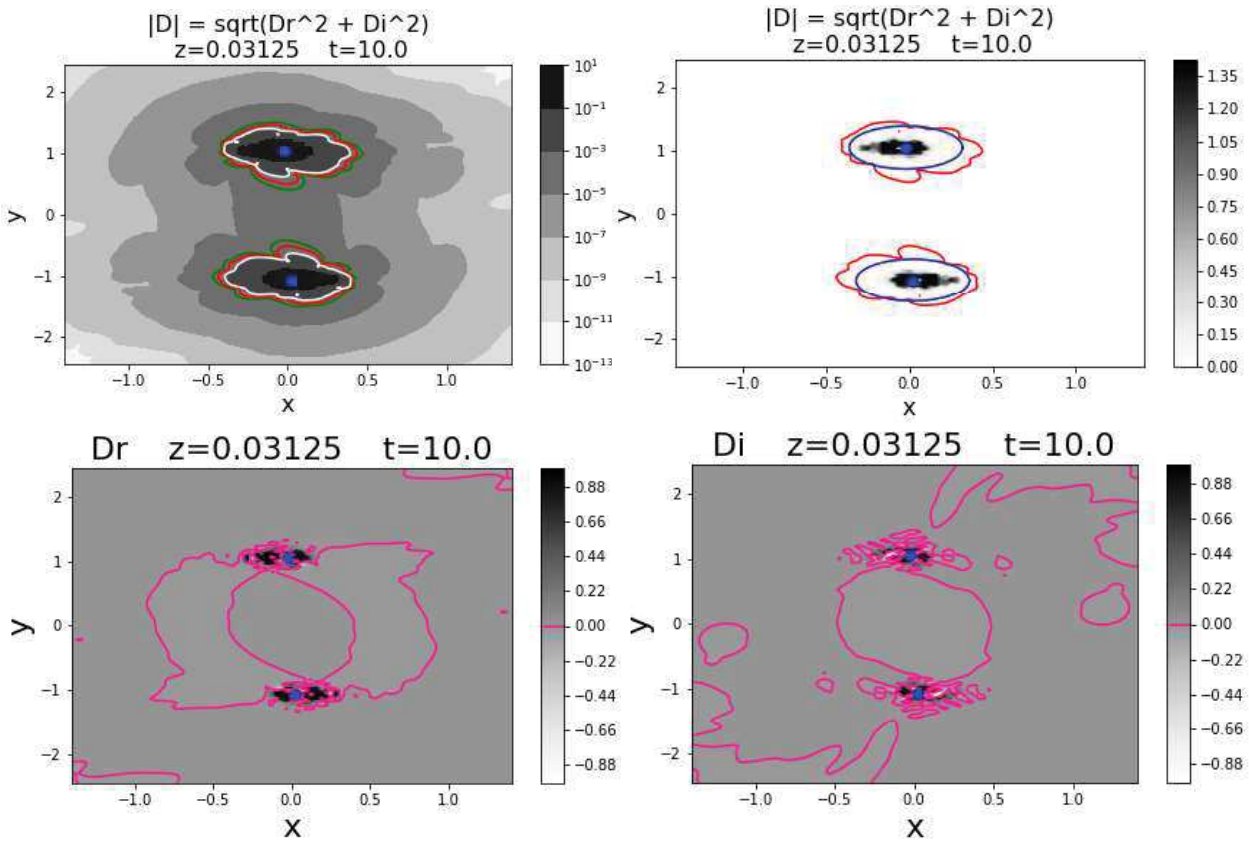

Figure 12: T = 11

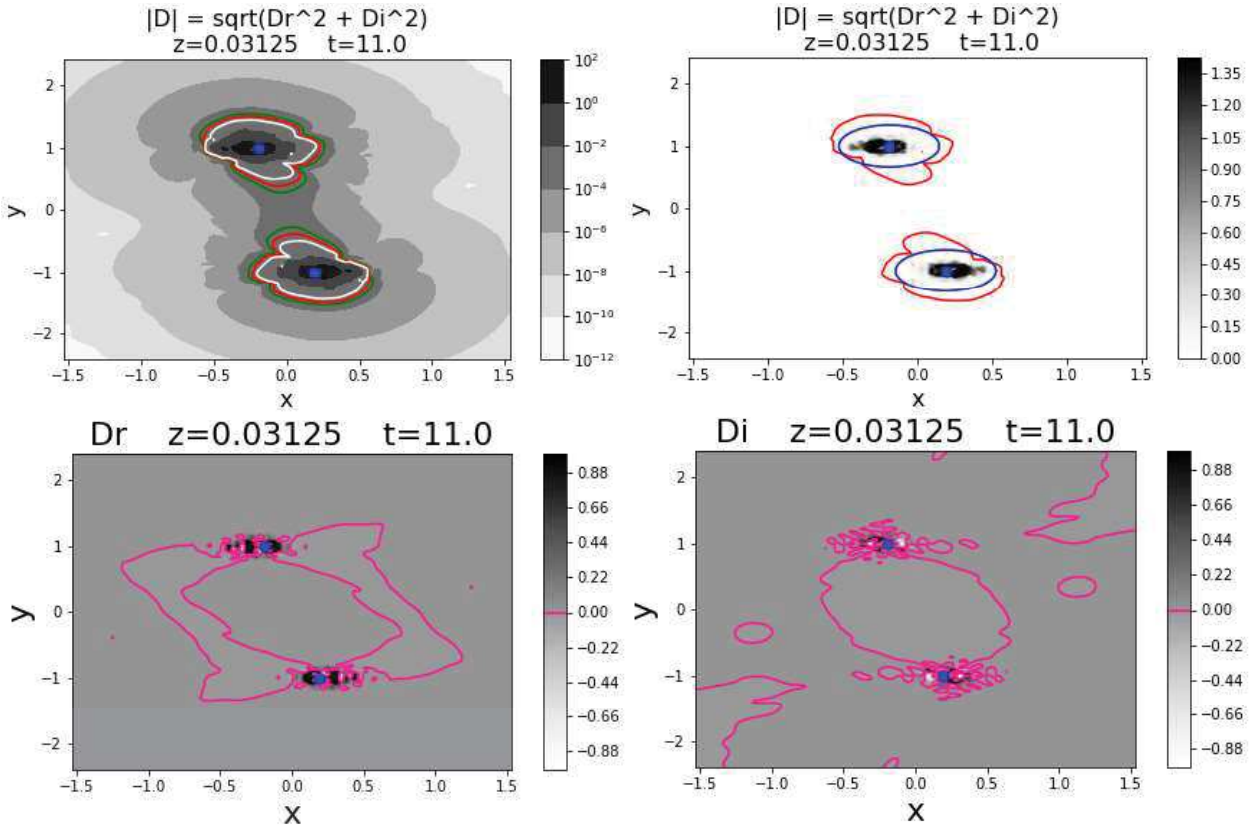

Figure 13: T = 12

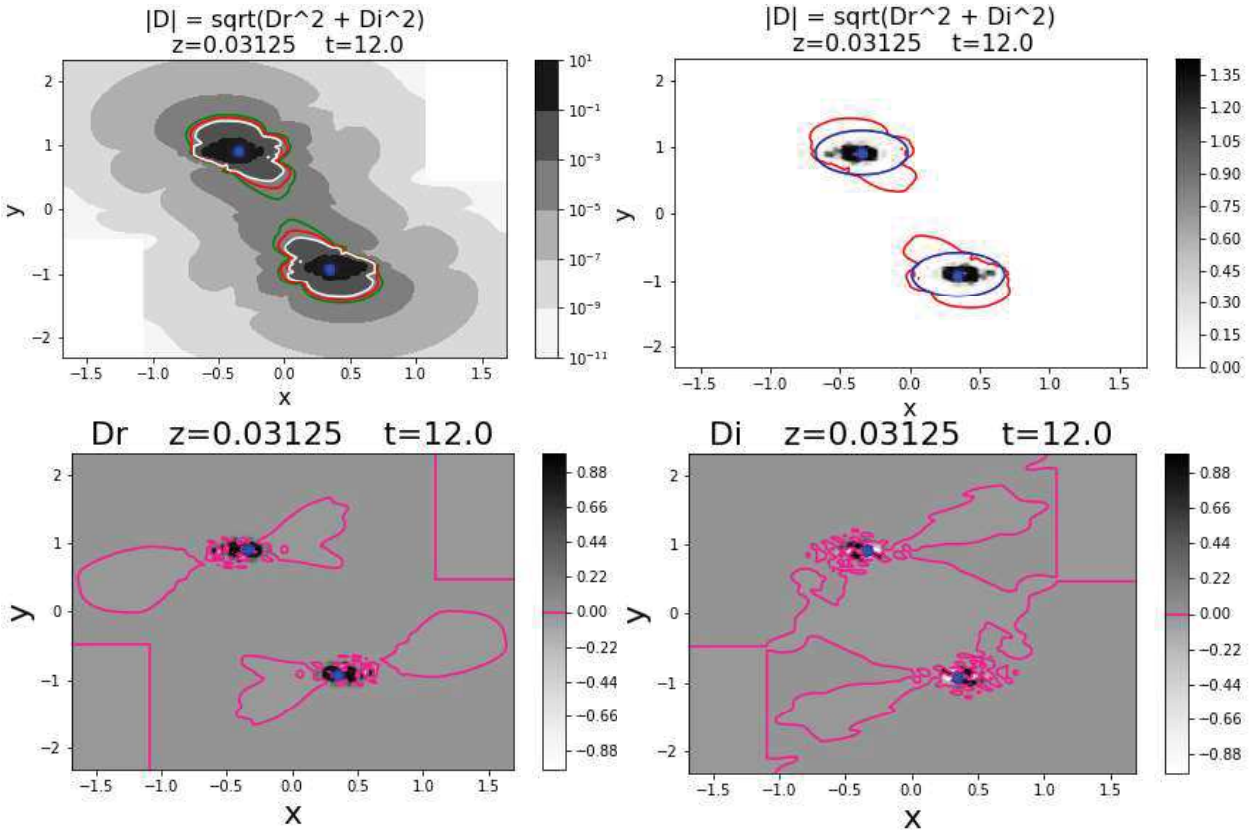

Figure 14: T = 13

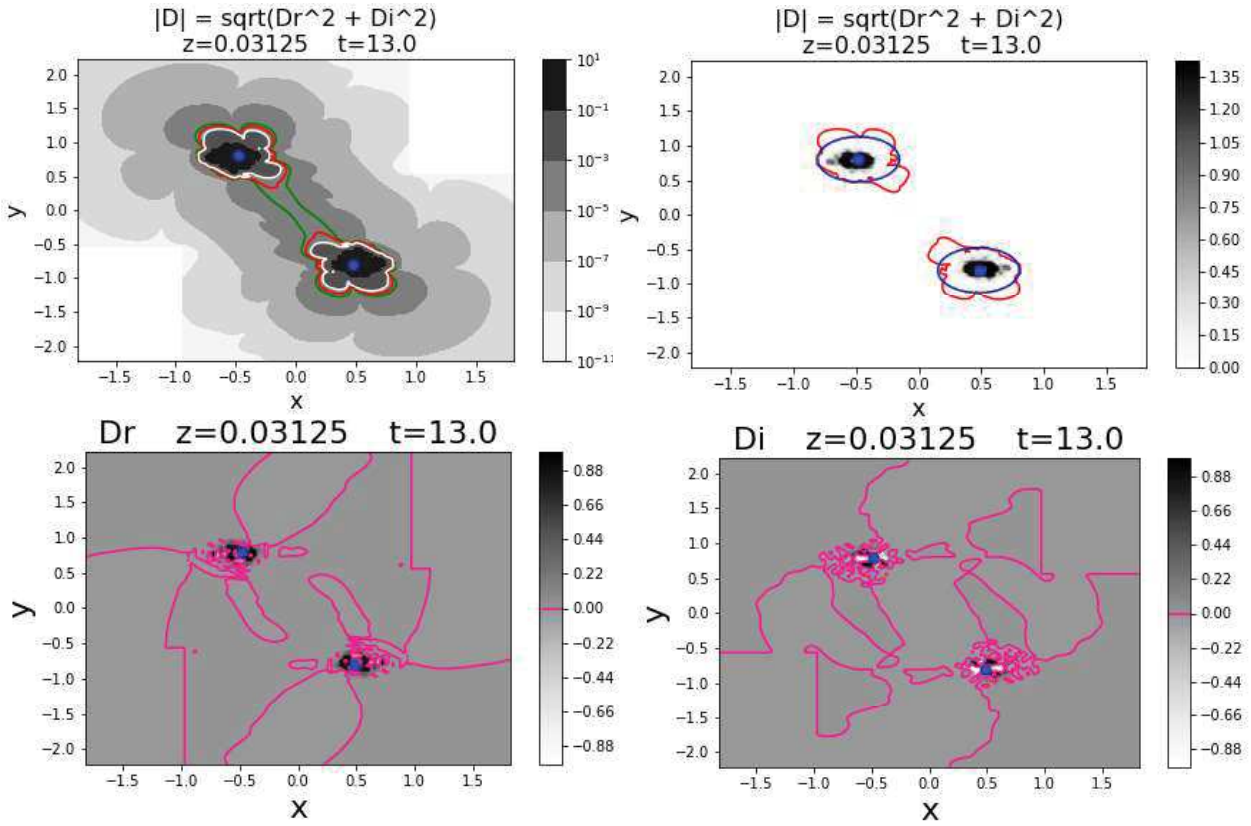

Figure 15: T = 14

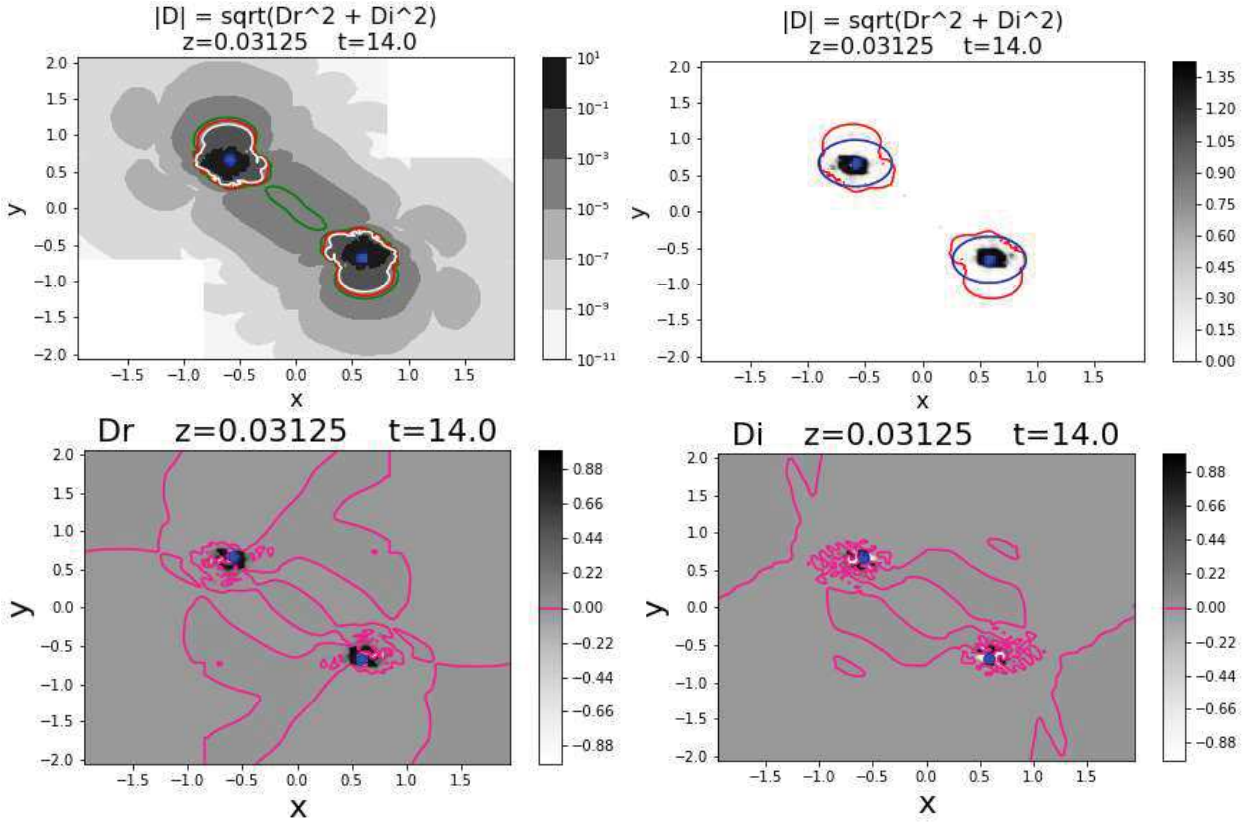

Figure 16: T = 15

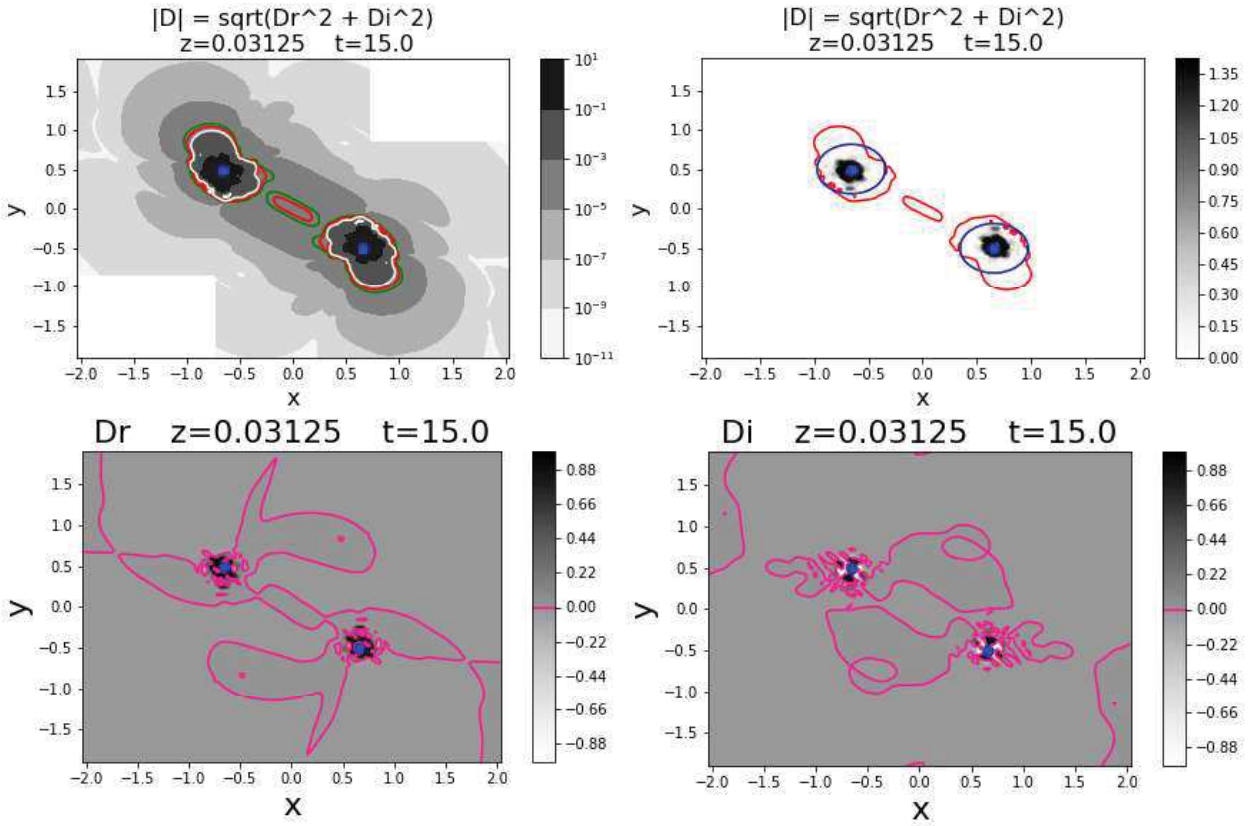

Figure 17: T = 16

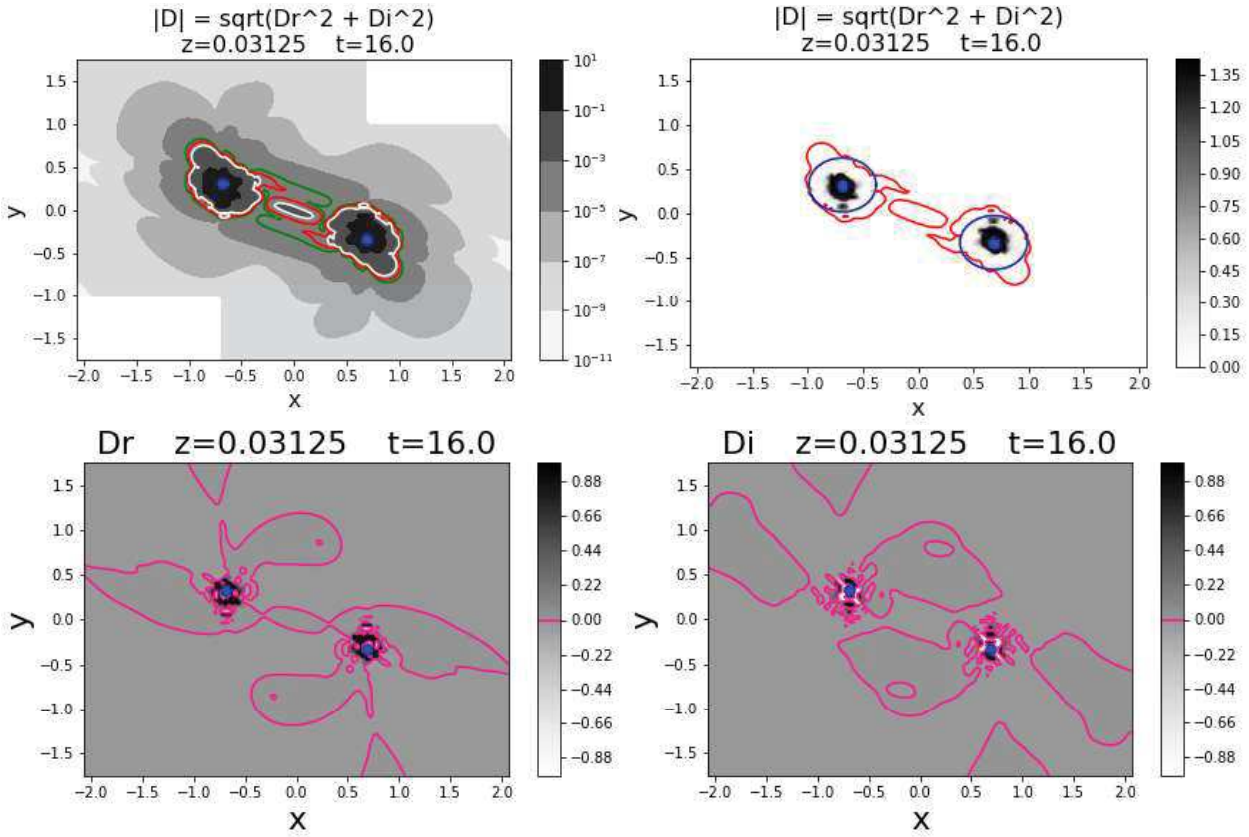

Figure 18: T = 17

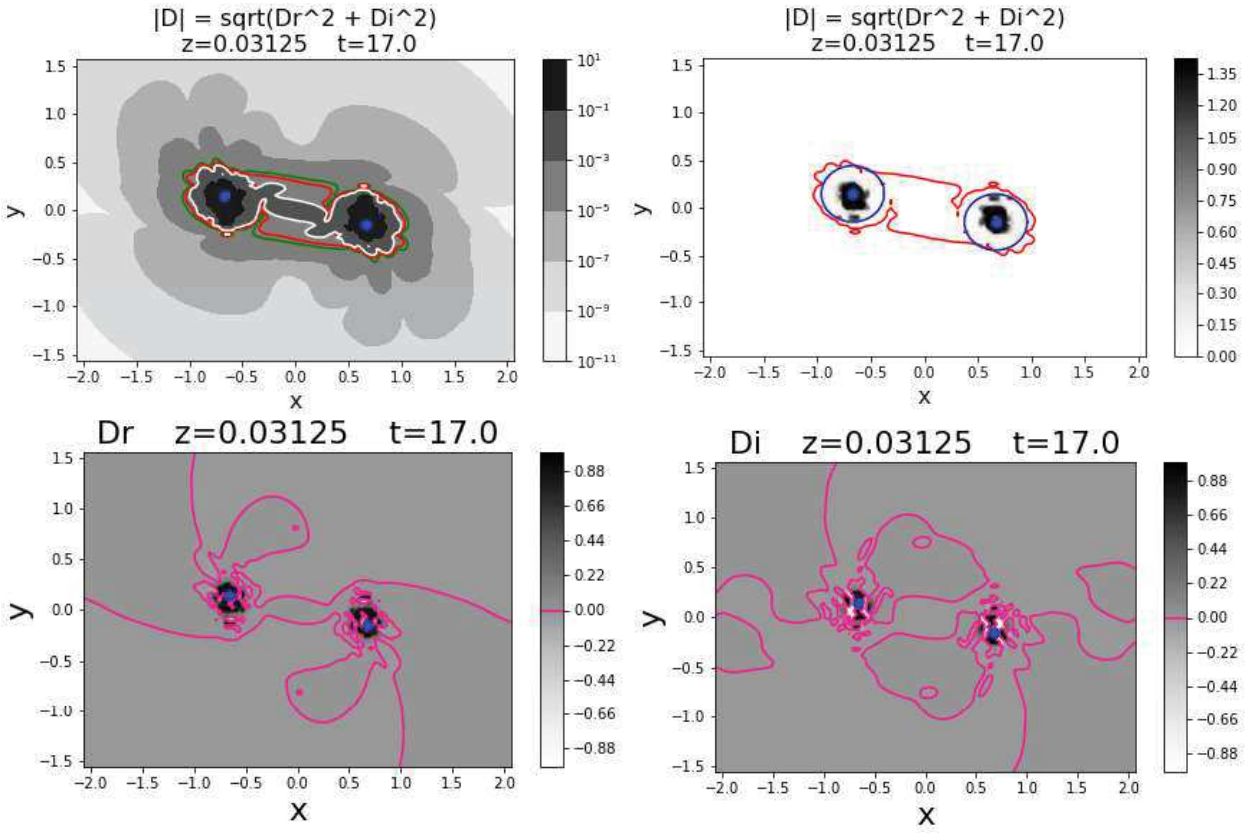

Figure 19: T = 18

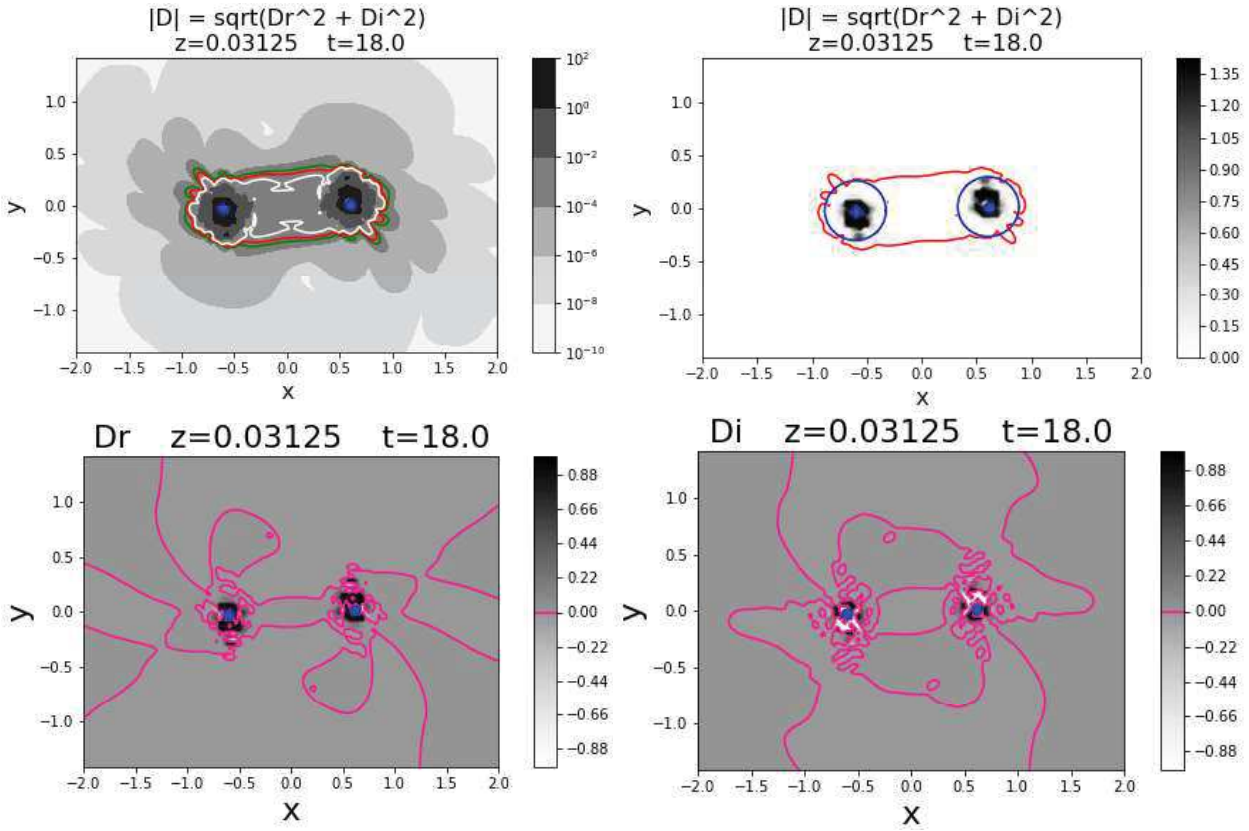

Figure 20: T = 19

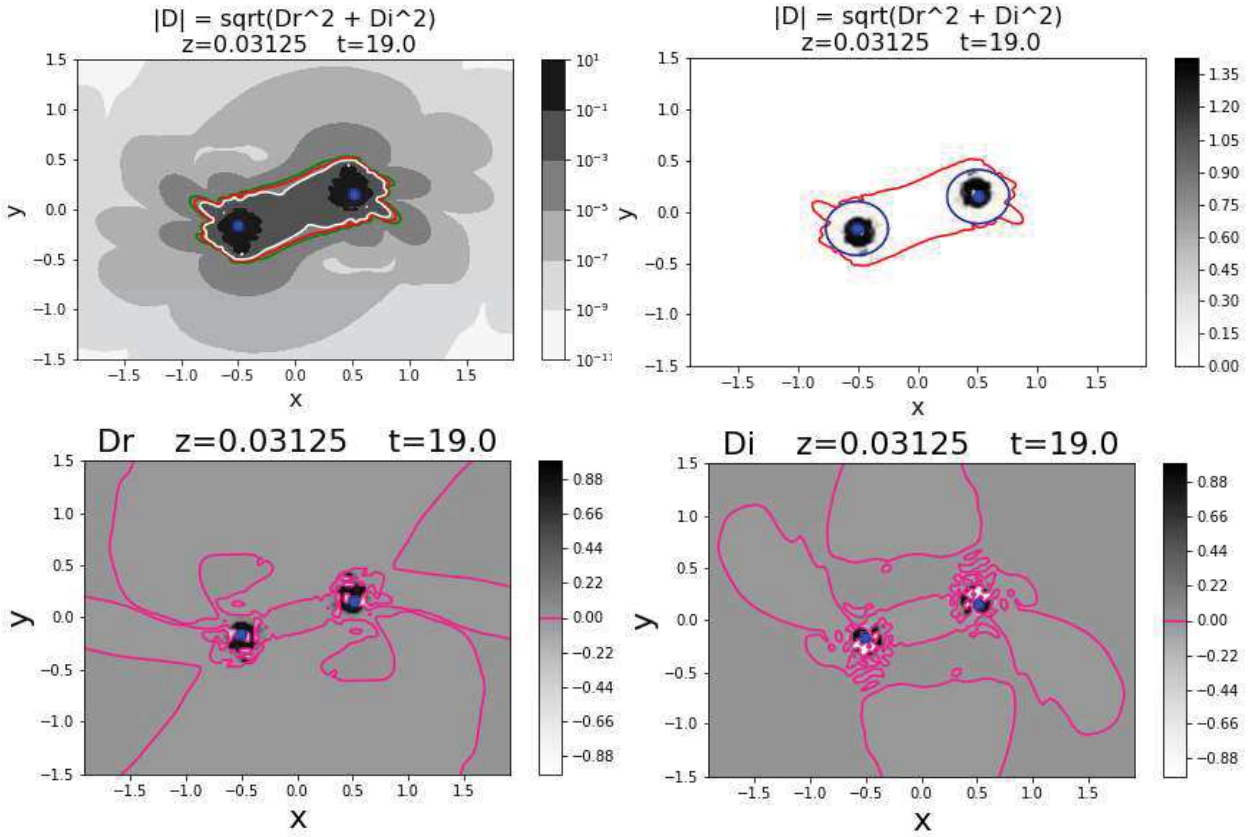

Figure 21: T = 20

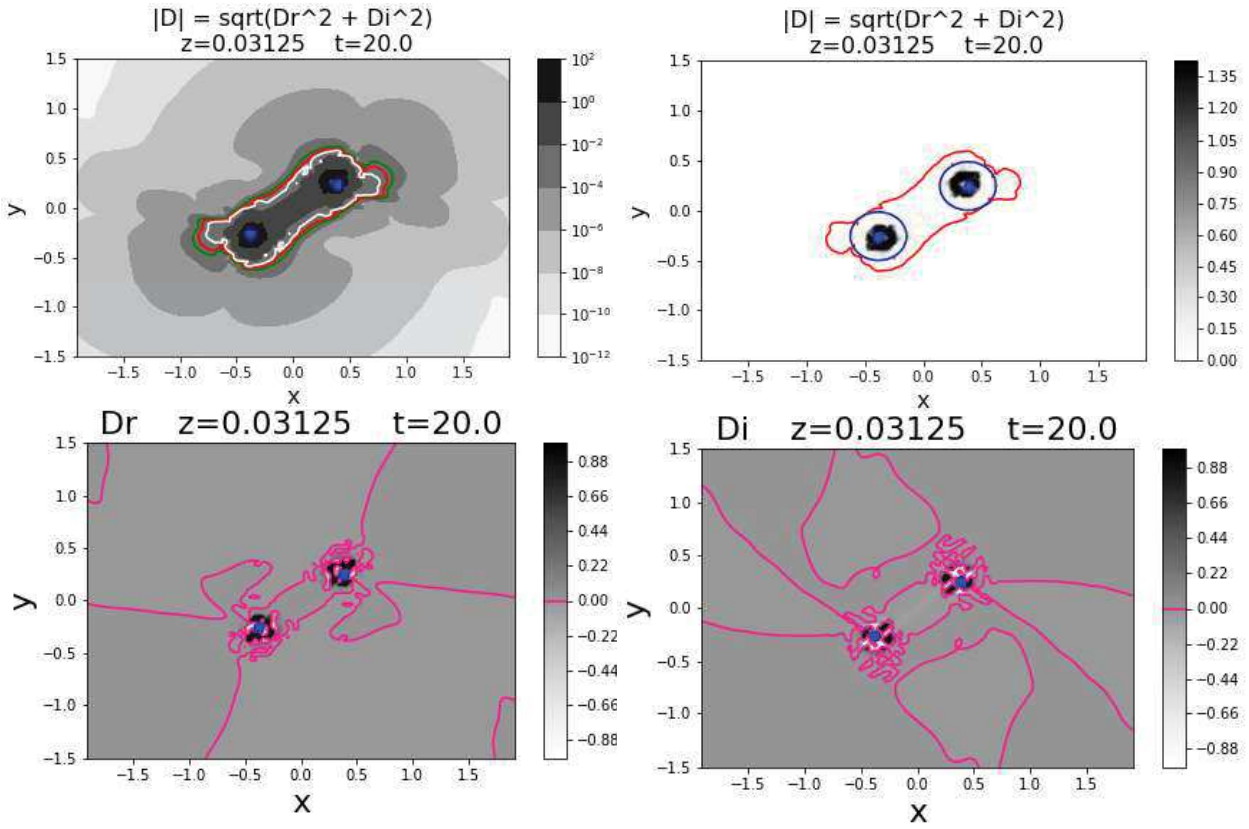

Figure 22: T = 21

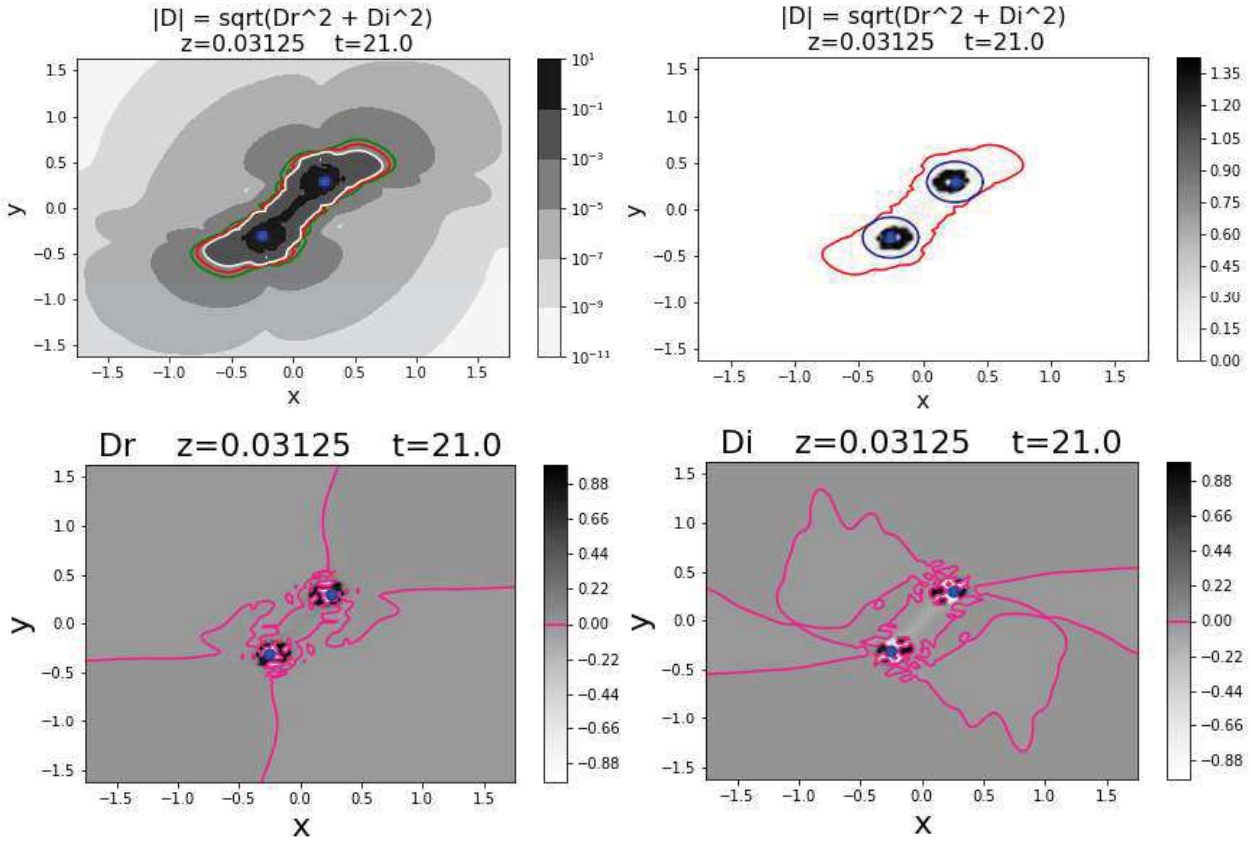

Figure 23: T = 22

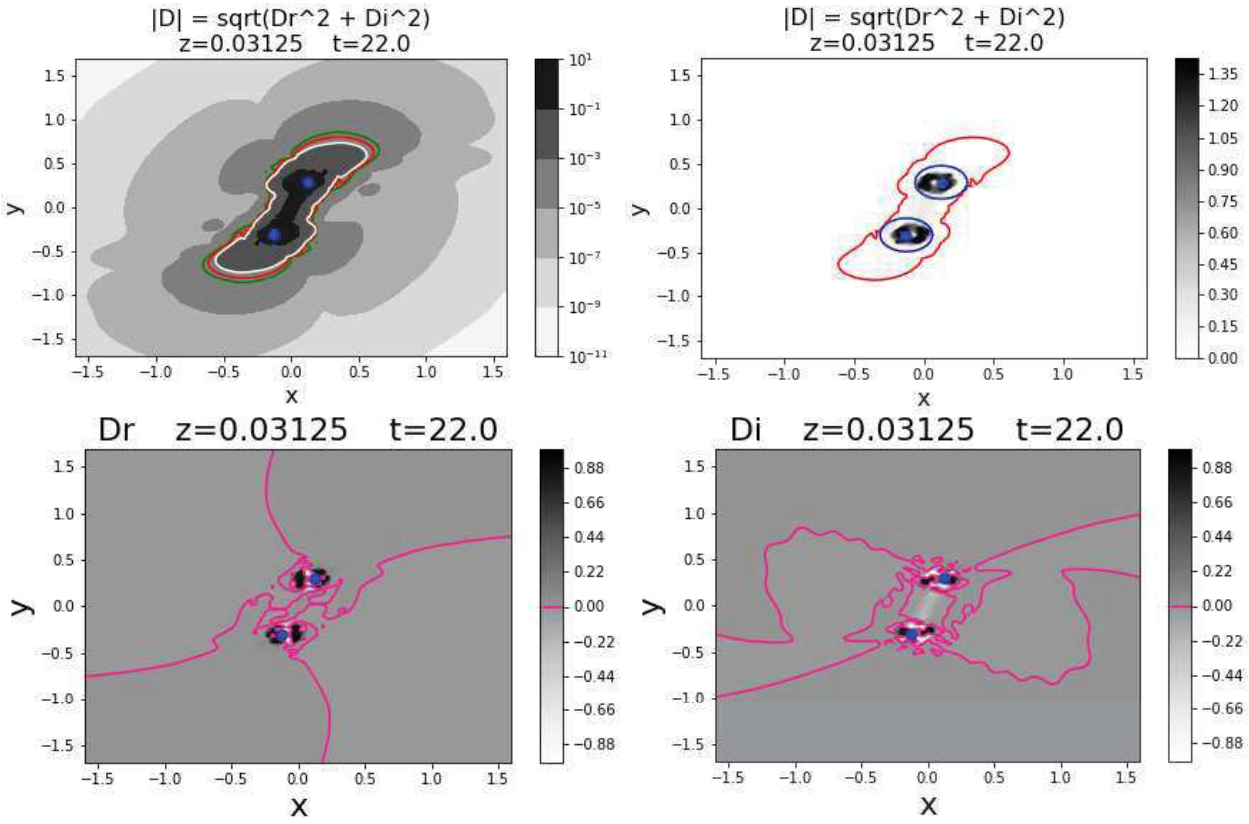

Figure 24: T = 23

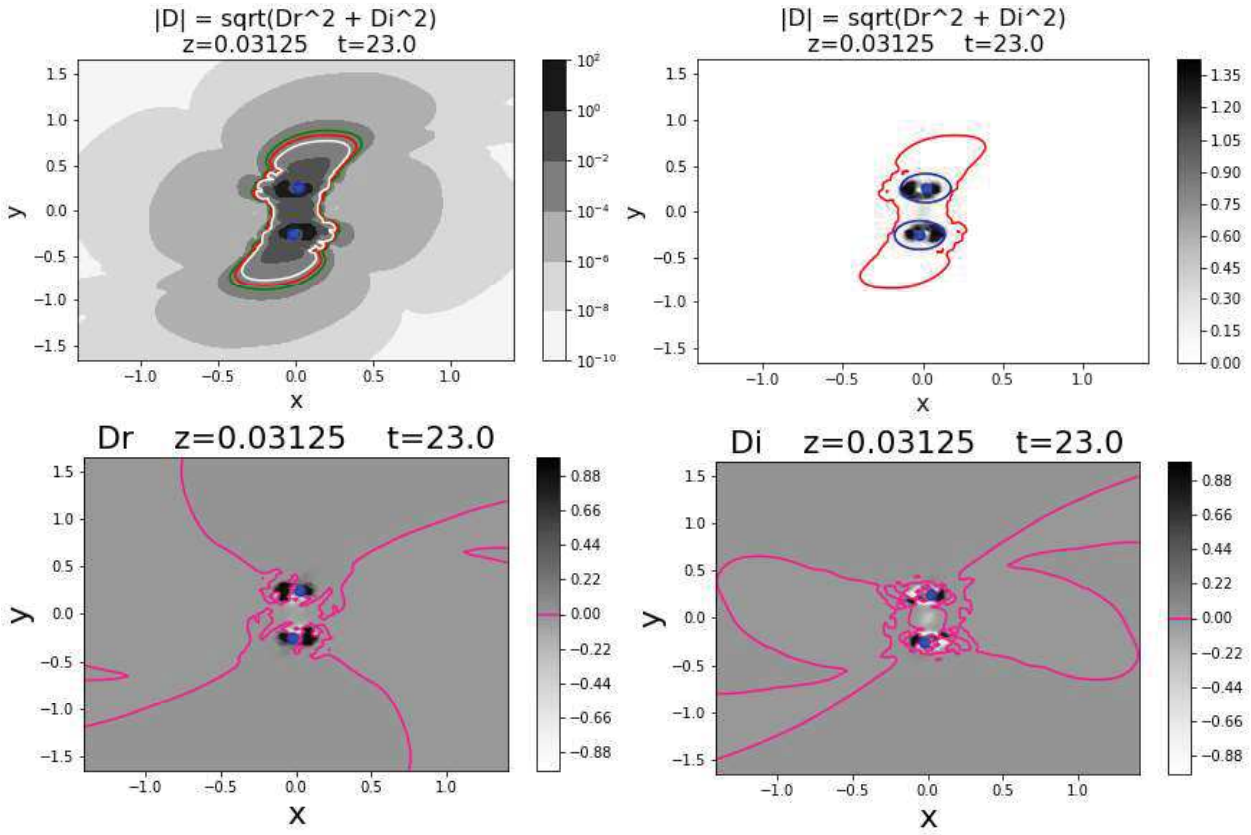

Figure 25: T = 24

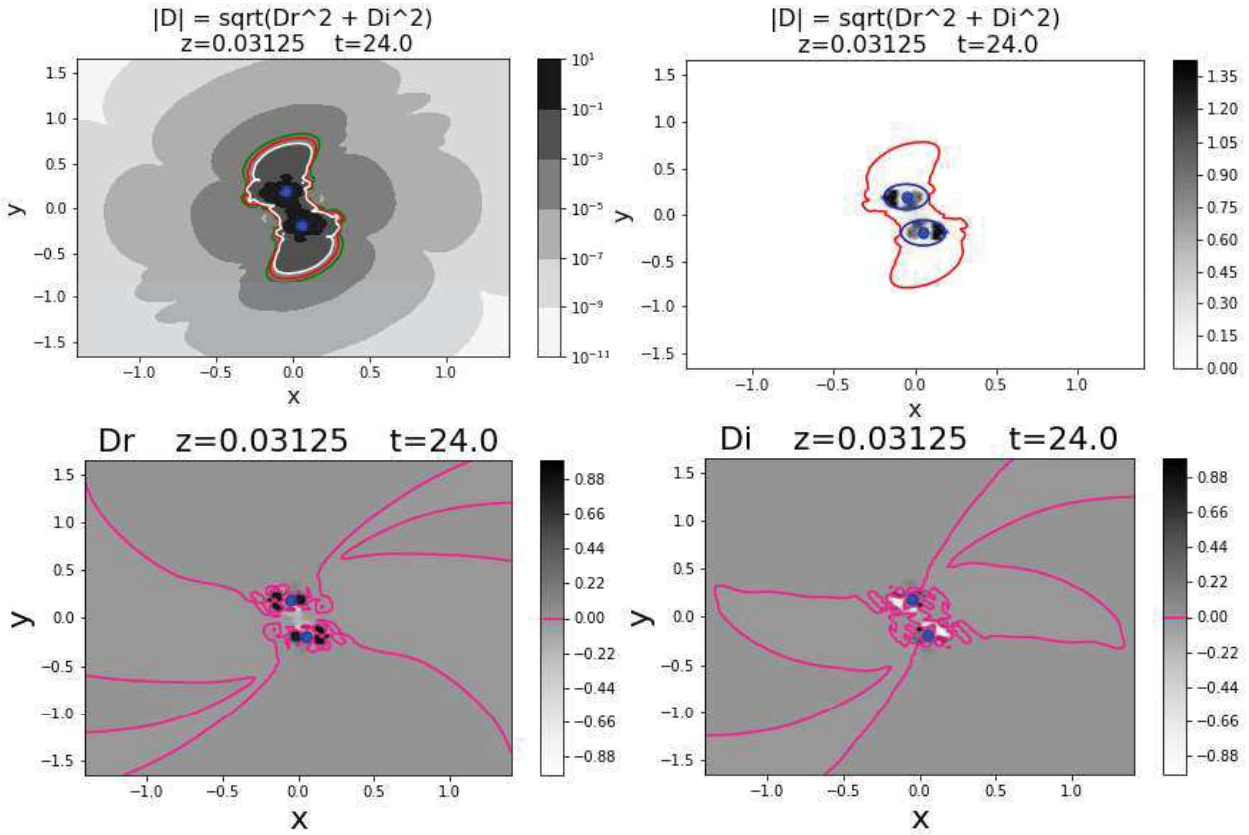

Figure 26: T = 25

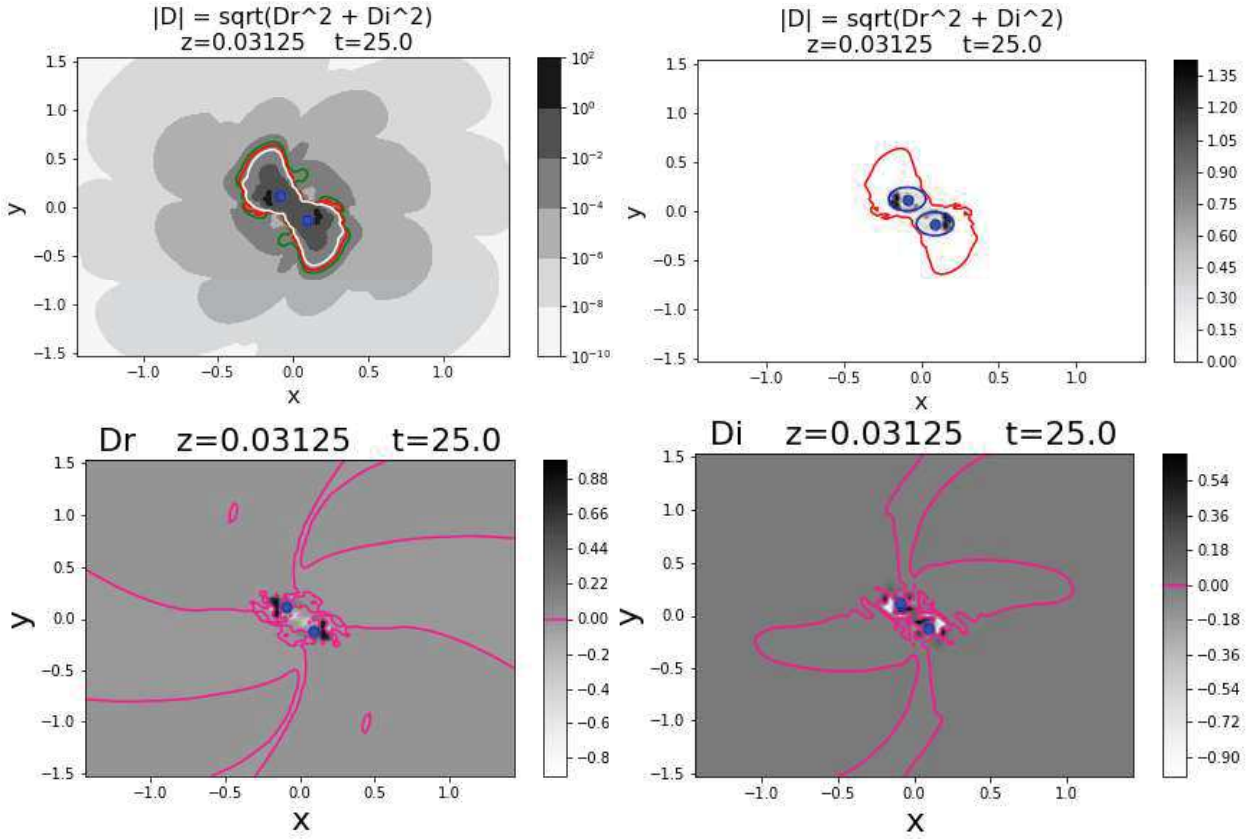

Figure 27: T = 26

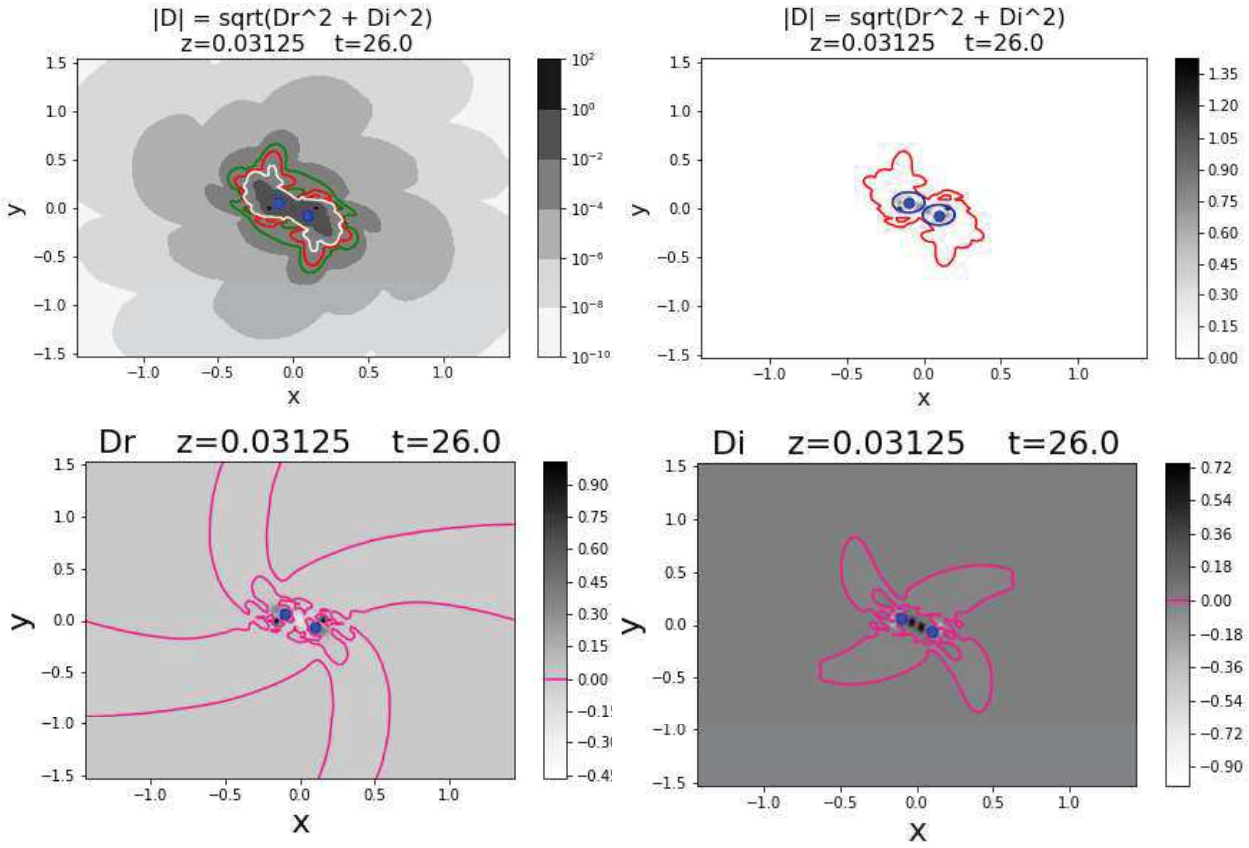

Figure 28: T = 27

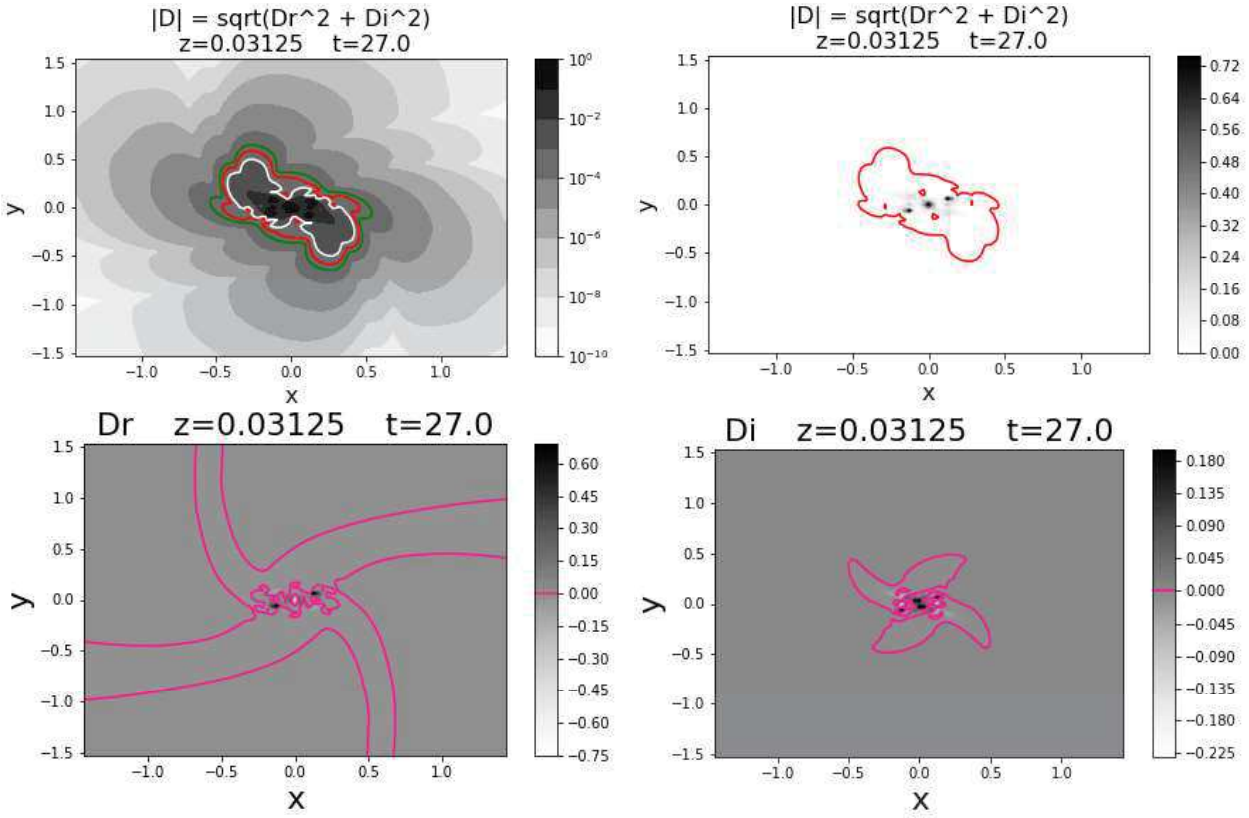

Figure 29: T = 28

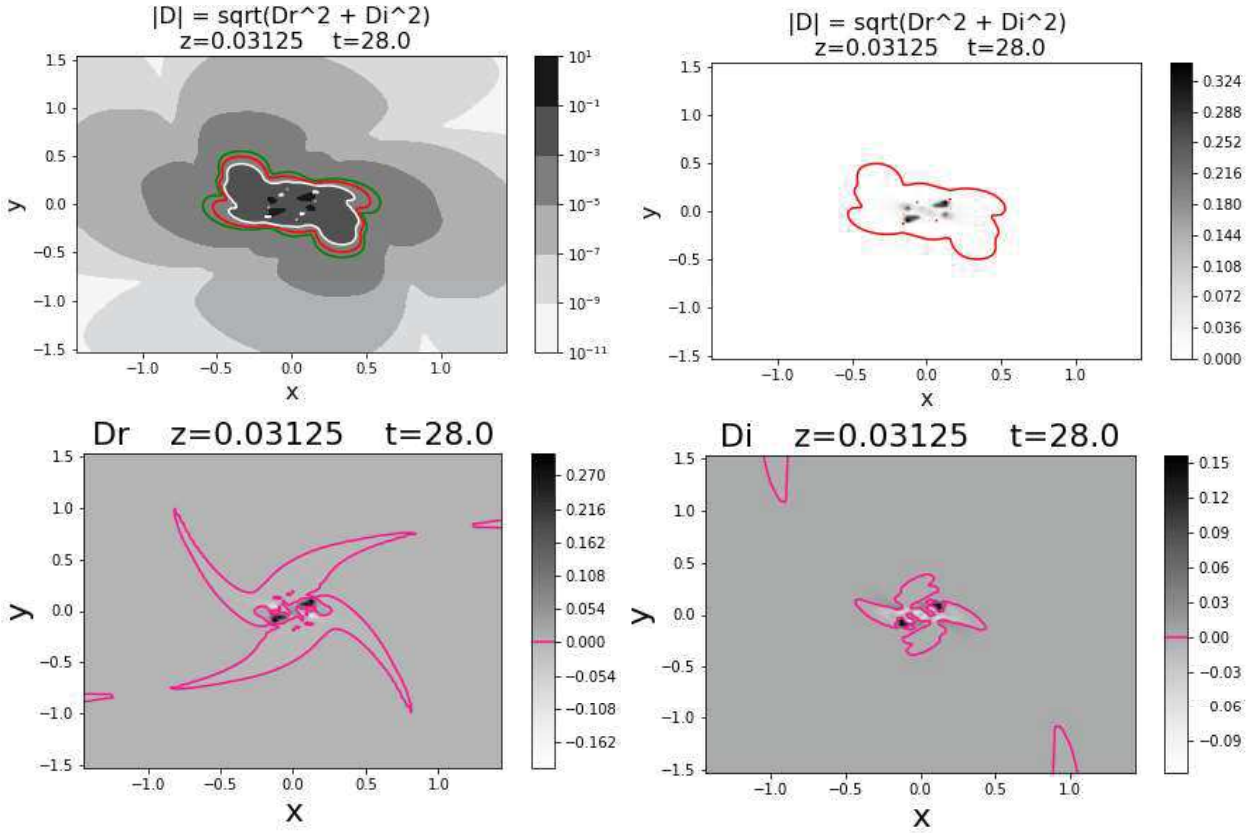

Figure 30: T = 29

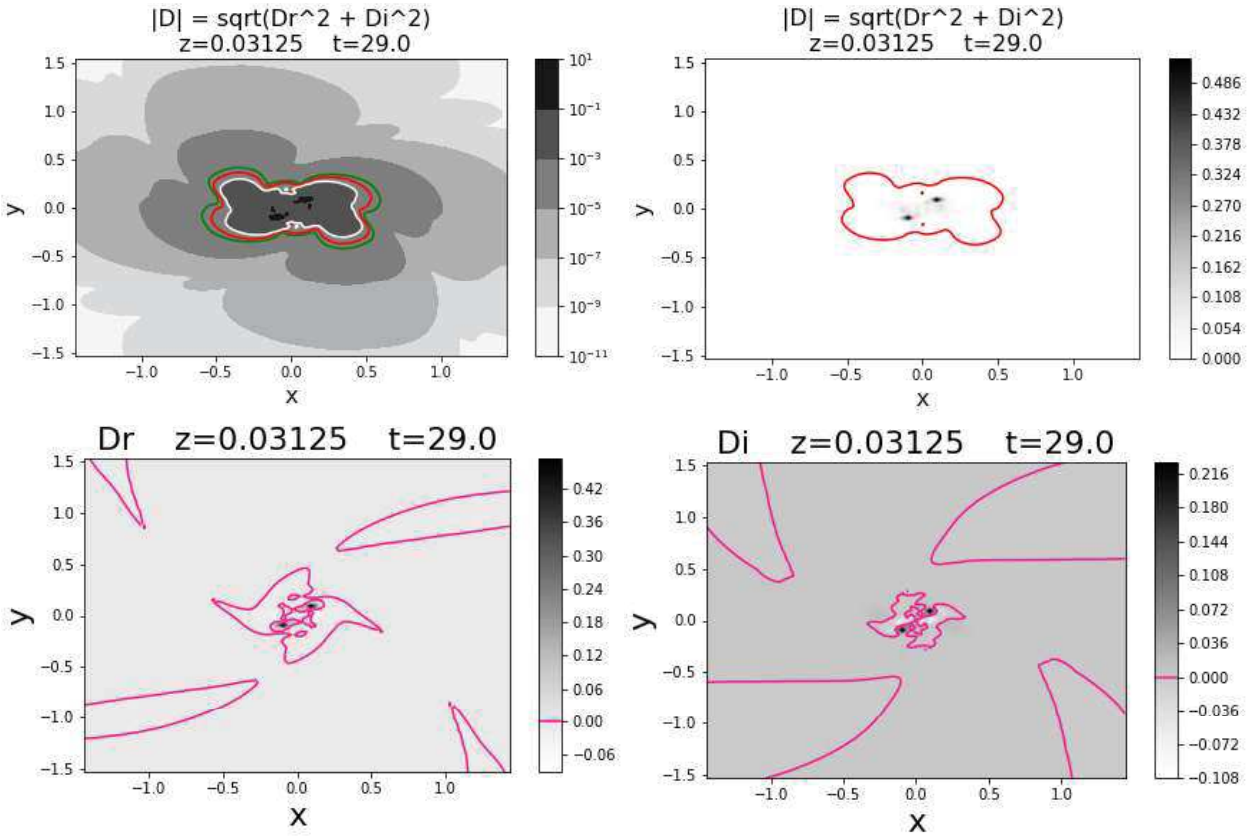

Figure 31: T = 30

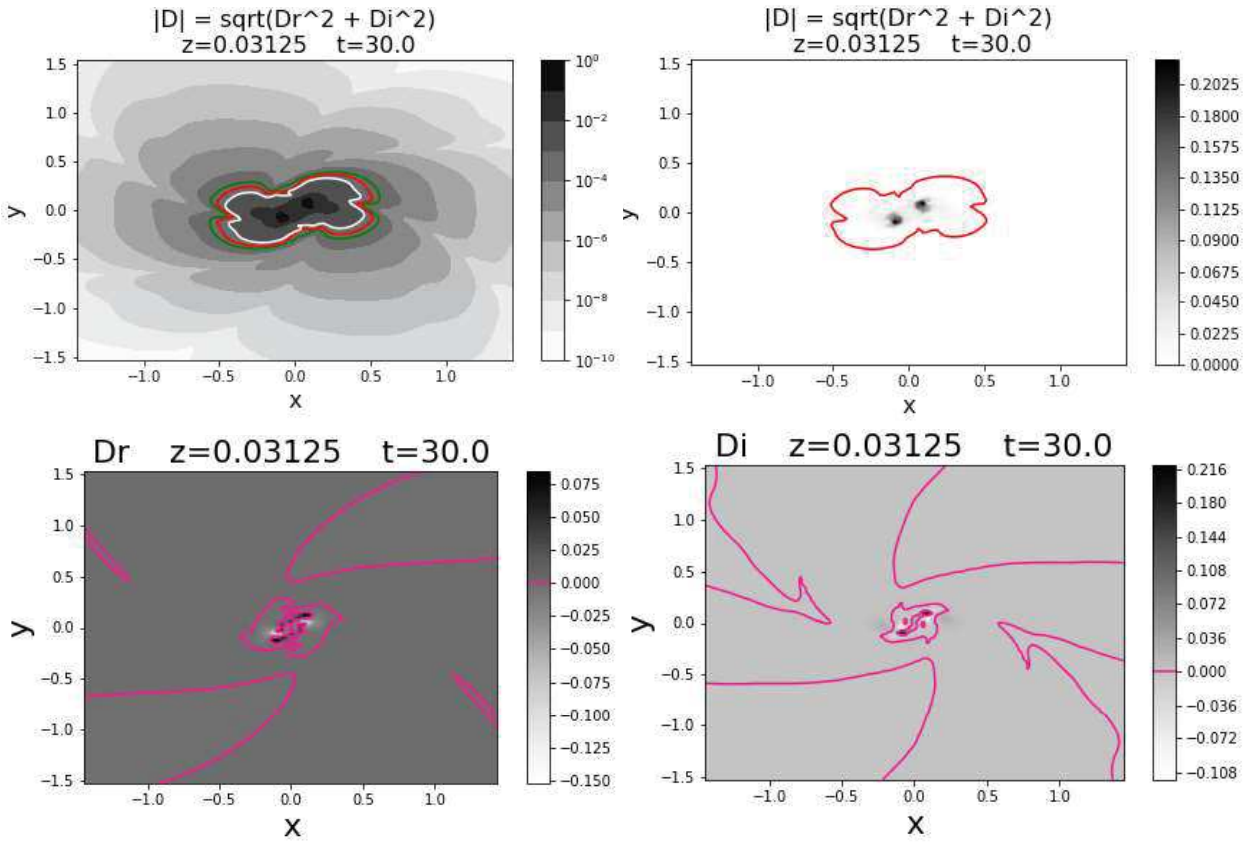

Figure 32: T = 34

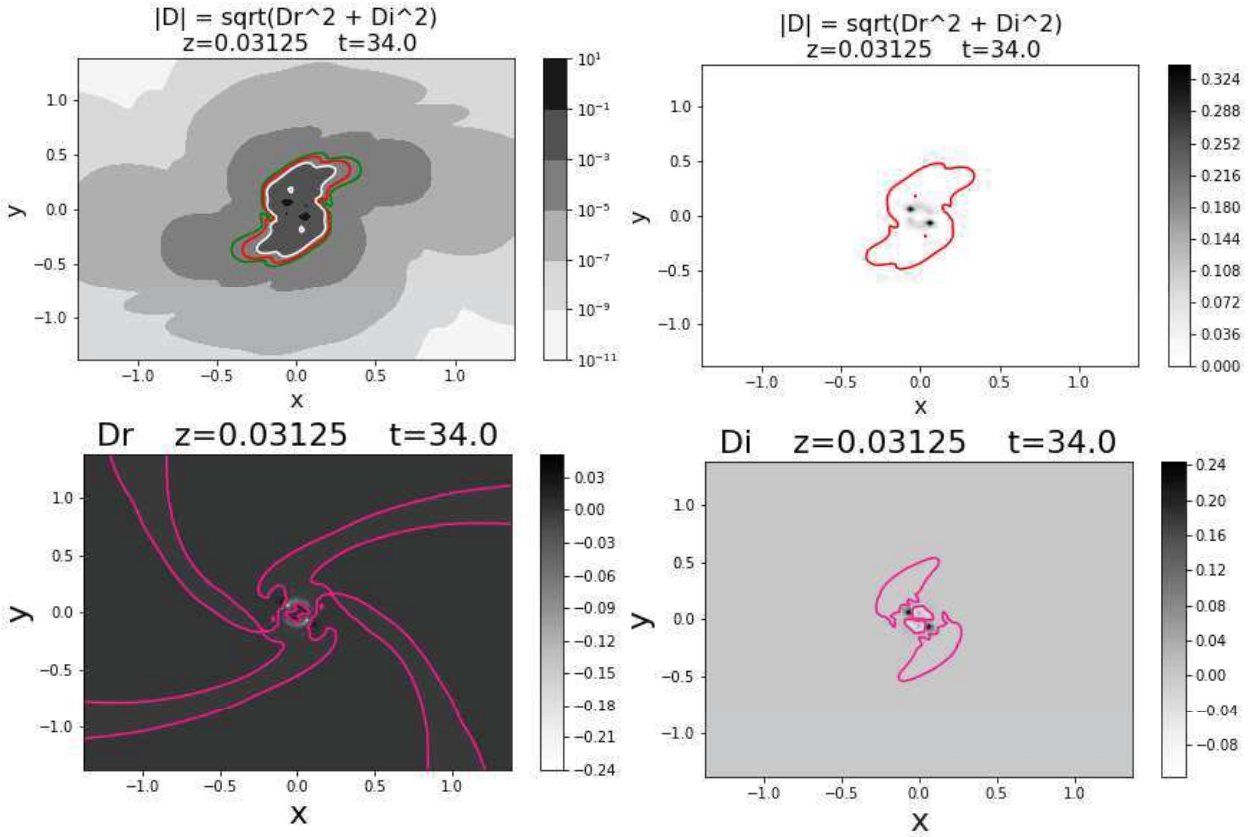

Figure 33: T = 38

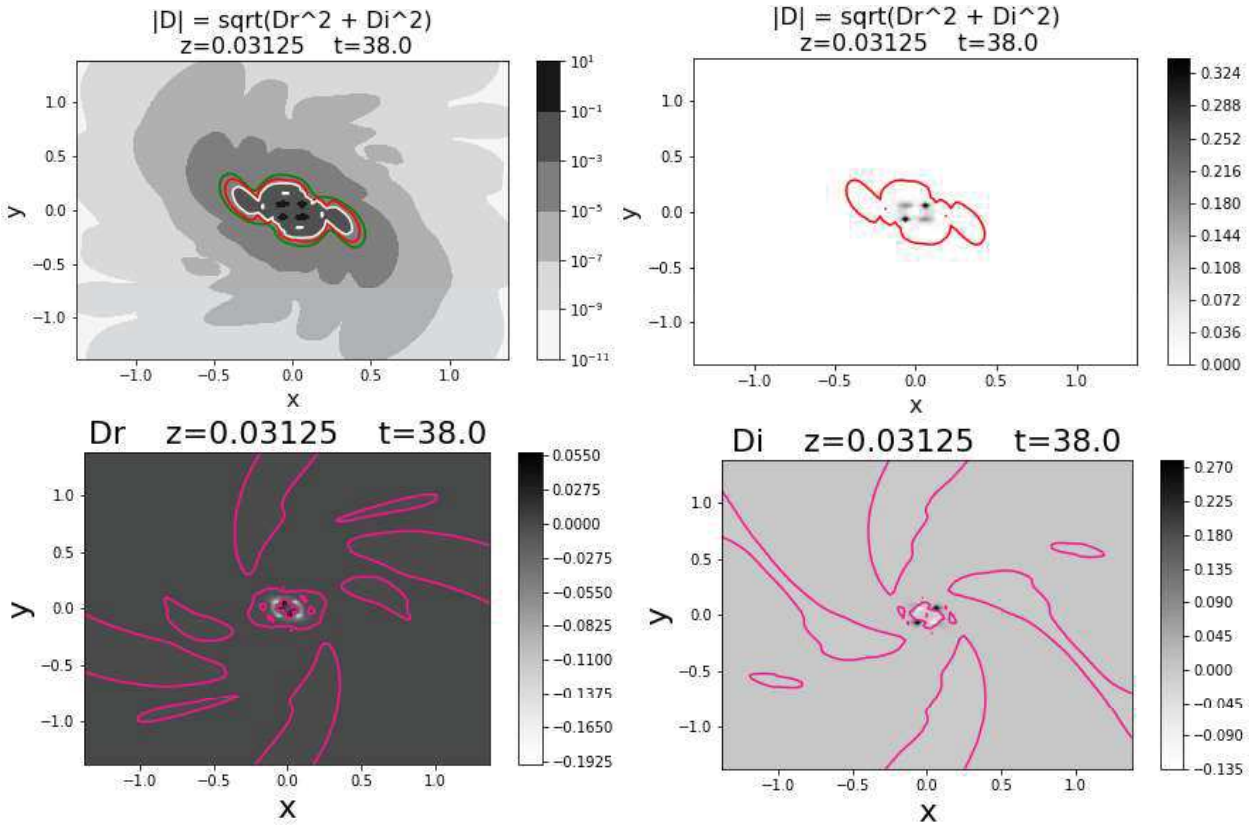

Figure 34: T = 42

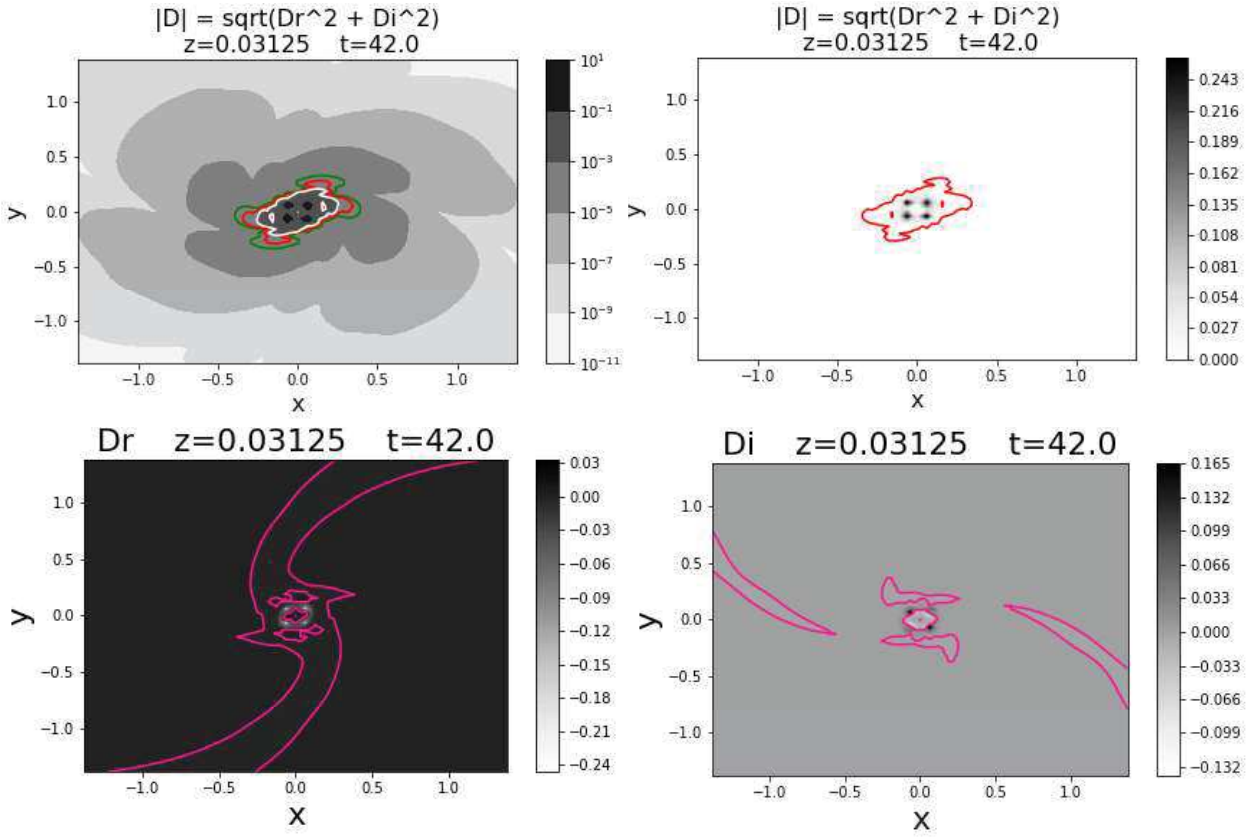

Figures 35-51: Plots of |D| vs y for fixed x ("slice plots") at times T = 12, 16, 20, 24, and plots of locations of local minima of |D| along these selected constant x slice plots.

Legend for Figures 35-51:

- "Slice plots" = plots of |D| vs y for fixed x (at a fixed time).
- Upper left plot: Plot of |D| vs y and x with points of local minima along slice plots indicated
- Remaining plots (not upper left): Slice plots of |D| at various resolutions indicating local minima.
- Green points (Upper left): Plots of local minima of |D| along slice plots.
- Green points (remaining plots): Points of |D| measured from numerical simulation [E. Schnetter, 2020]
- Blue dots: Centroids of MOTSs of initial BHs.
- Blue ellipses: "Radius-Averaged" MOTSs of initial BHs.
- Green contours (Upper left): level 0.0003 sets of |D|.
- Red contours (Upper left): level 0.0005 sets of |D|.
- White contours (Upper left): level 0.001 sets of |D|.

Figure 35: T = 12, x = 0

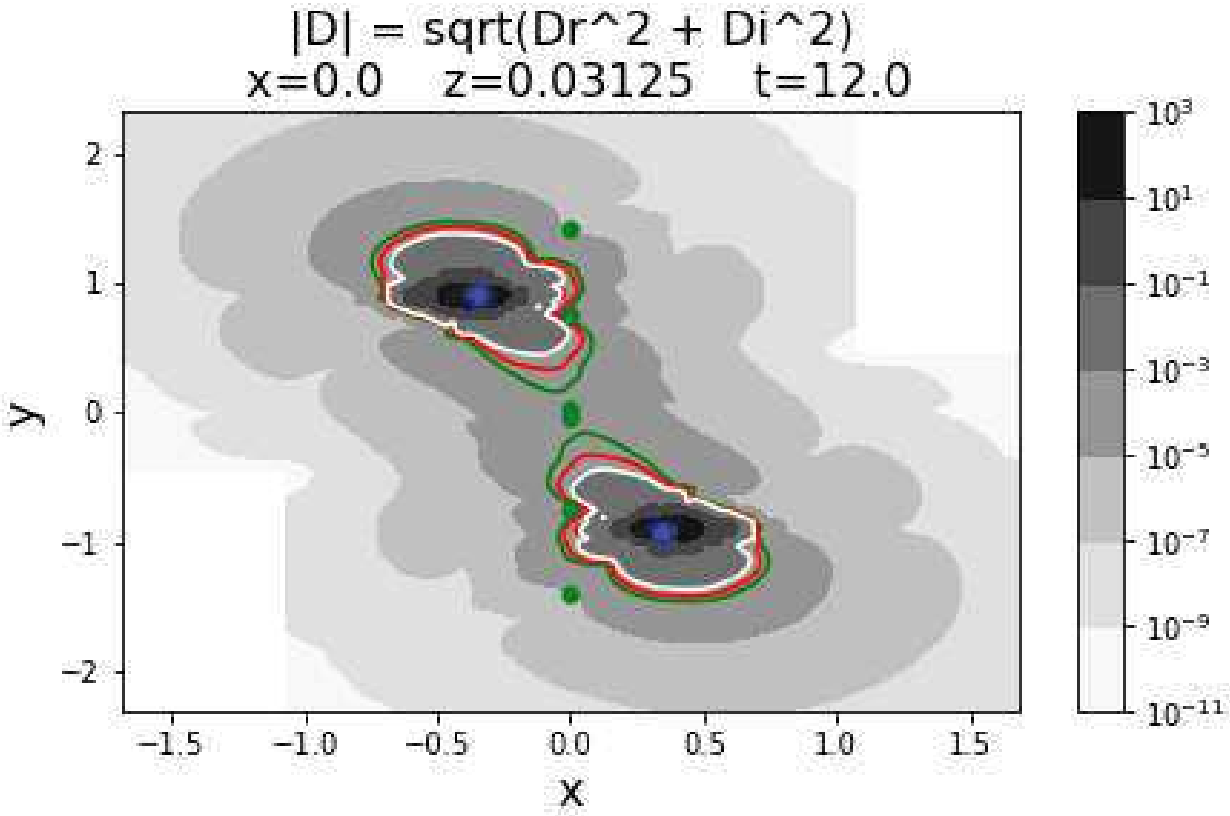

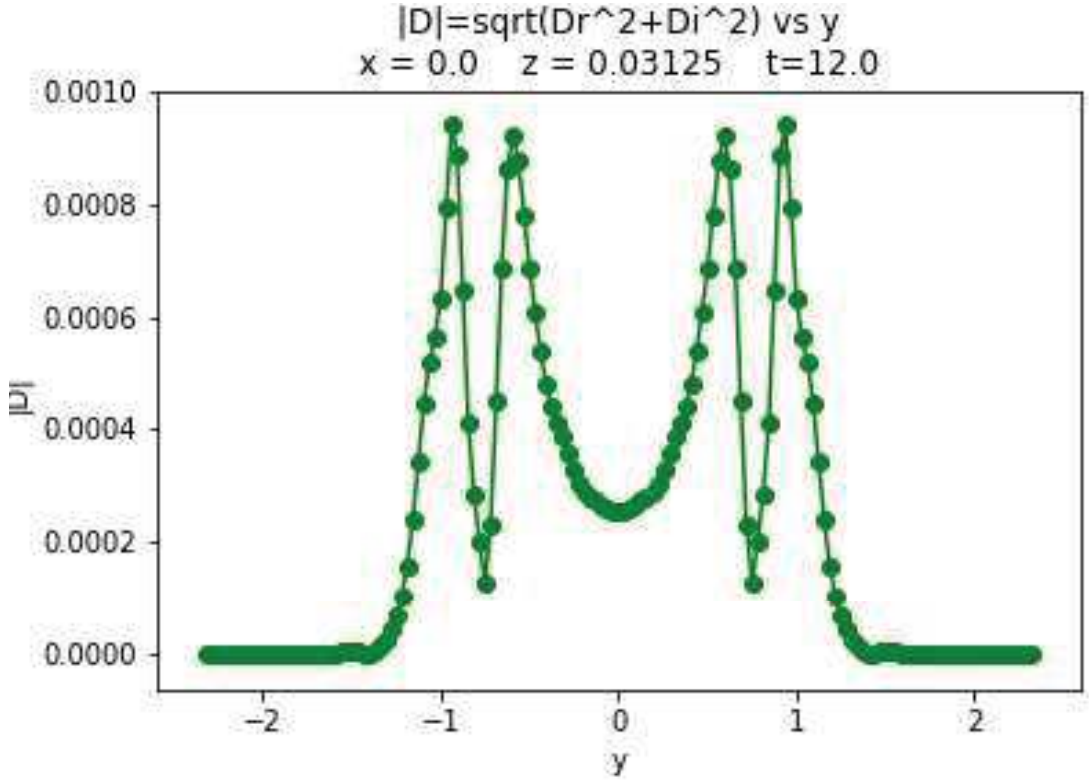

Figure 36: T = 12, x = 0.03125

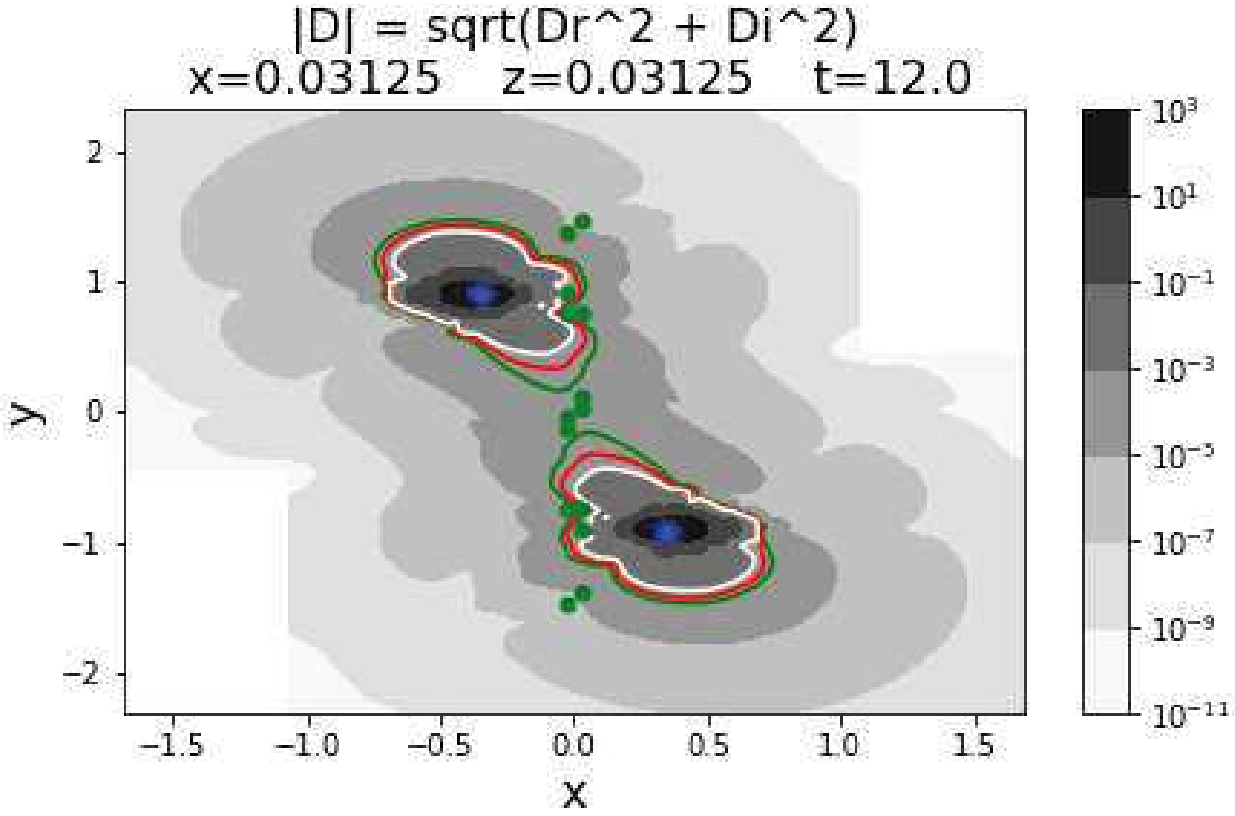

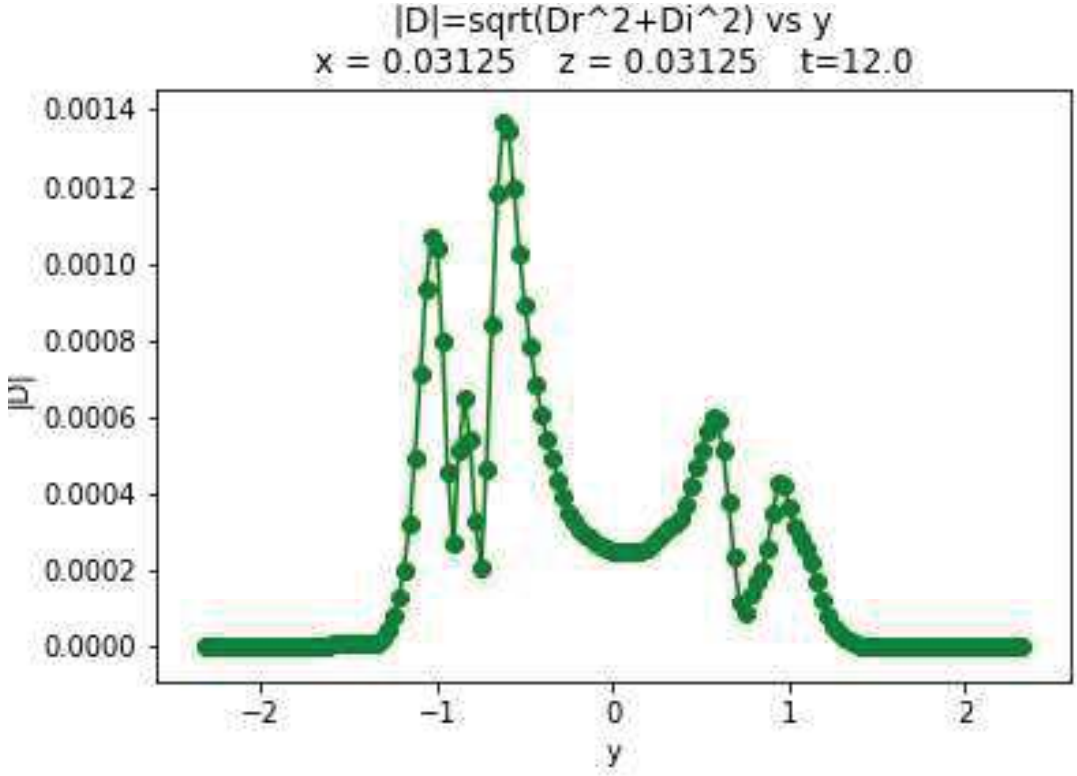

Figure 37: T = 12, x = 0.125

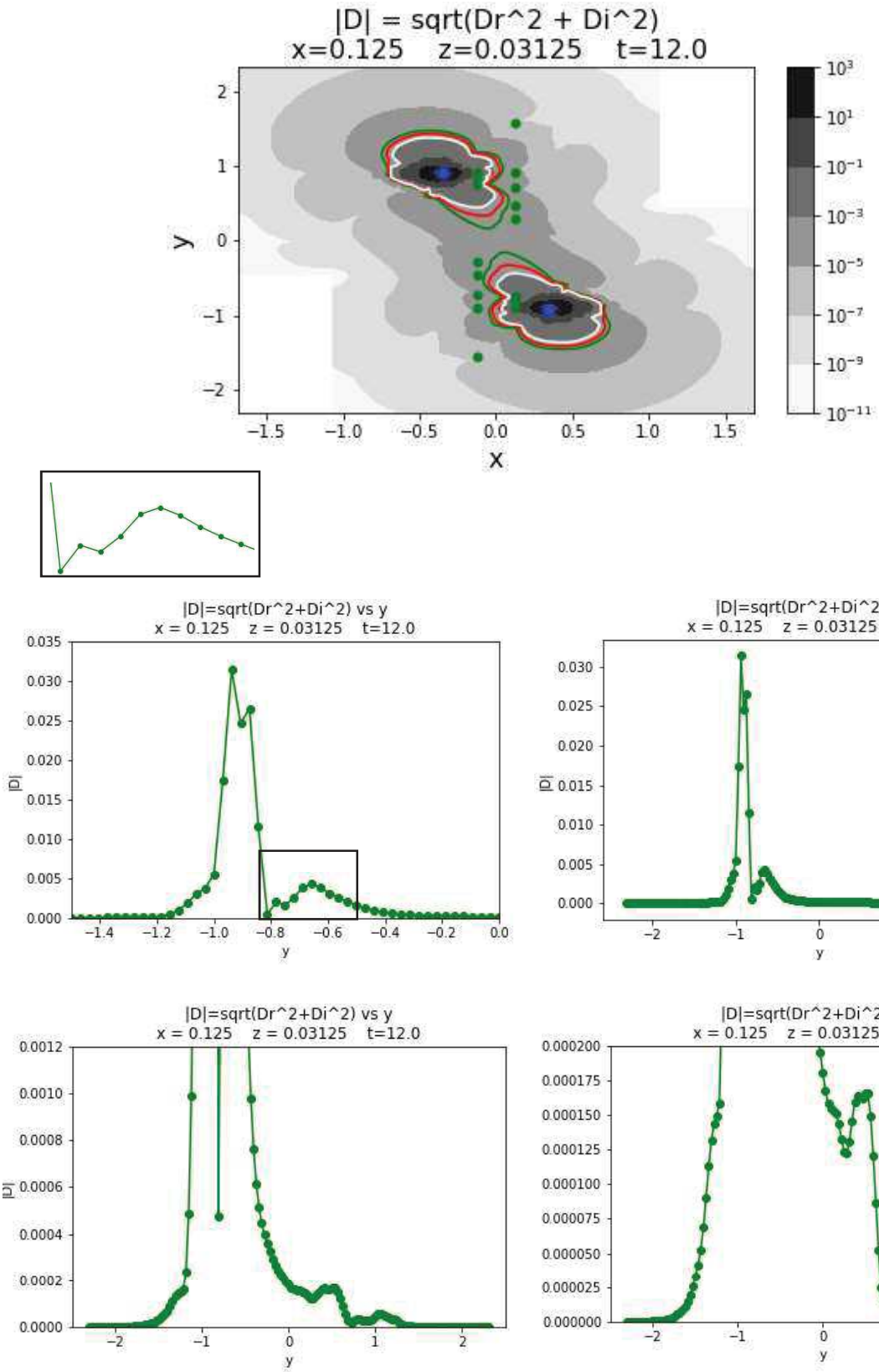

Figure 38: T = 12, x = 0.28125

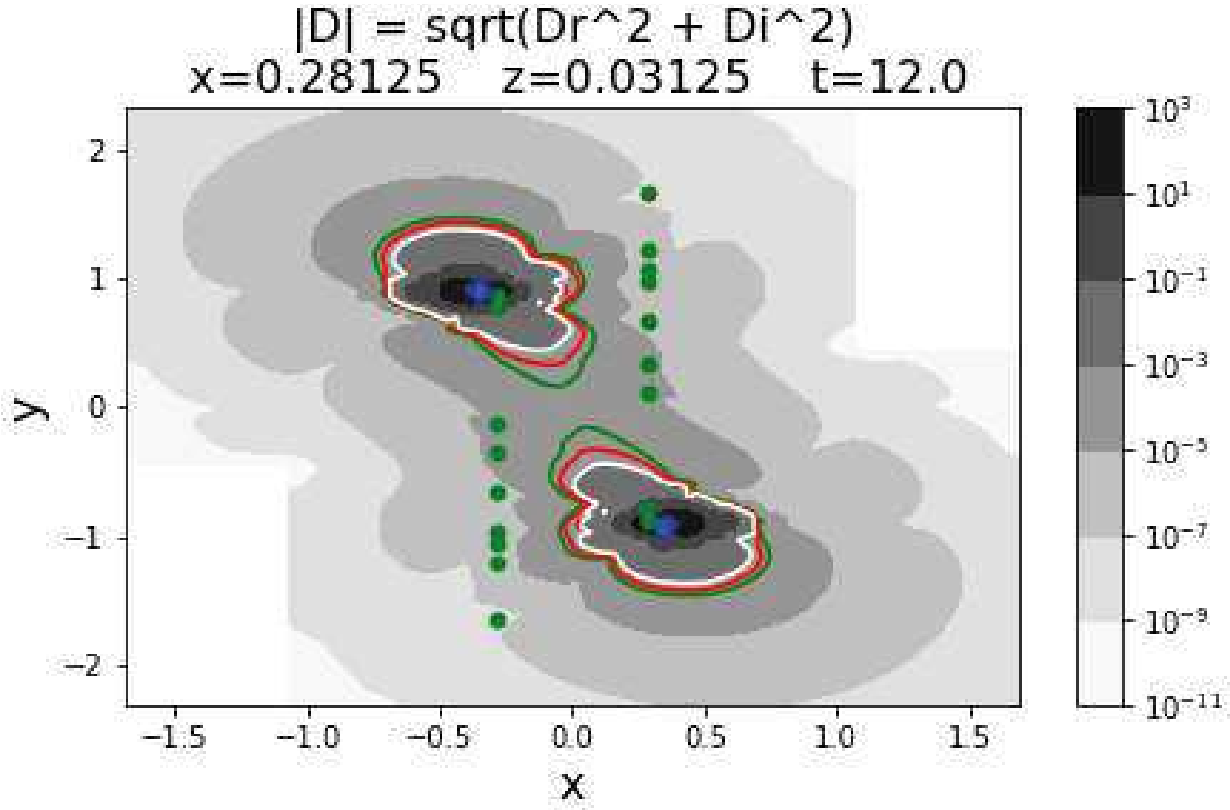

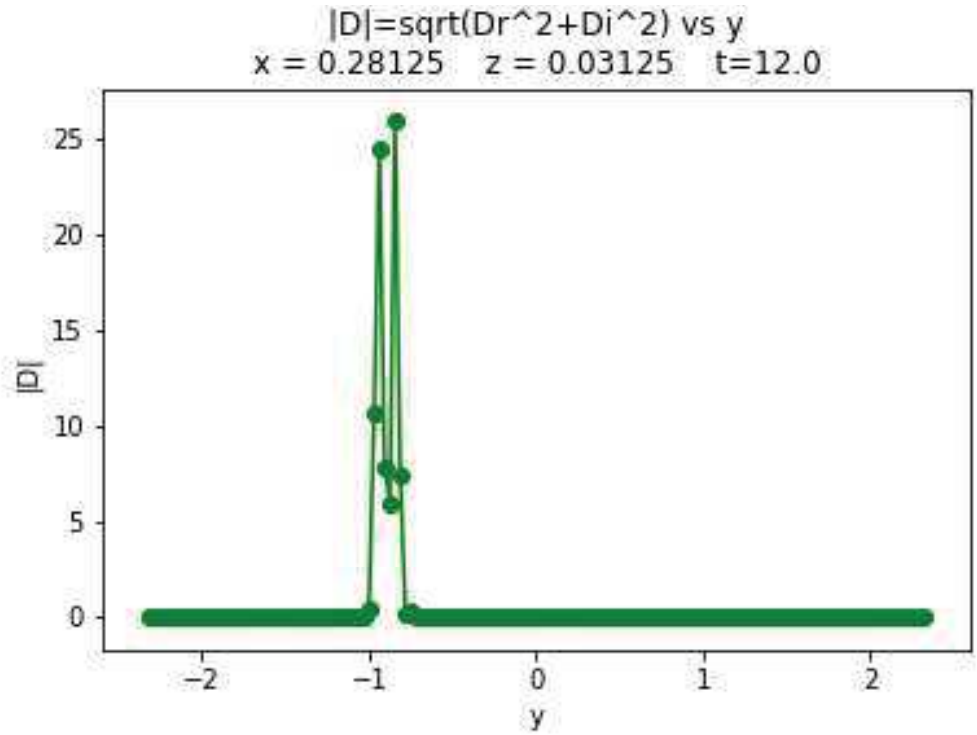

Figure 39: T = 12, x = 0.65625

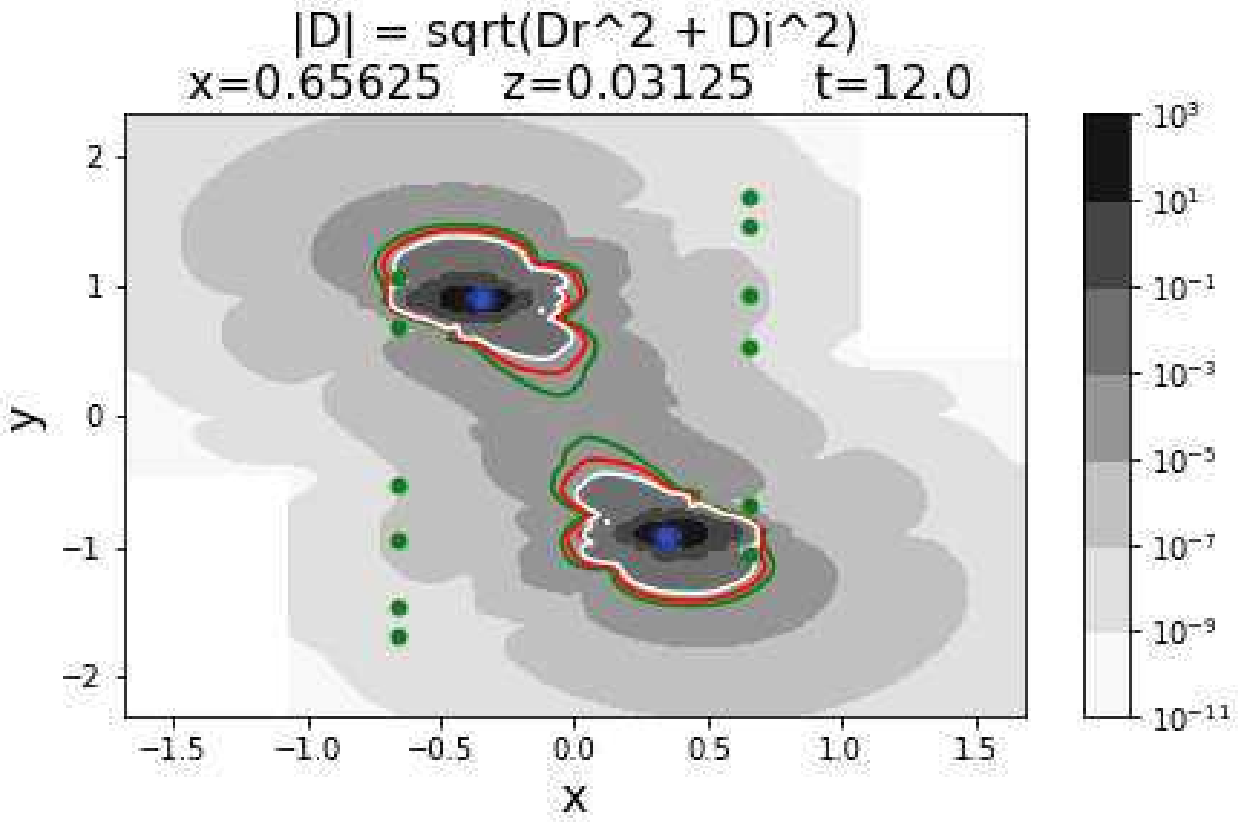

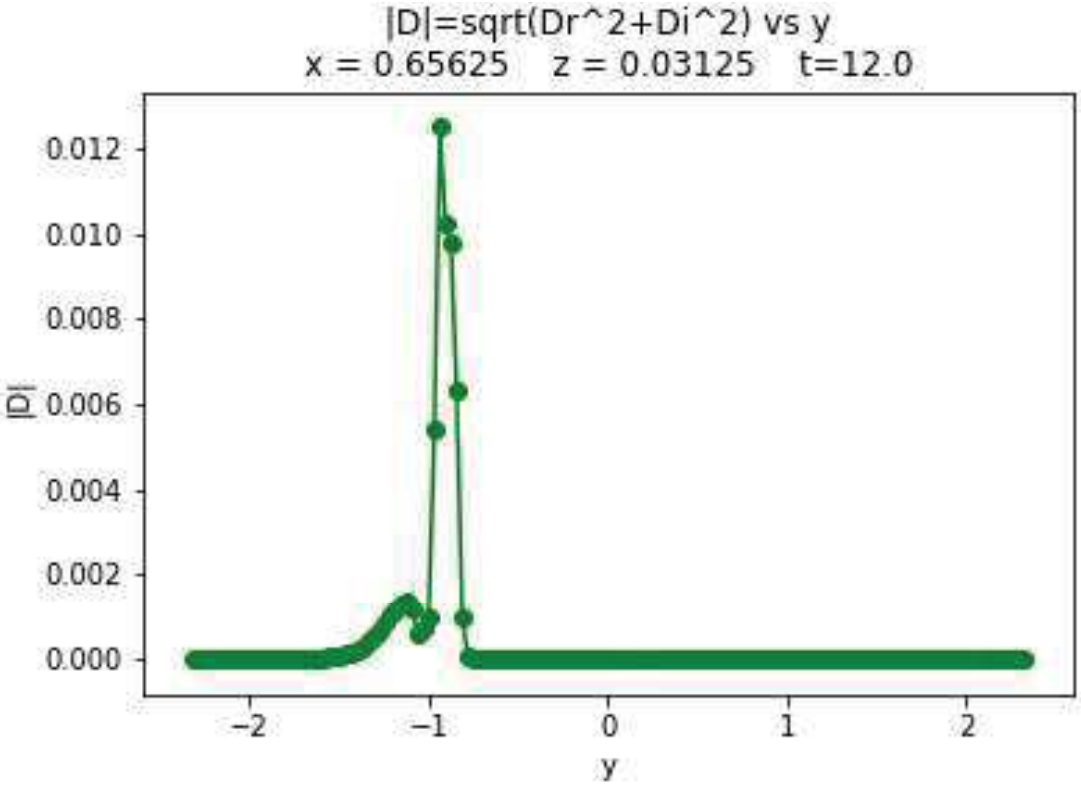

Figure 40: T = 16, x = 0

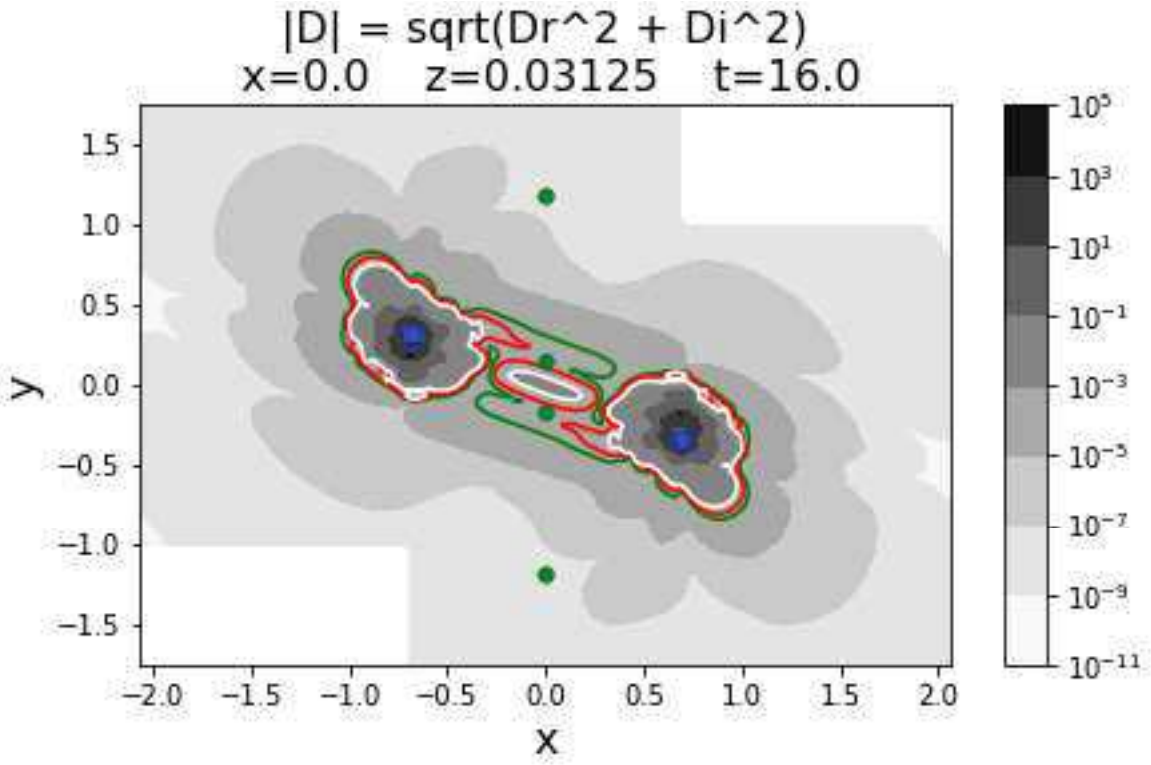

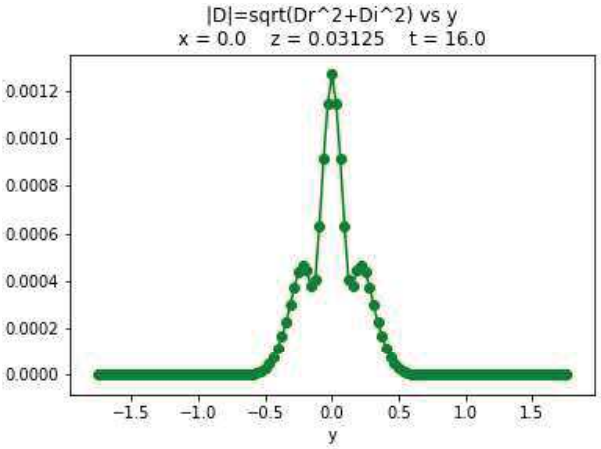

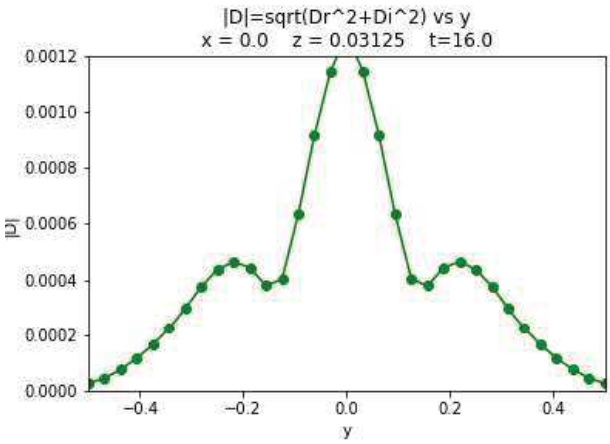

Figure 41: T = 16, x = 0.0625

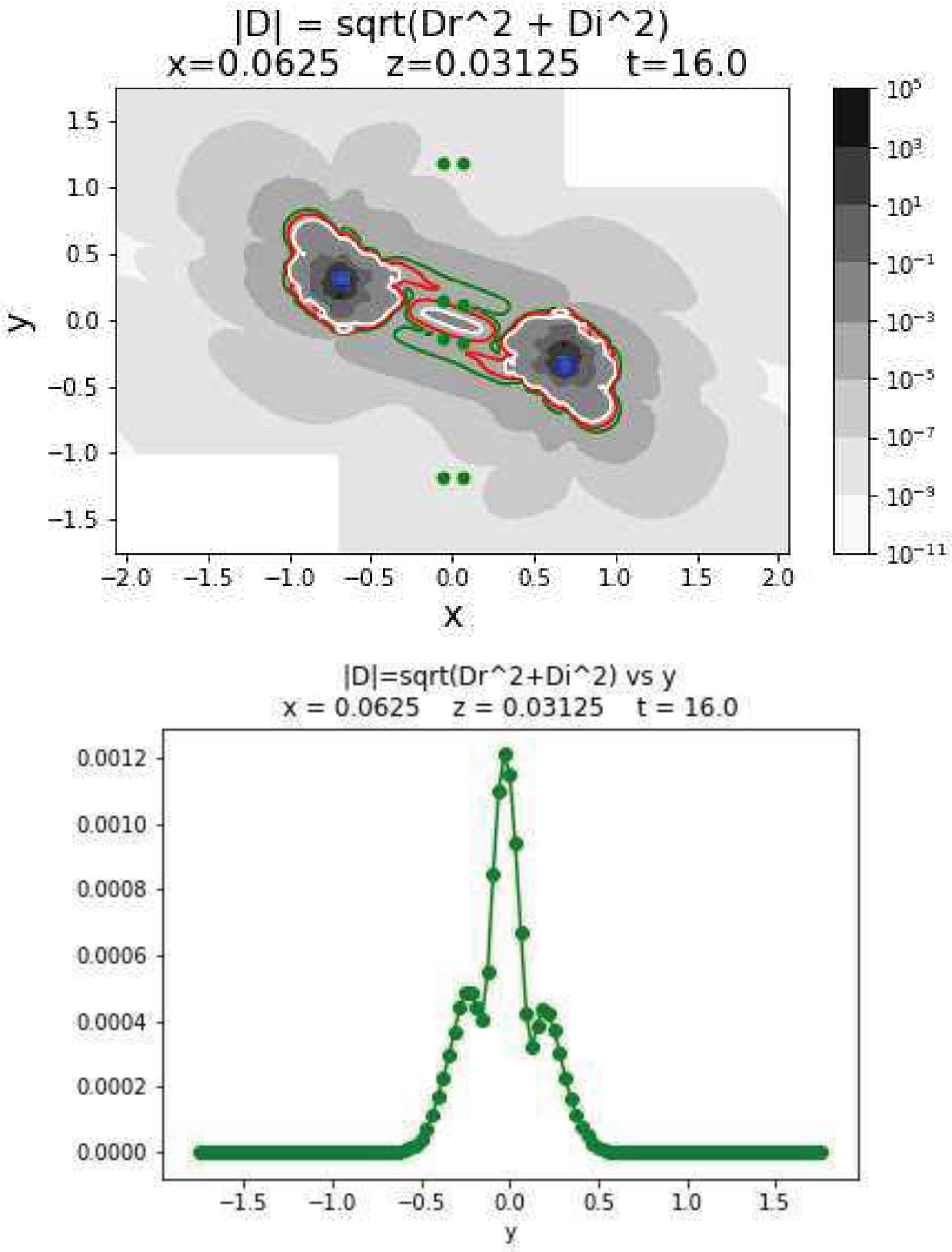

Figure 42: T = 16, x = 0.25

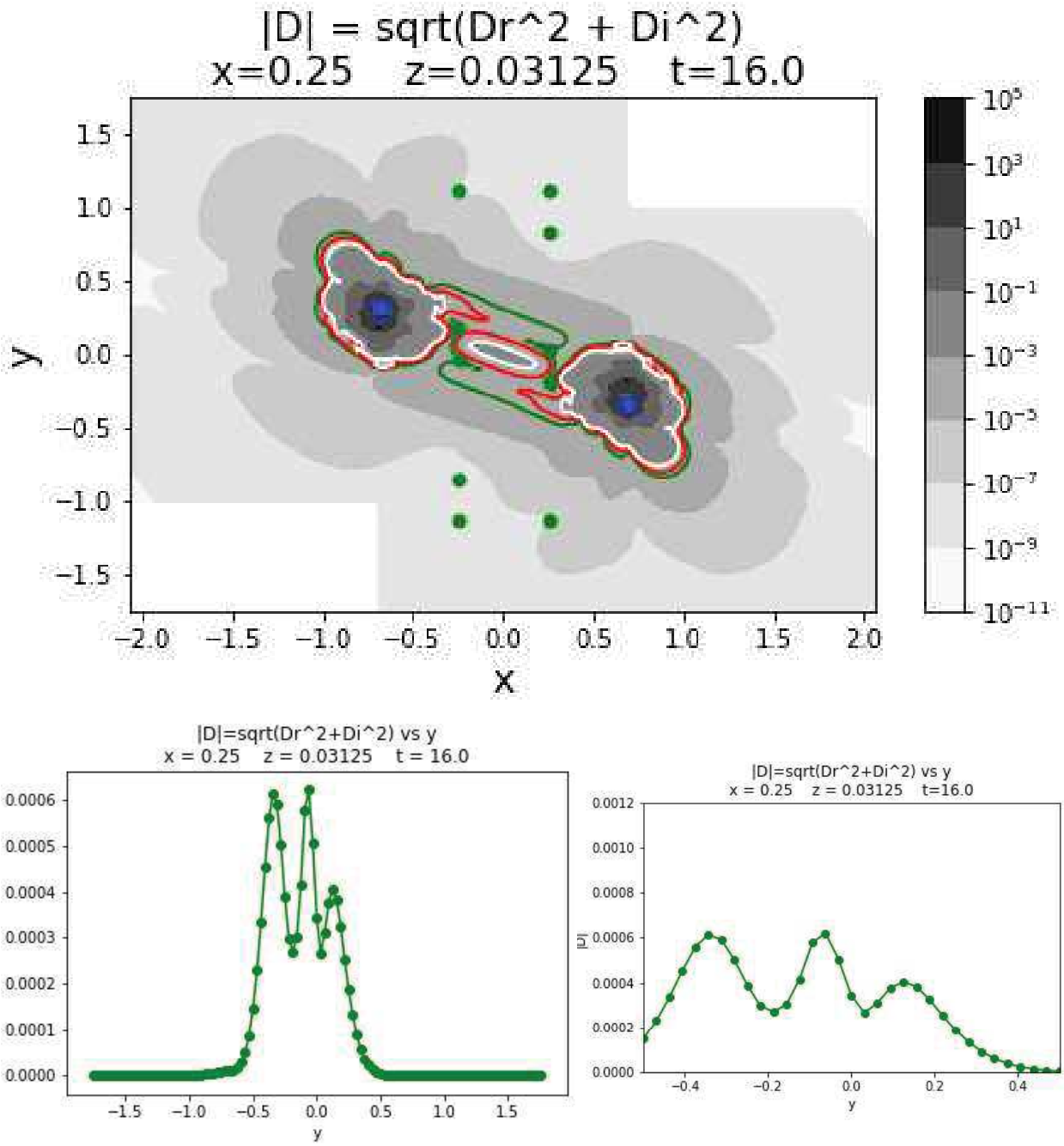

Figure 43: T = 16, x = 0.3125

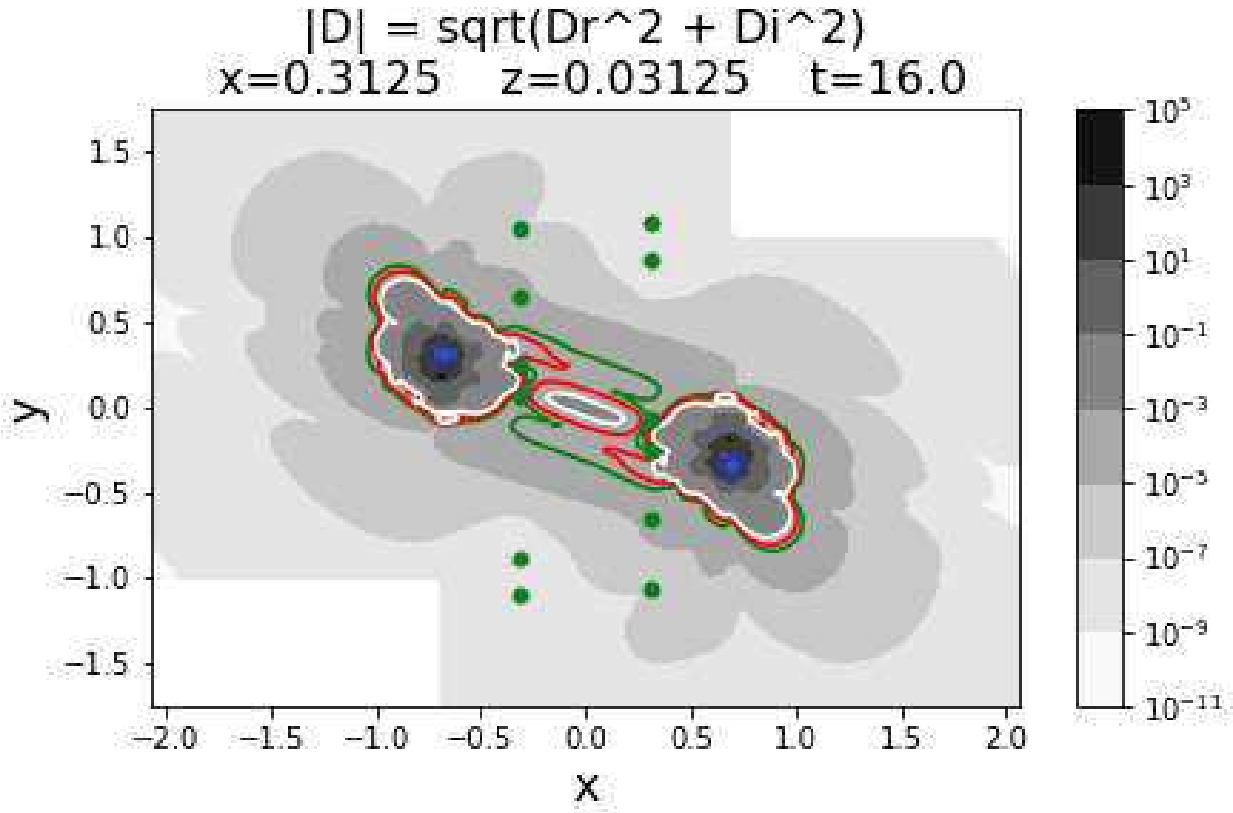

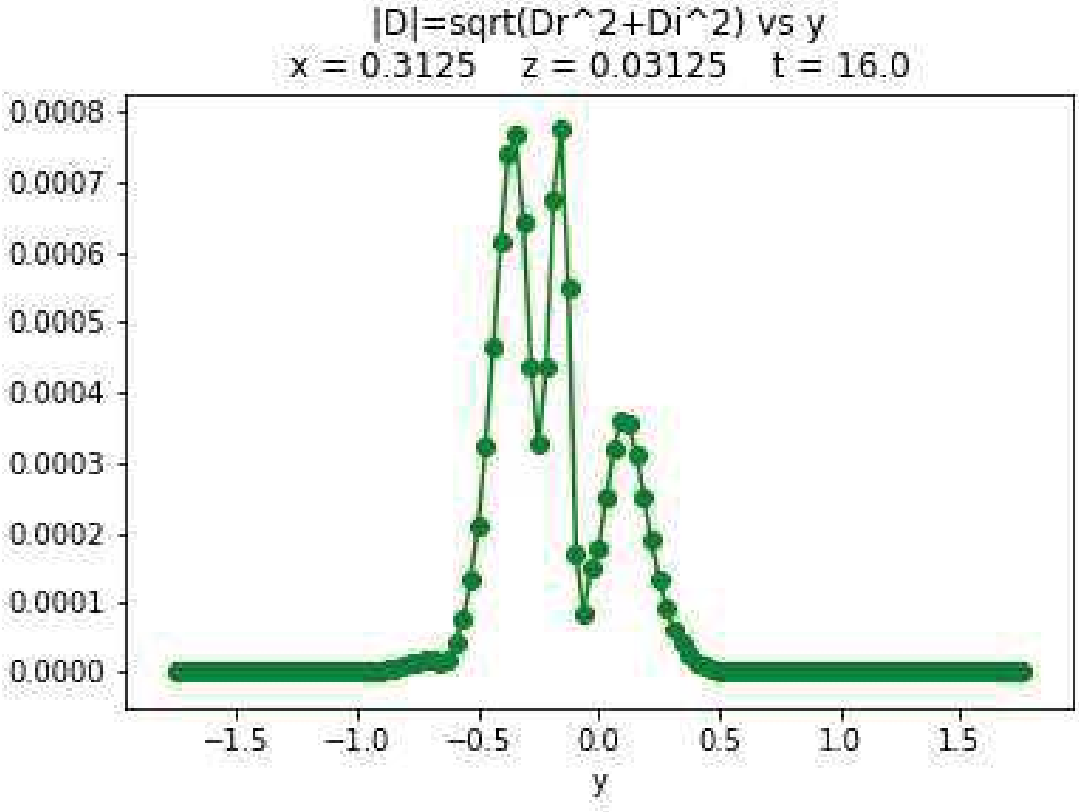

Figure 44: T = 16, x = 0.5

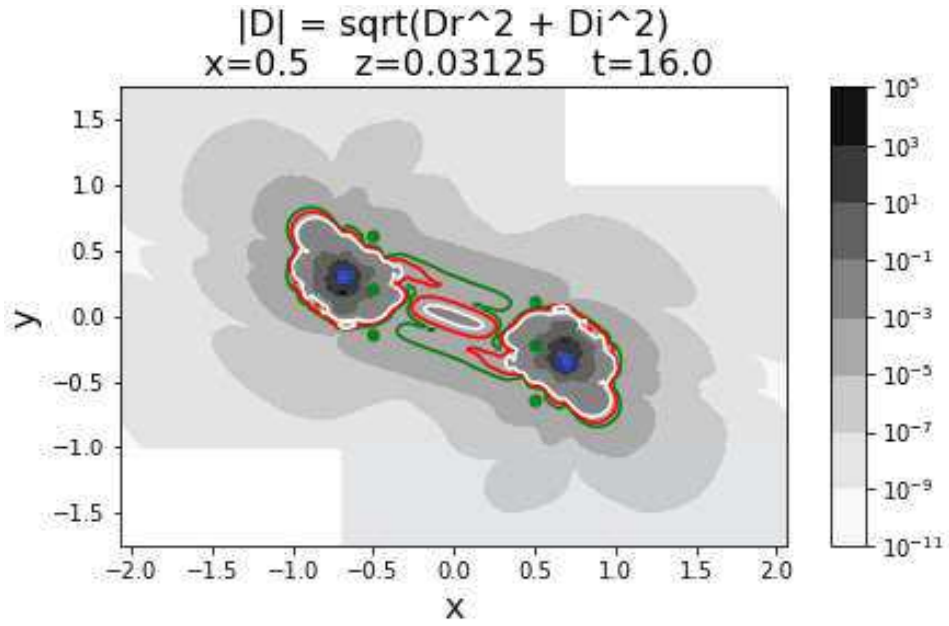

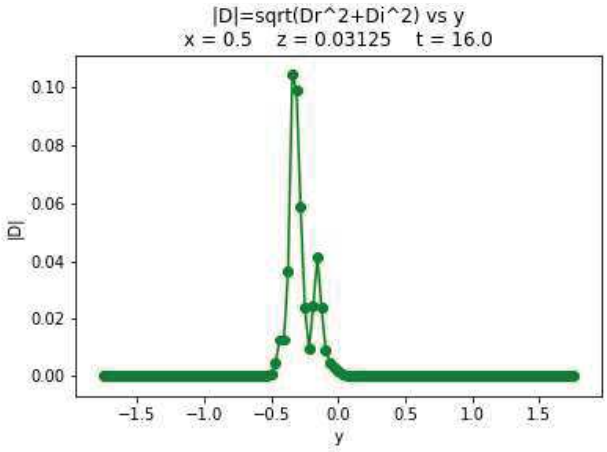

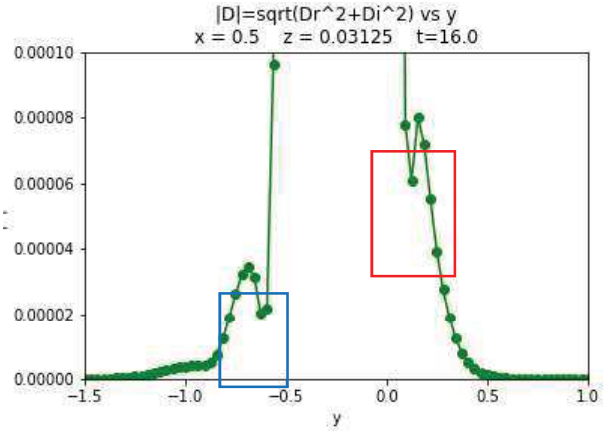

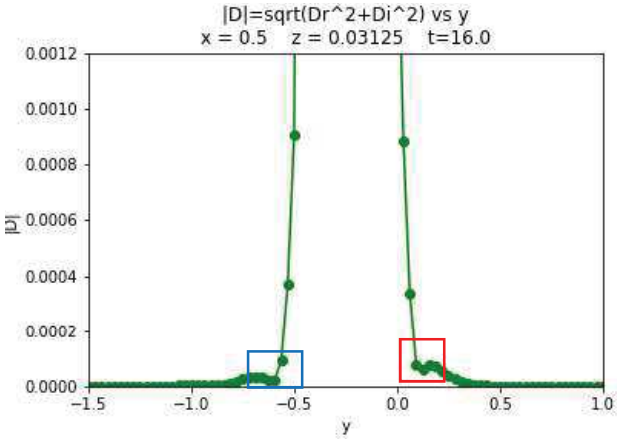

Figure 45: T = 16, x = 0.75

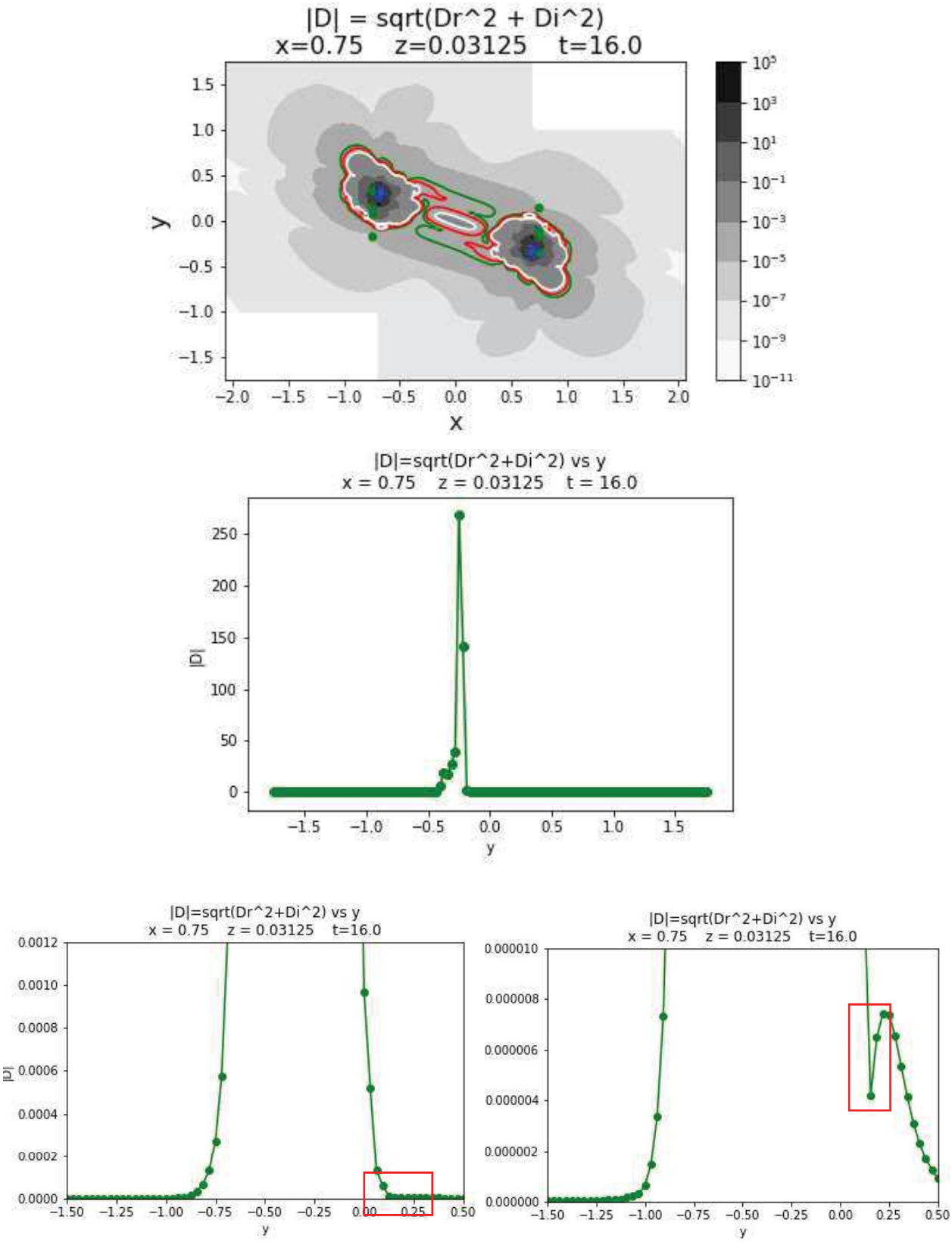

Figure 46: T = 16, x = 1.0

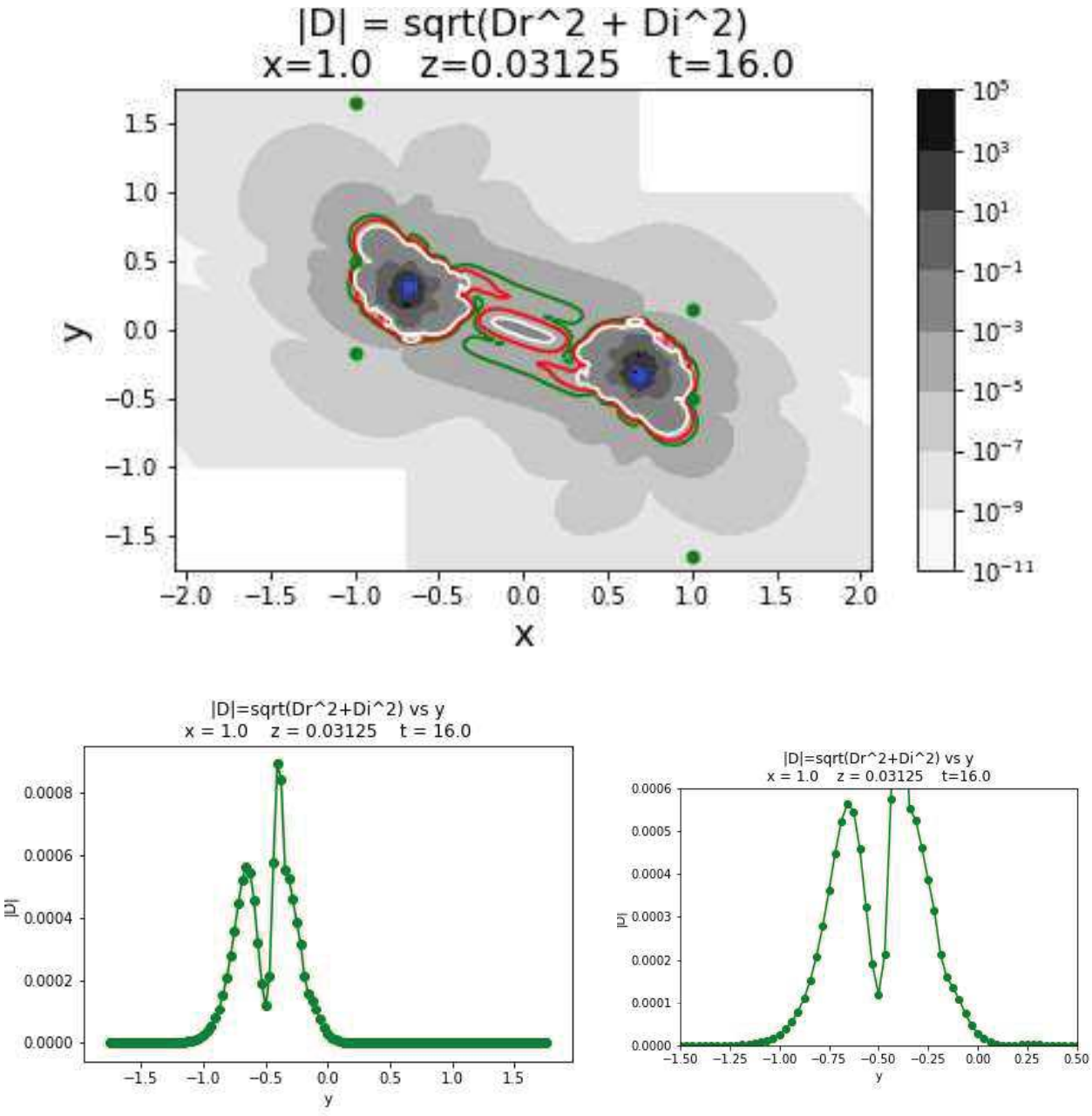

Figure 47: T = 20, x = 0.125

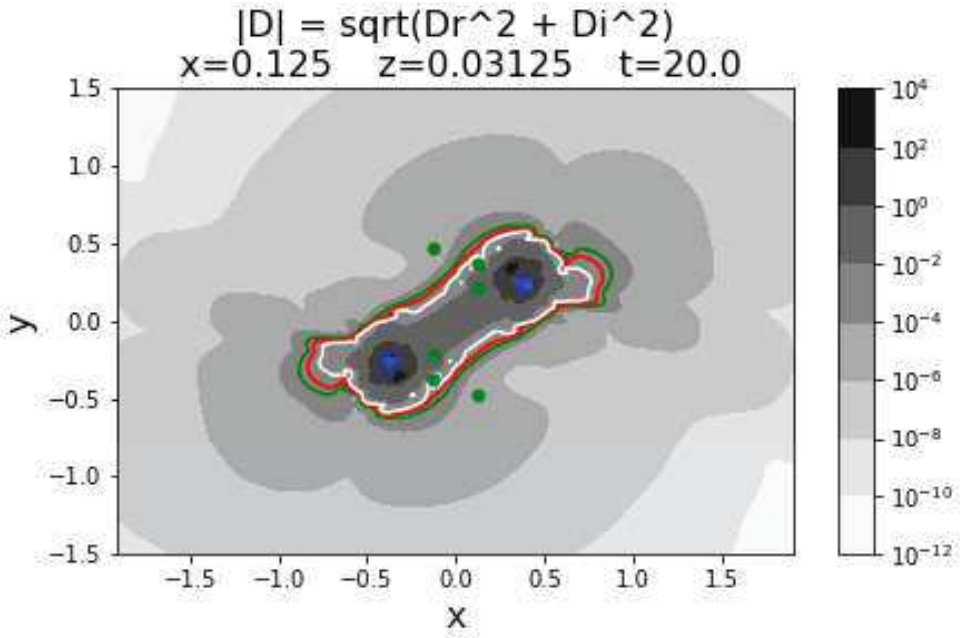

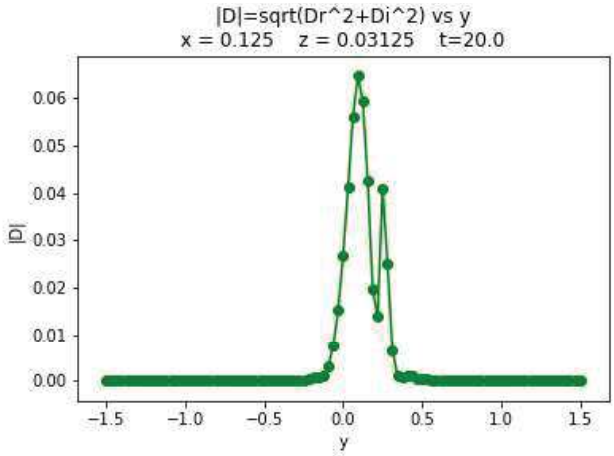

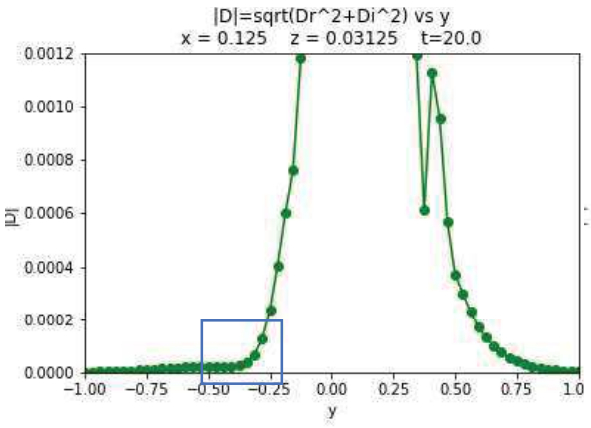

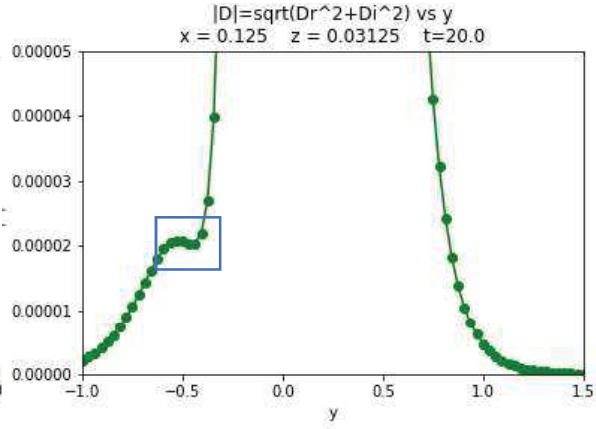

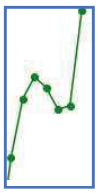

Figure 48: T = 20, x = 0.375

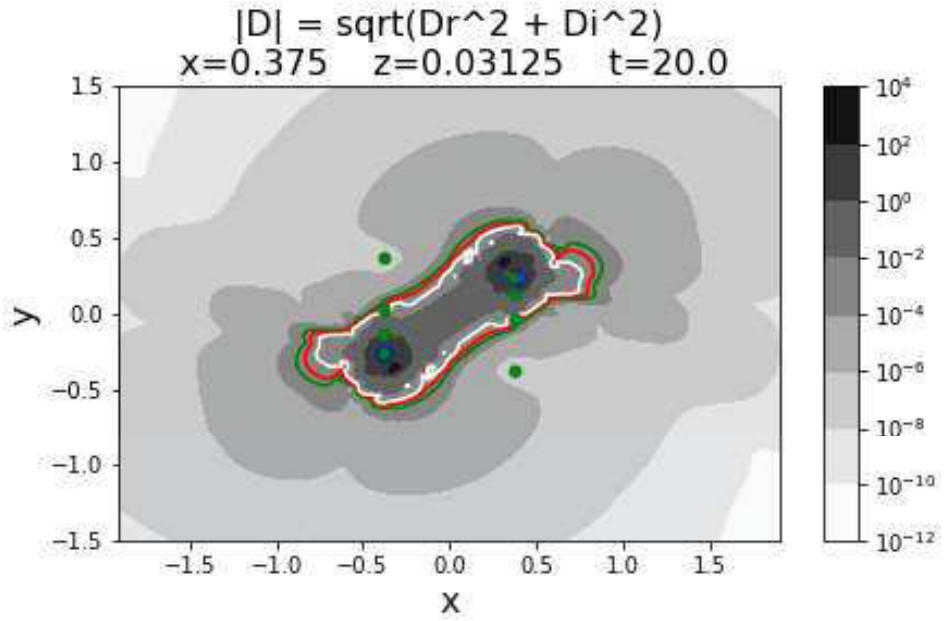

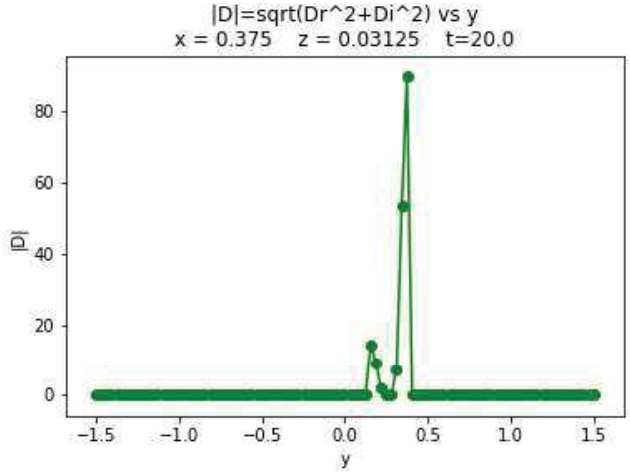

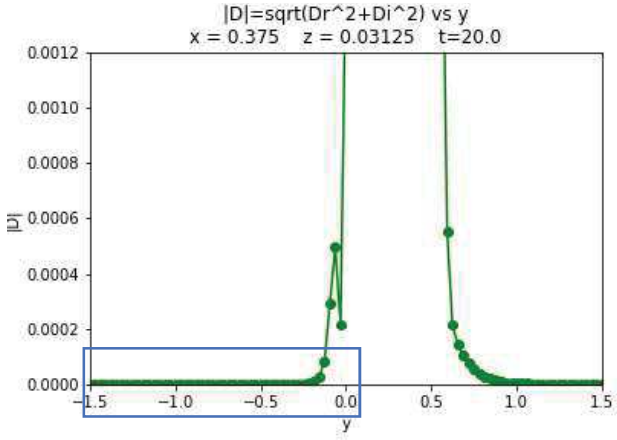

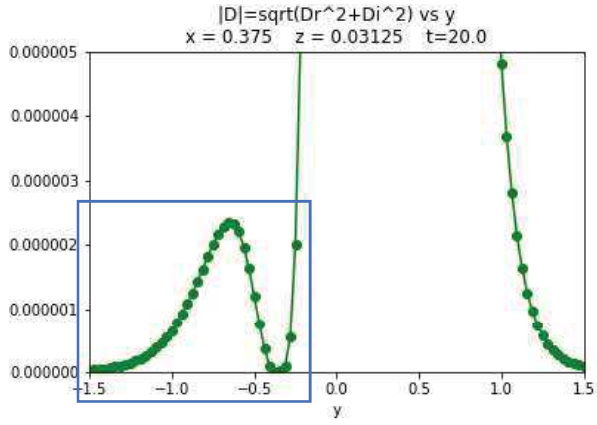

Figure 49: T = 20, x = 0.5

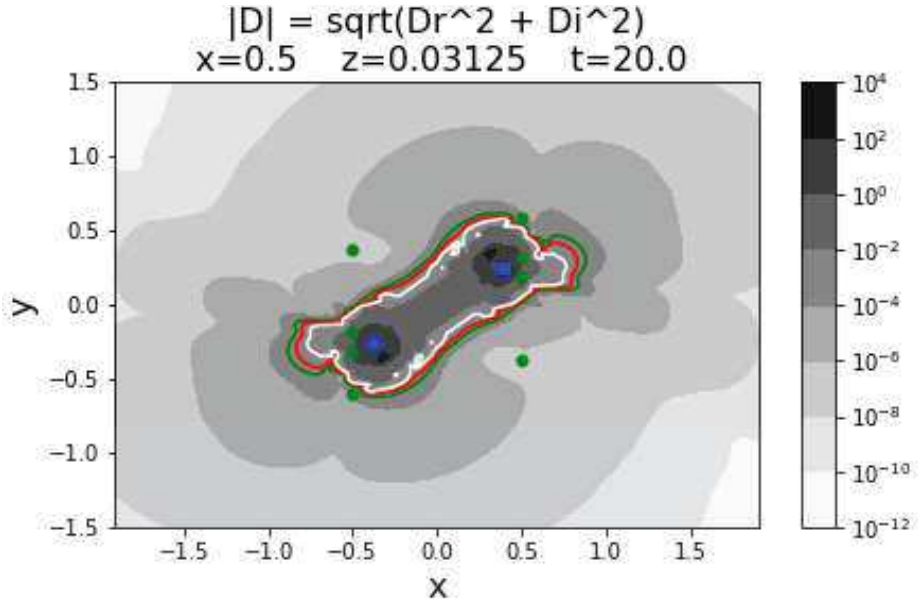

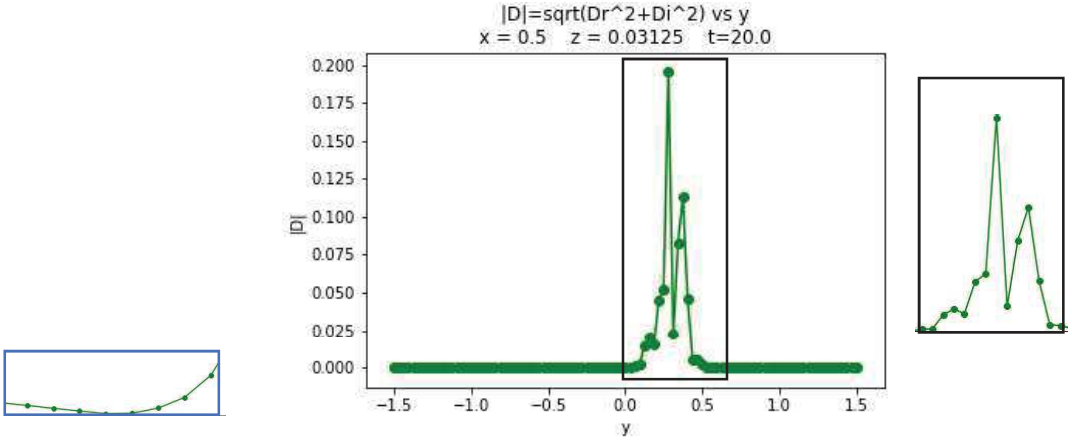

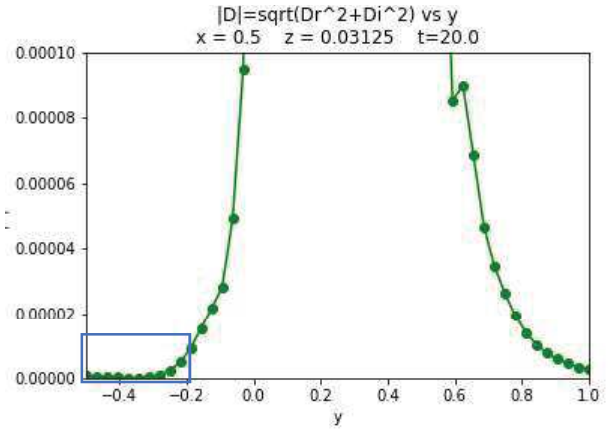

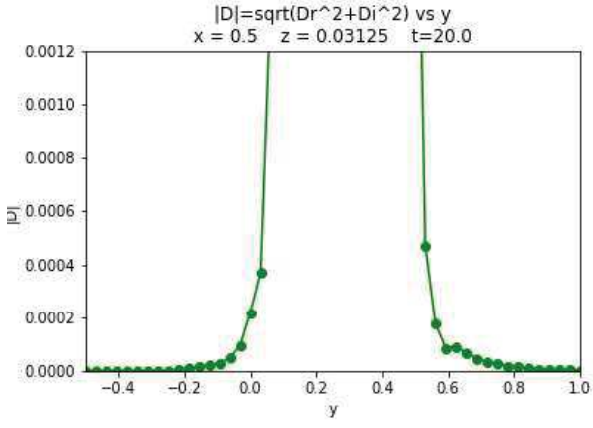

Figure 50: T = 20, x = 0.625

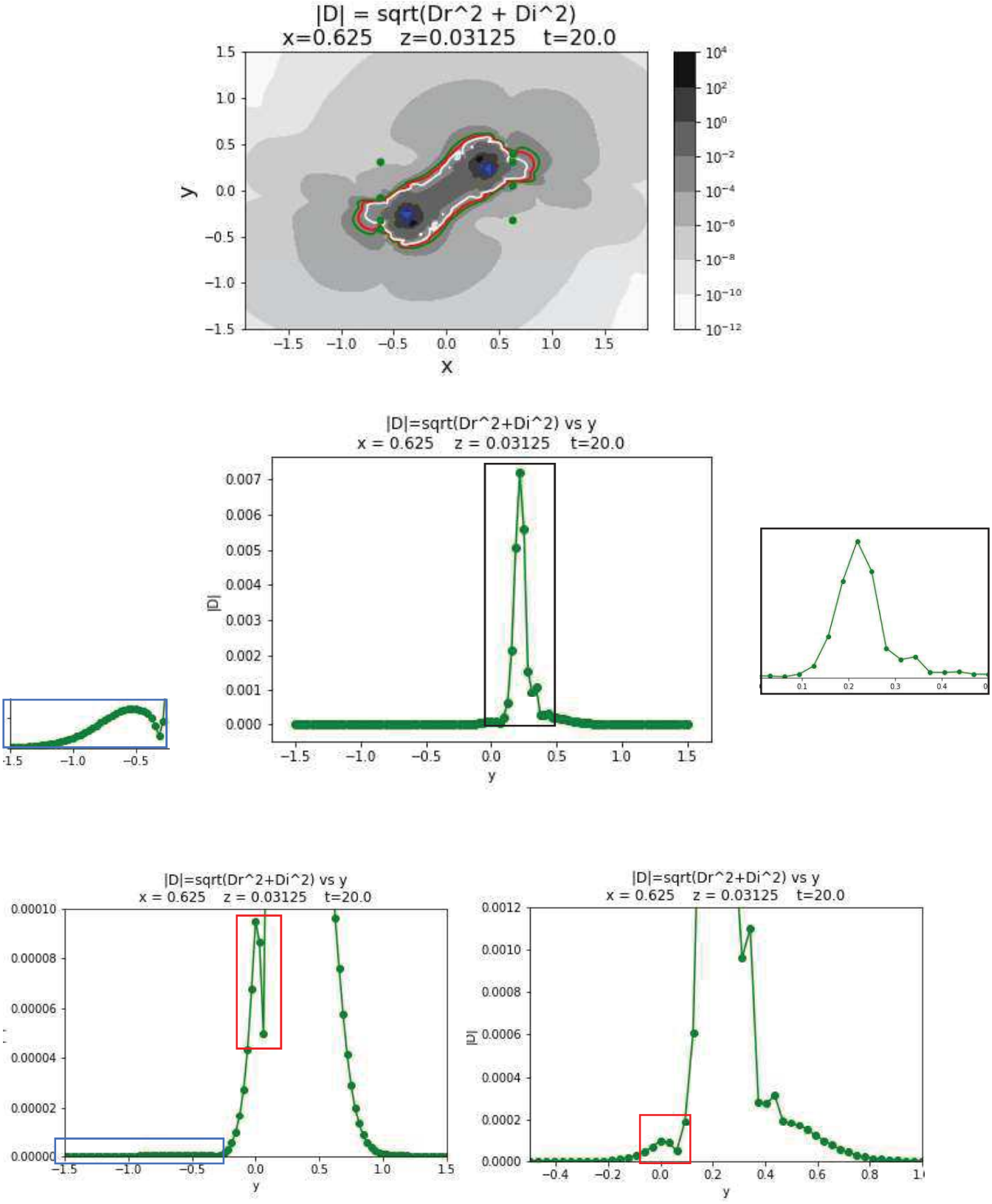

Figure 51: T = 20, x = 0.75

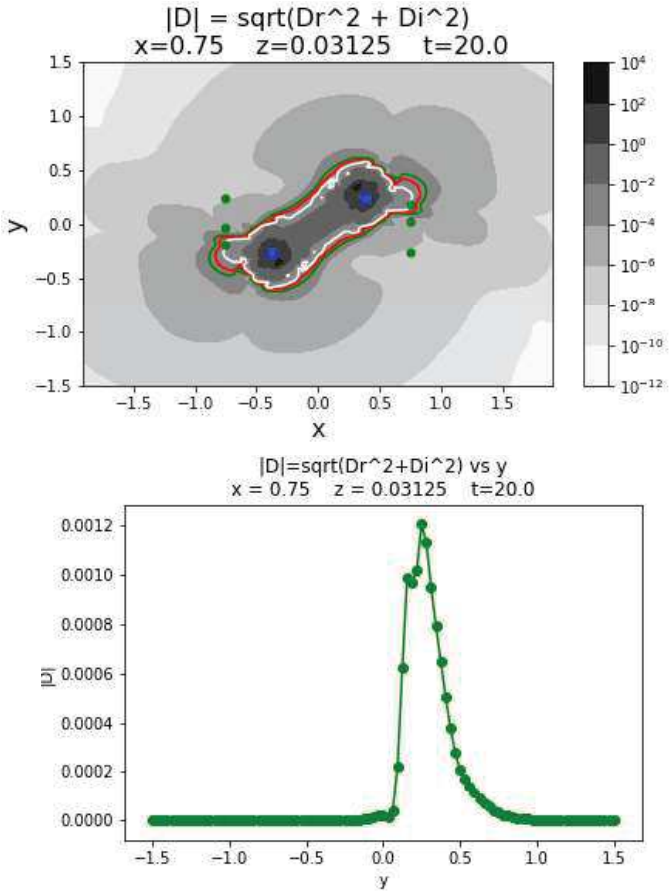

Figures 52-55: Plotting all local minima from slice plots taken from Figures 35-51 at the respective times T = 12, 16, 20, and 24.

Legend for Figures 52-55:

- Upper left plots: Plots of local minima of |D| considering only neighbouring values of |D| as taken along constant x sections.
- Upper right plots: Plots of local minima of |D| considering only neighbouring values of |D| as taken along constant y sections.
- Lower plots: Plots of Dr.
- Green dots: Local minima of |D| taken along the x-direction (for lower left plot) or along the y-direction (for lower right plot).
- Green curves: level 0.0003 sets of |D|.
- Red curves: level 0.0005 sets of |D|.
- White curves: level 0.001 sets of |D|.
- Deep pink curves: level 0 sets of Dr, where Dr is cut off to lie in the range [-1,1] (see description for Figures 1-34).
- Blue dots: centroids of MOTSs of initial BHs.

Figure 52: T = 12

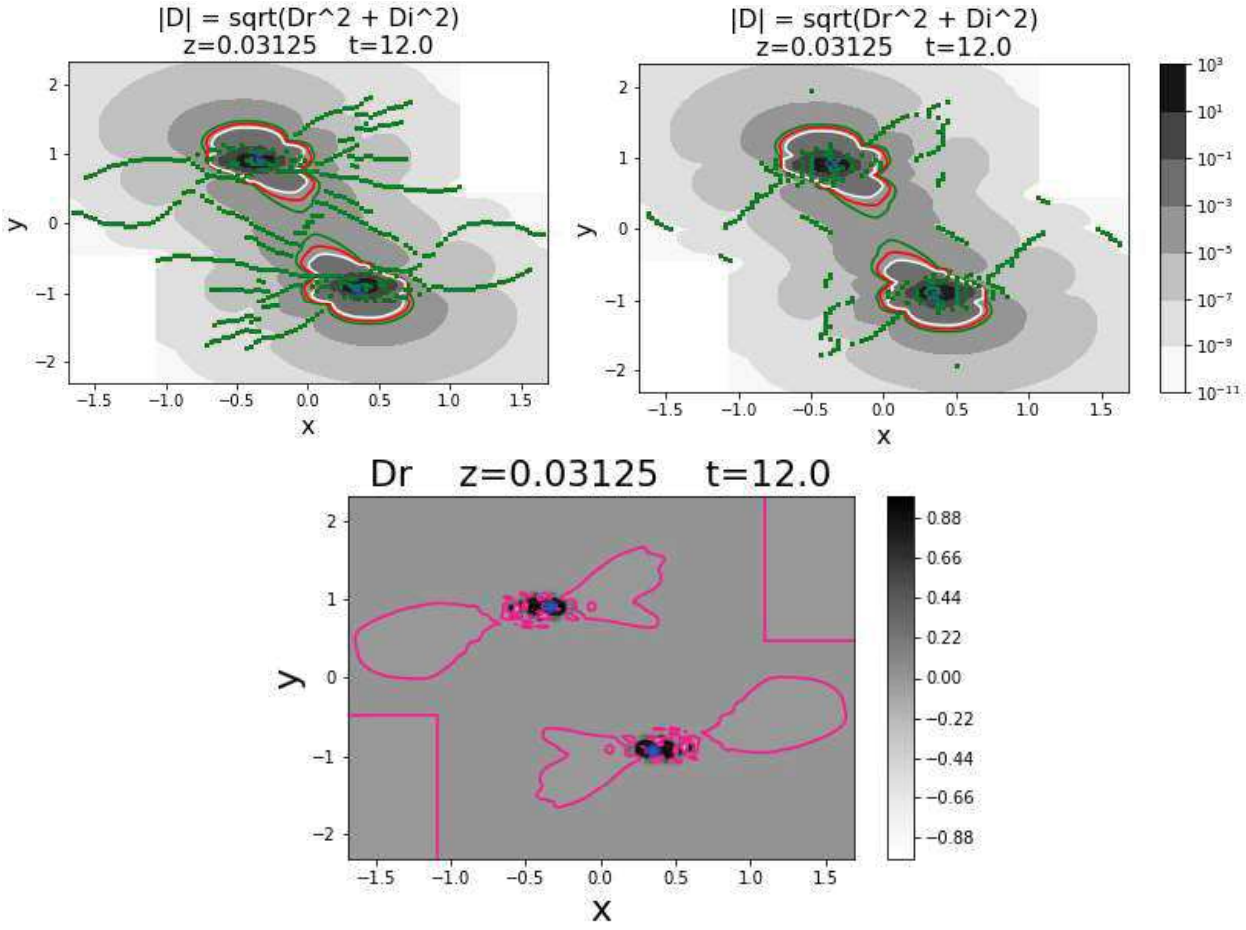

Figure 53: T = 16

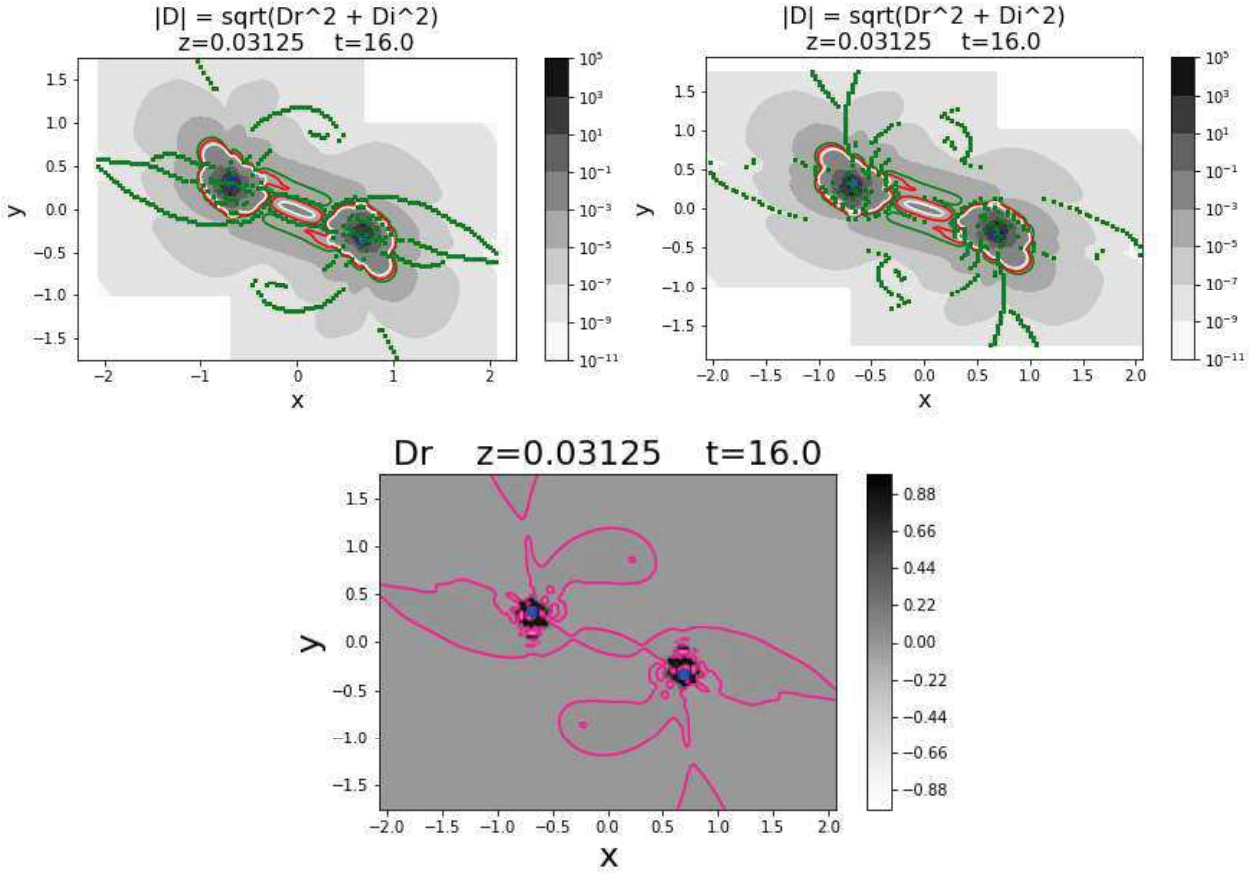

Figure 54: T = 20

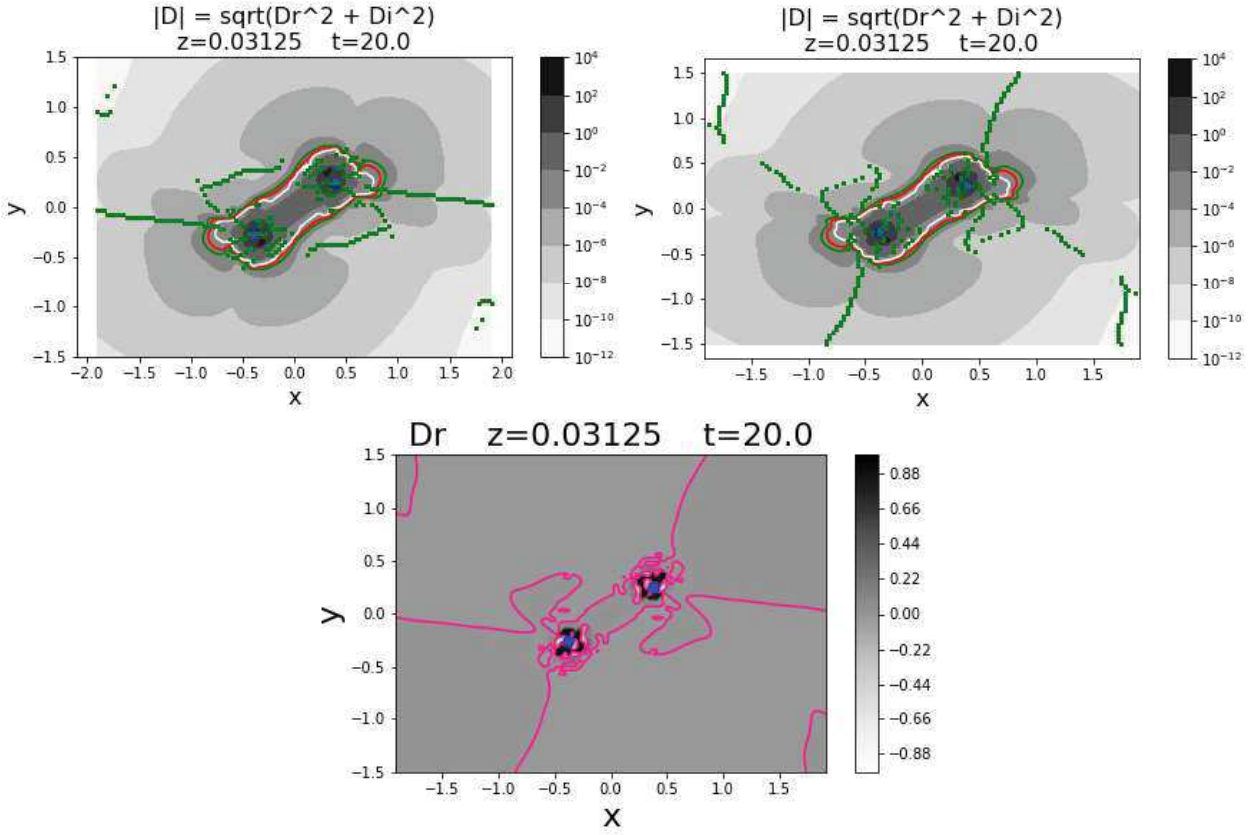

Figure 55: T = 24

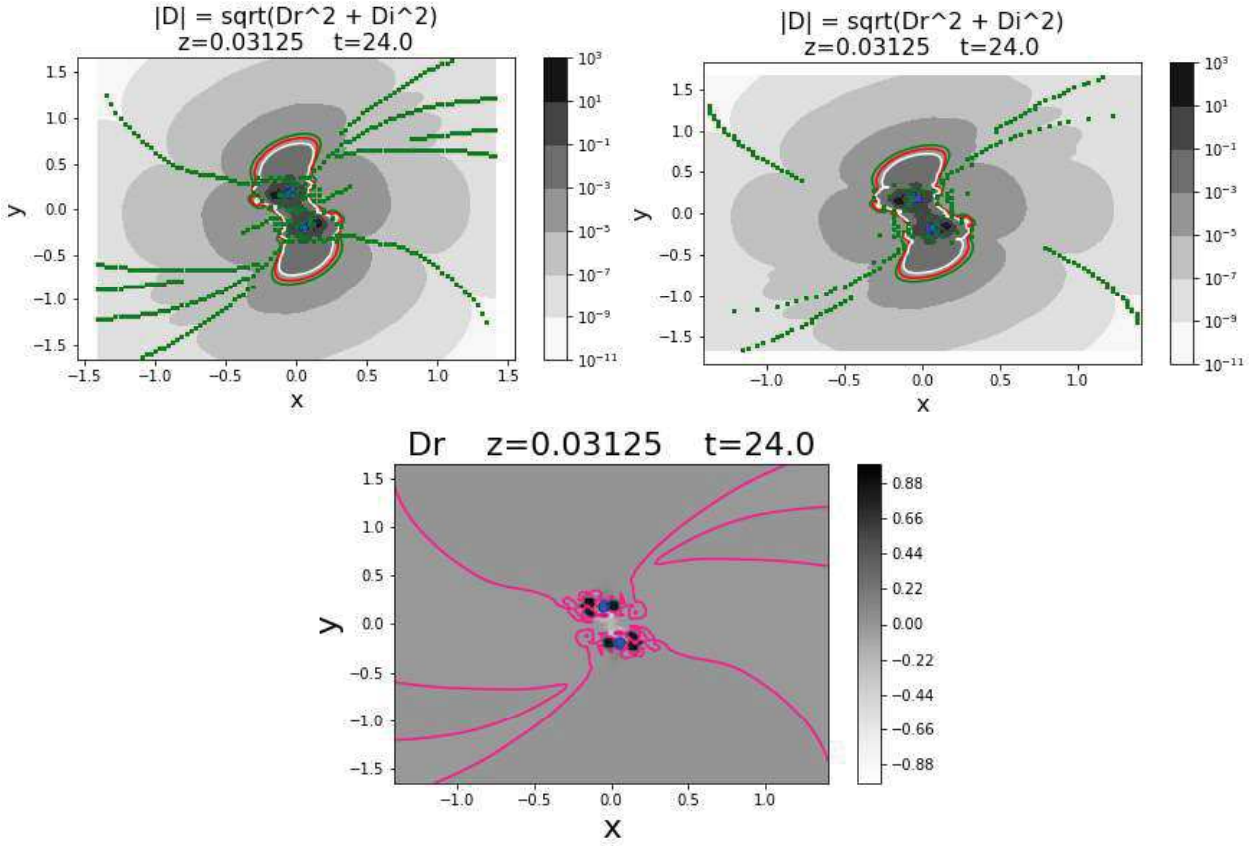

Figures 56-59: Comparing plots of local minima along the x direction from Figures 52-56 with level 0.0003 sets of |D|.

Legend for Figures 56-59:

- Top plot: Plot of |D| vs position at the time indicated
- Bottom plot: Plot of |D| vs position at the time indicated with magnified resolution
- Green curves: Level 3e-4 curves of |D|
- White curves: Level 1e-3 curves of |D|
- Green dots: Plots of local minima of |D| taken along sections of constant x, restricted to lie between 0.0001 and 0.0012
- Blue dots: Centroids of MOTSs of initial BHs

Figure 56: T = 12

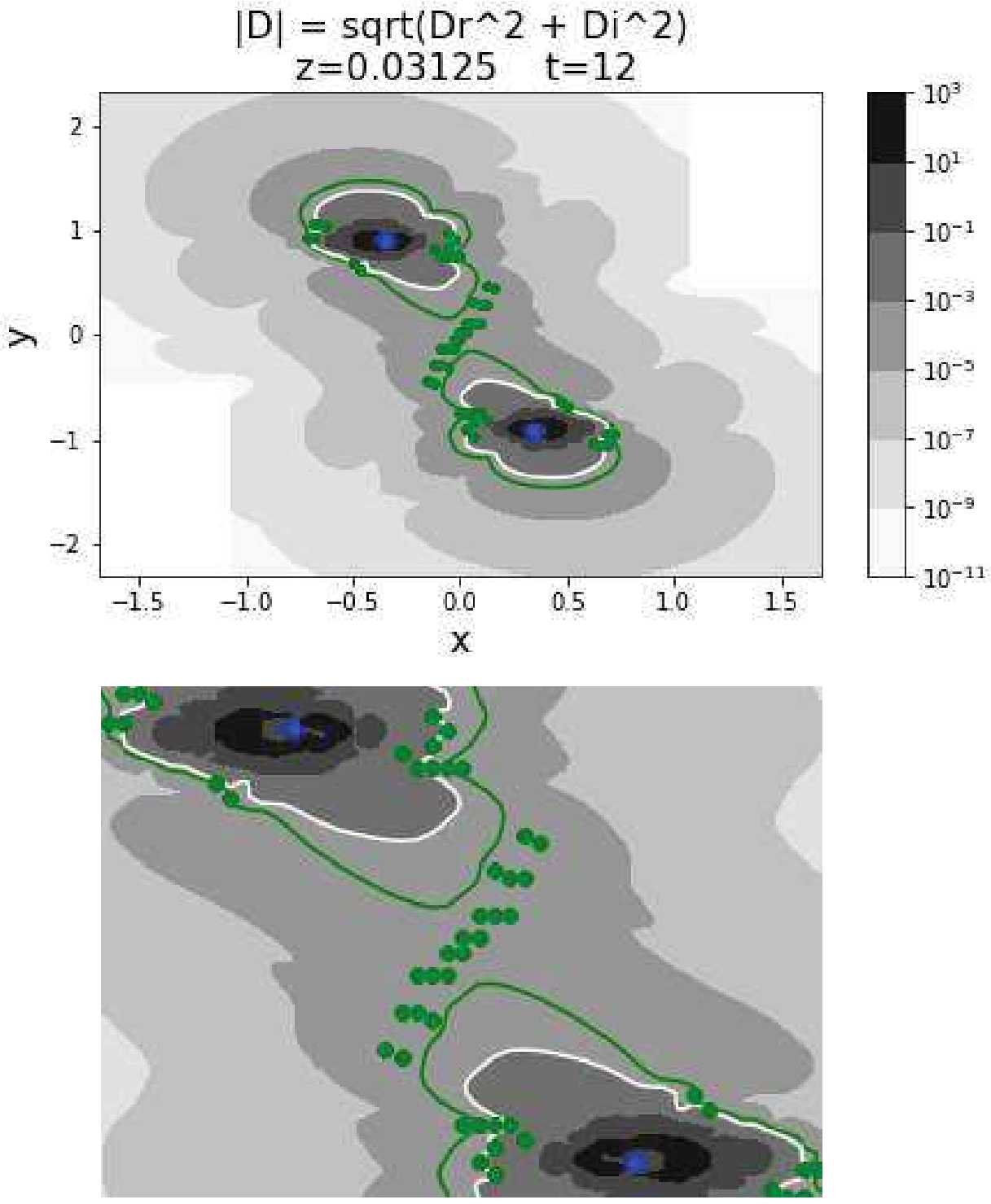

Figure 57: T = 16

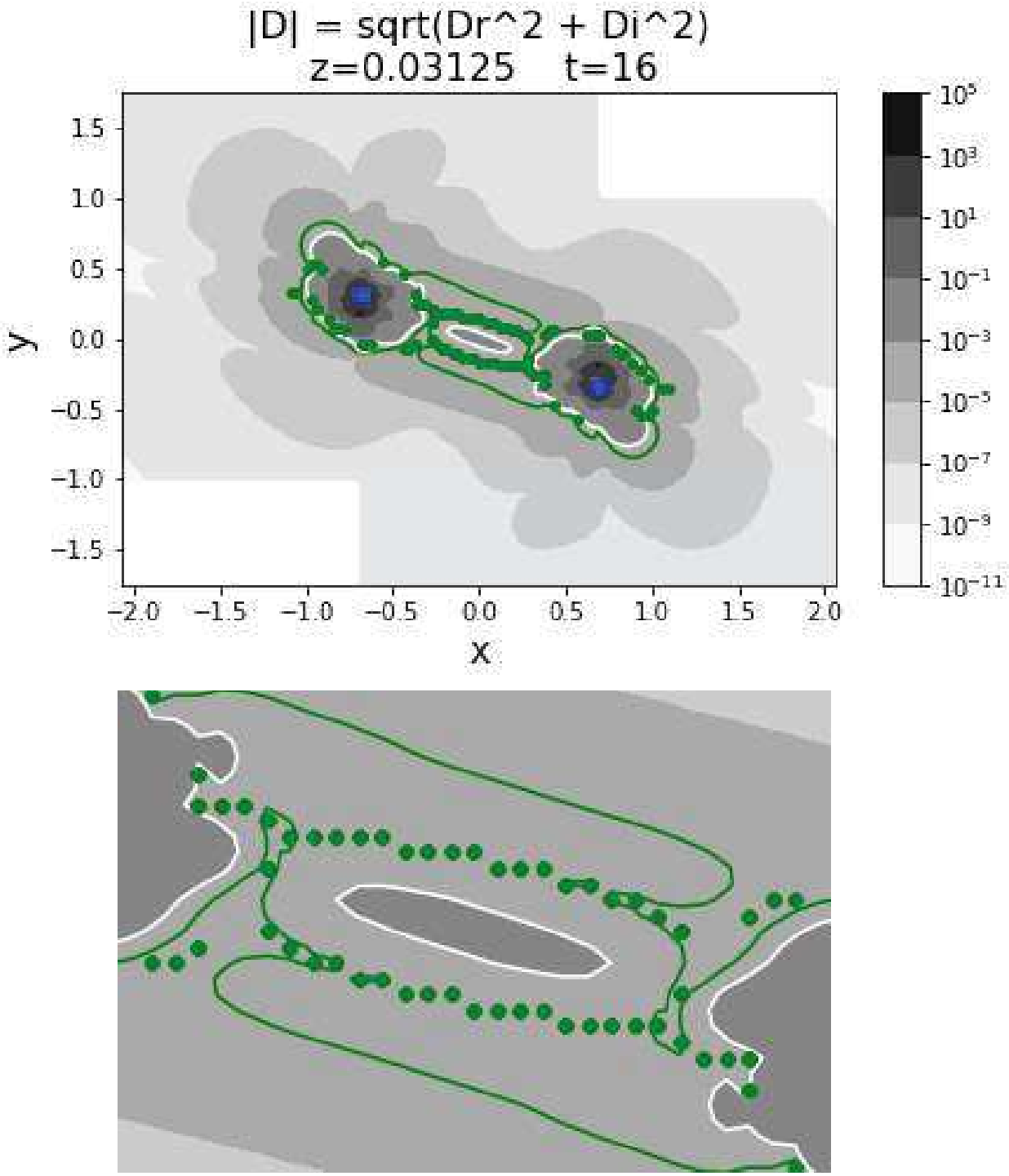

Figure 58: T = 20

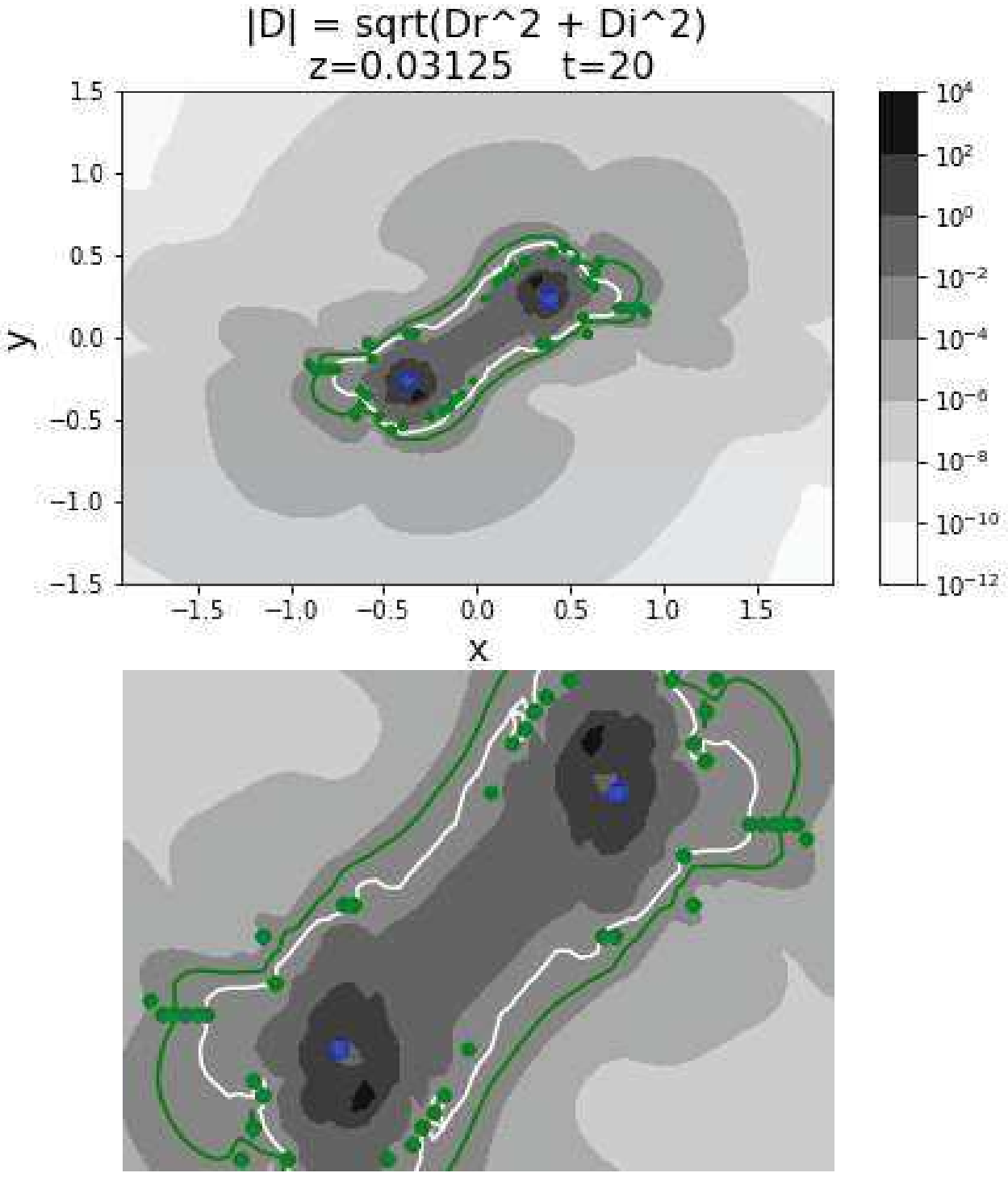

Figure 59: T = 24

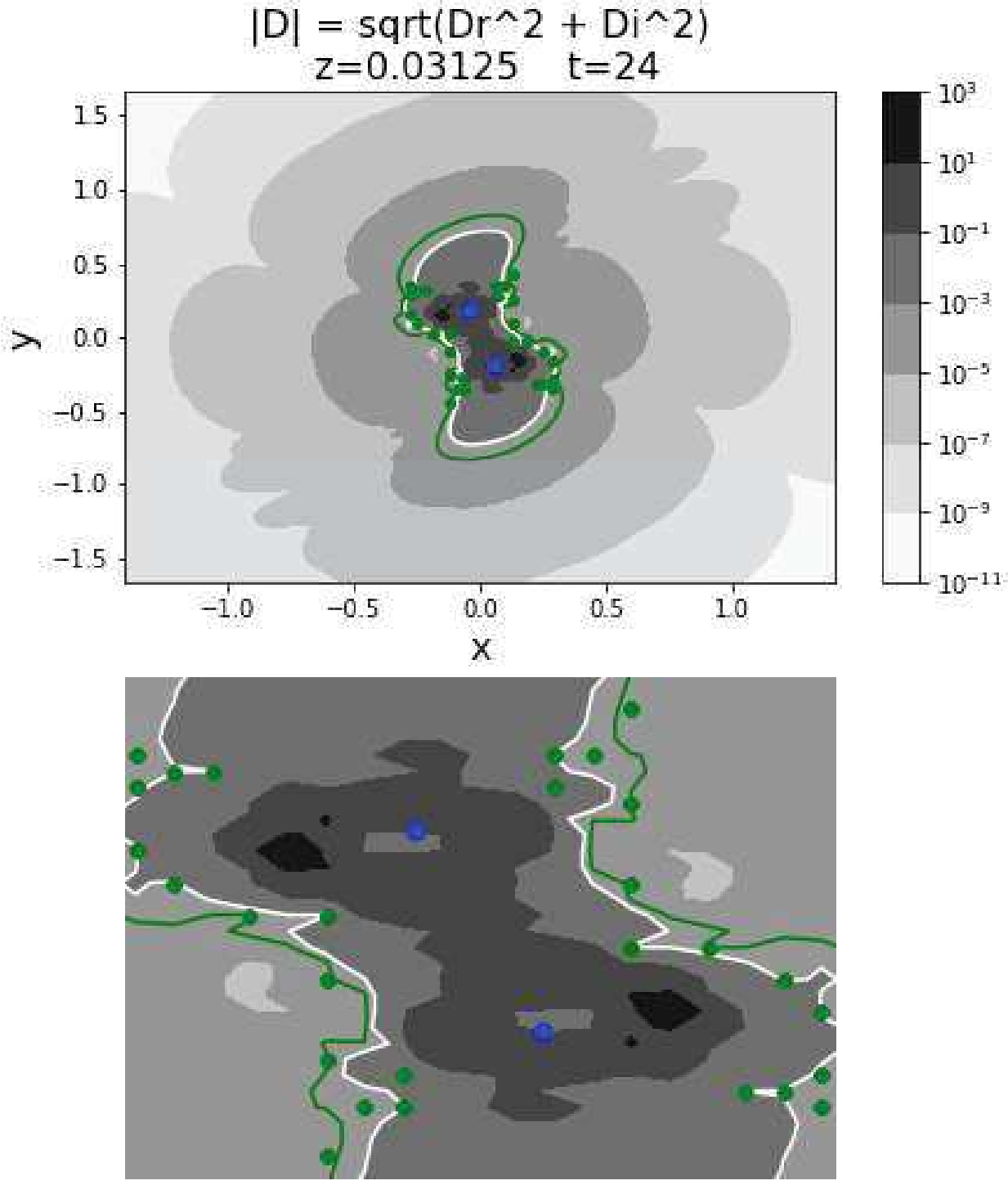

Figures 60-63: Comparing plots of local minima along the x direction from Figures 52-56 with level–0 sets of D_r.

Legend for Figures 60-63:

- Top plot: Plot of the zeros of Dr vs position at the times indicated
- Bottom plot: Plot of the zeros of Dr vs position at the times indicated with magnified resolution
- Deep pink curves: Level 0 sets of D_r
- Green dots: Plots of local minima of |D| taken along sections of constant x (lower left plot). Plots of local minima of |D| taken along sections of constant x restricted to lie between 0.0001 and 0.0012.
- Blue dots: Centroids of MOTSs of initial BHs.

Figure 60: T = 12

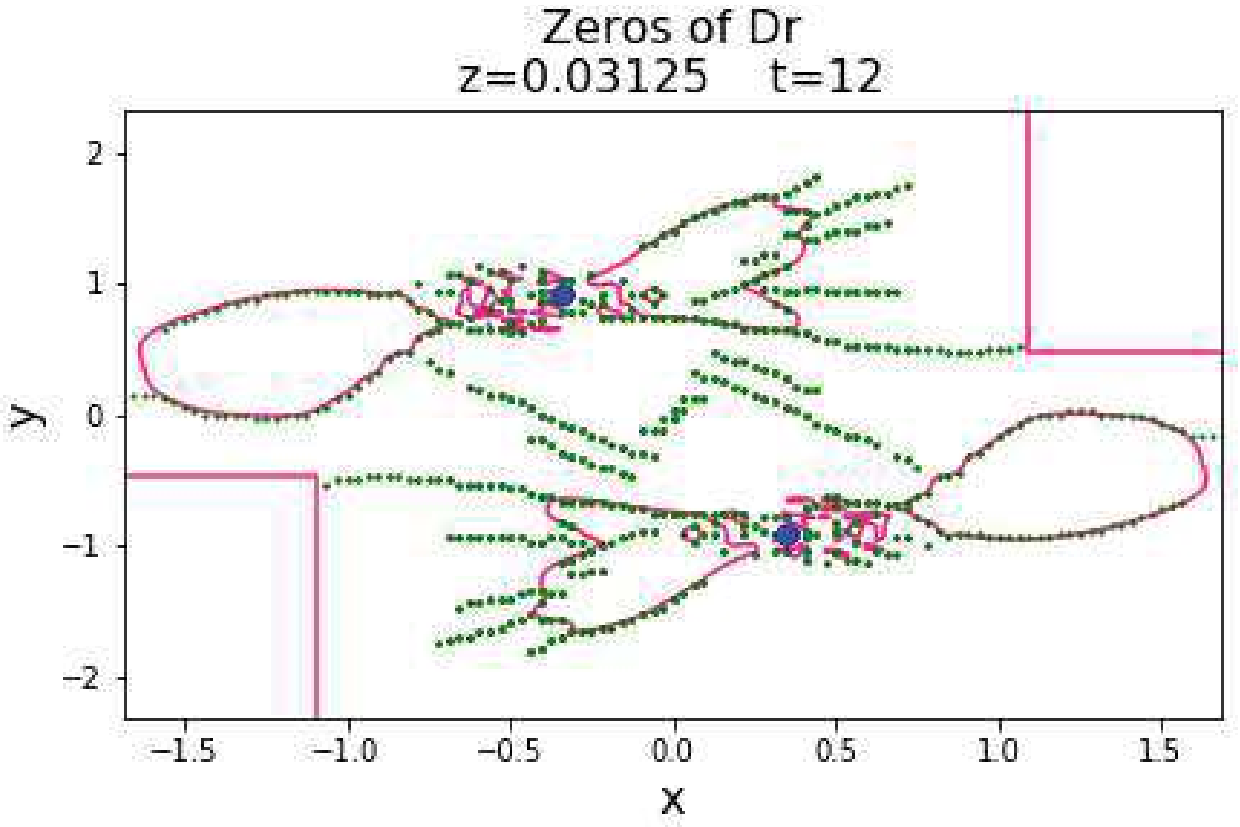

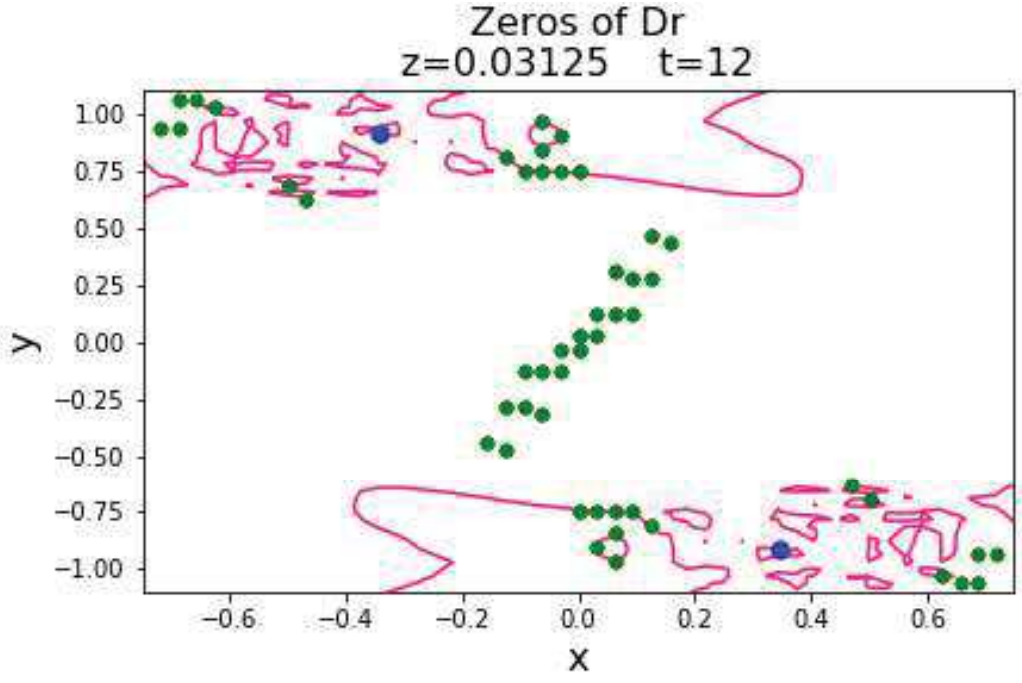

Figure 61: T = 16

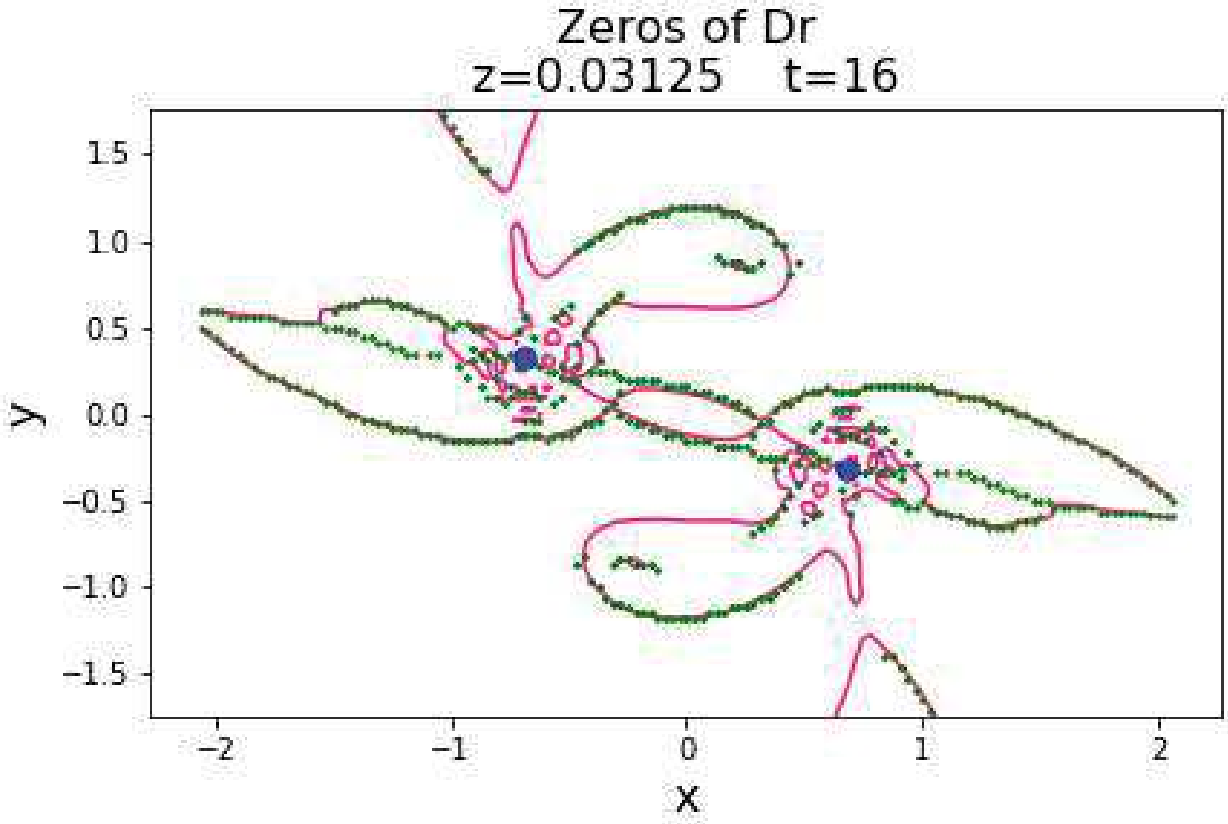

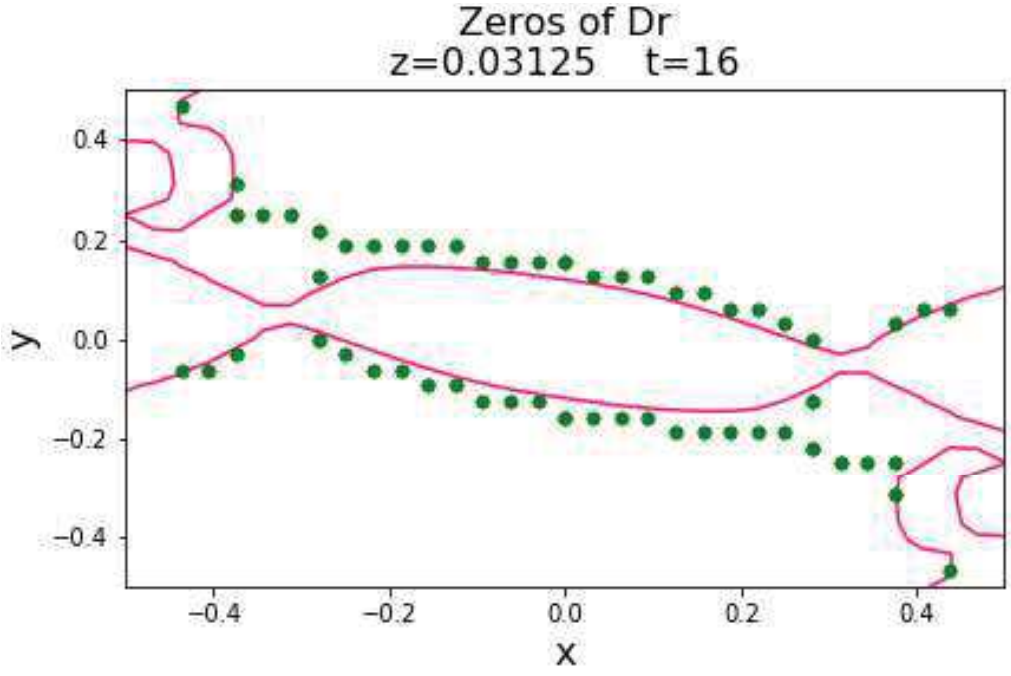

Figure 62: T = 20

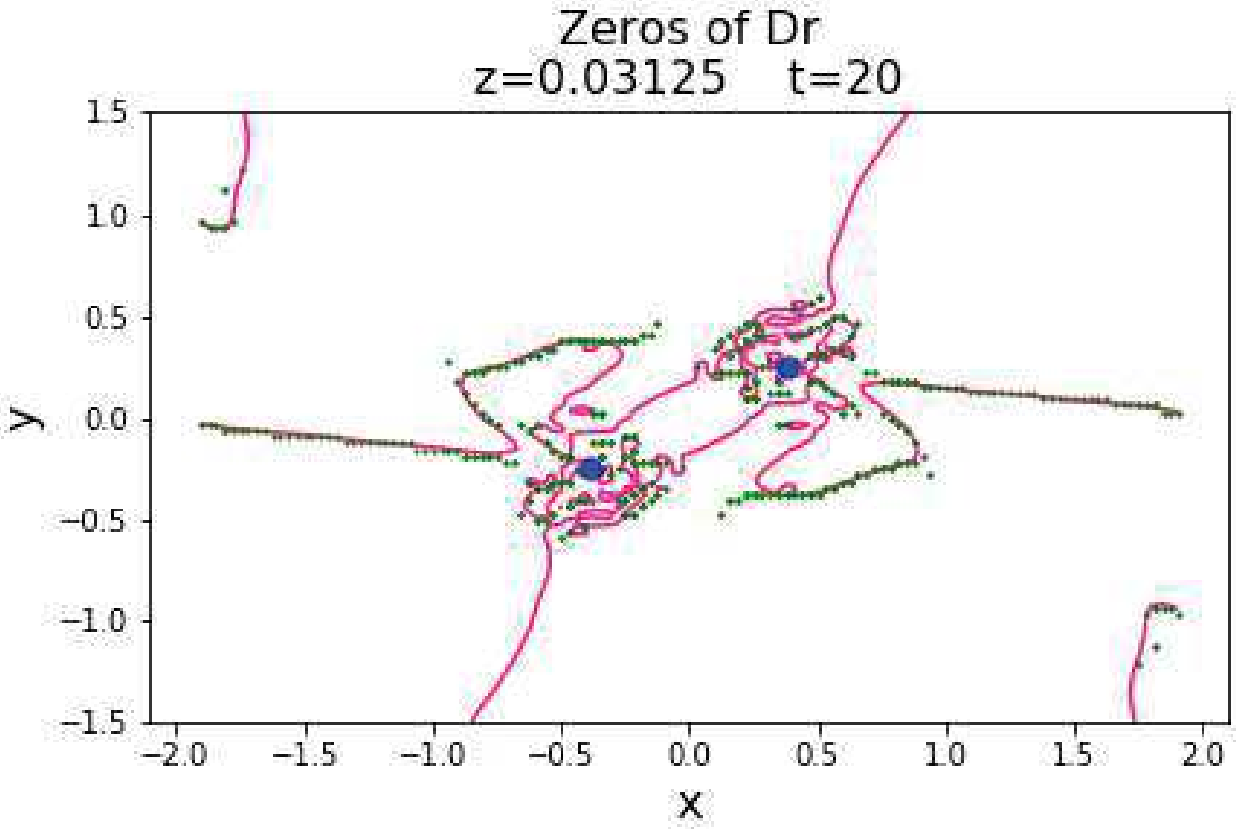

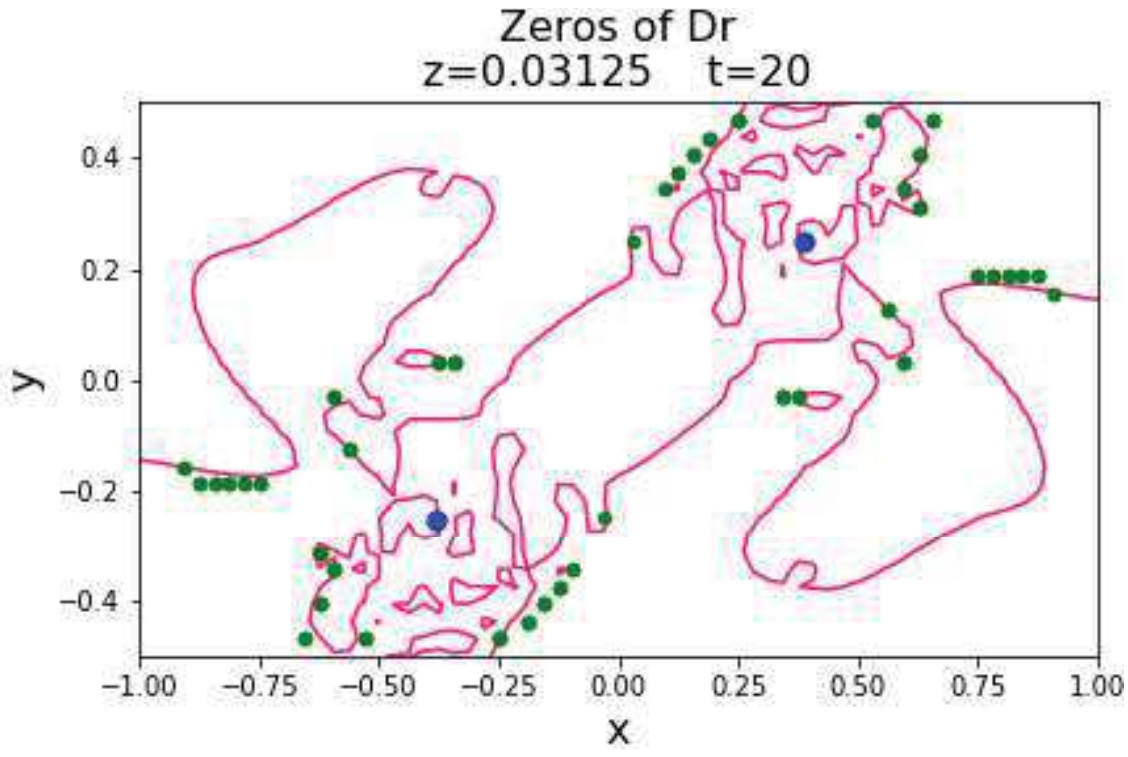

Figure 63: T = 24

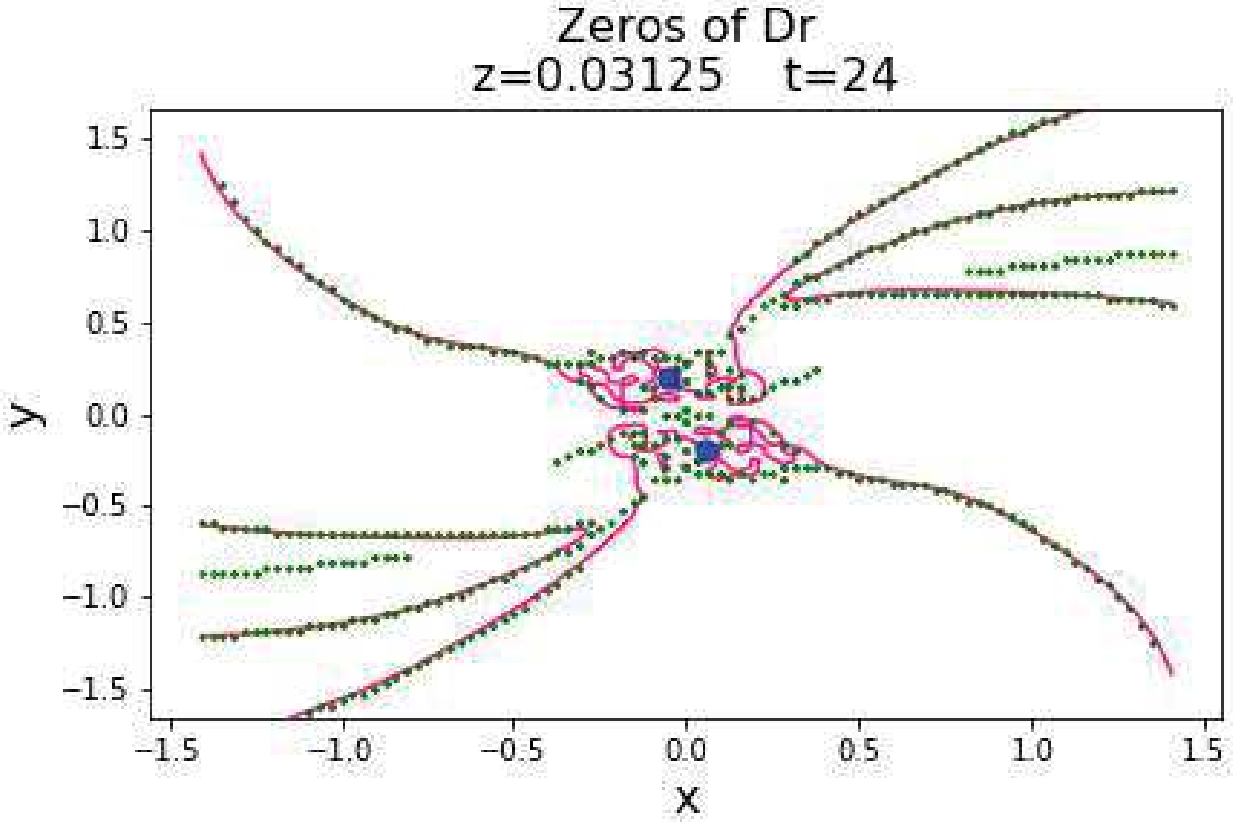

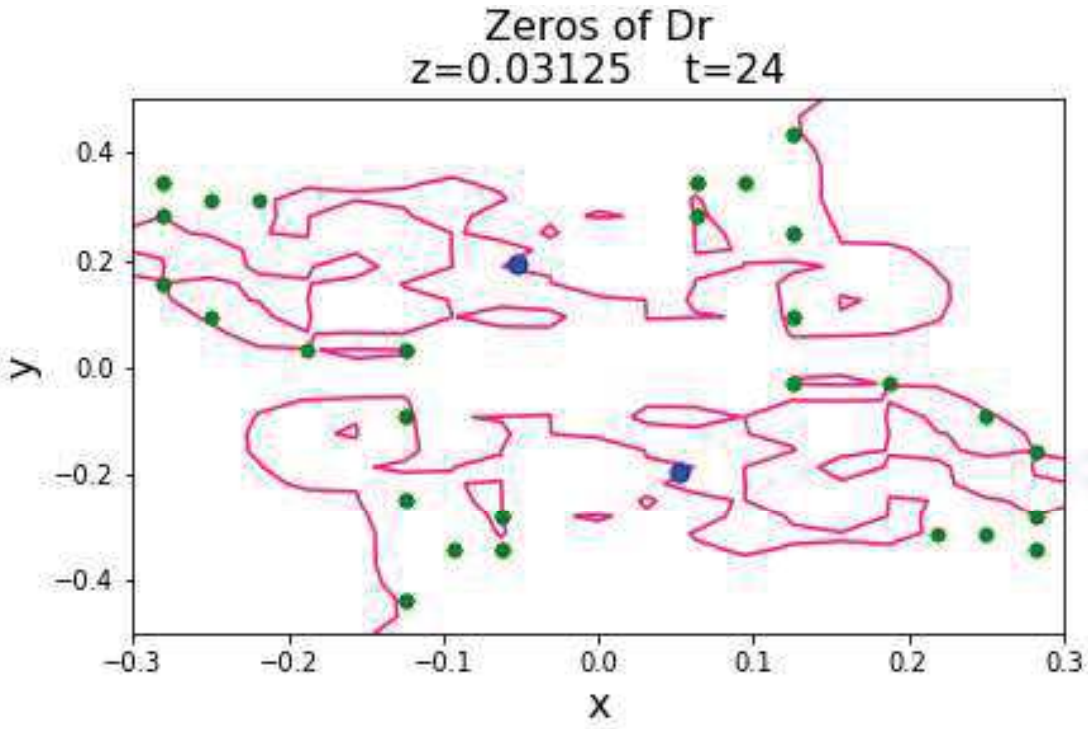

Figures 64-67: Magnified Plots of $\mathrm{Re}\{D^2\}$, $\mathrm{Im}\{D^2\}$, D_r, and D_i for times T = 12, 16, 20, and 24.

Notes:

- $\mathrm{Re}\{D^2\} = D_r{}^2 - D_i{}^2$
- $\mathrm{Im}\{D^2\} = 2{*}D_r{*}D_i$
- The values of D_r, and D_i, $\mathrm{Re}\{D^2\}$, and $\mathrm{Im}\{D^2\}$, have been cut off to lie in the range [-1,1]. See main text for details.

Legend for Figures 64-67:

- Upper left plot: $D_r{}^2 - D_i{}^2$
- Upper right plot: $2{*}\ D_r\ {*}\ D_i$
- Mid left and lower left plot: D_r
- Mid right and lower right plot: D_i
- Saddle brown contours: Level -0.1 sets
- Yellow contours: Level -0.01 sets
- White contours: Level 0.001 sets of |D|
- Lime green contours: Level +0.01 sets
- Cyan contours: Level +0.1 sets
- Blue dots: Centroids of MOTSs of initial BHs

Figure 64: T = 12

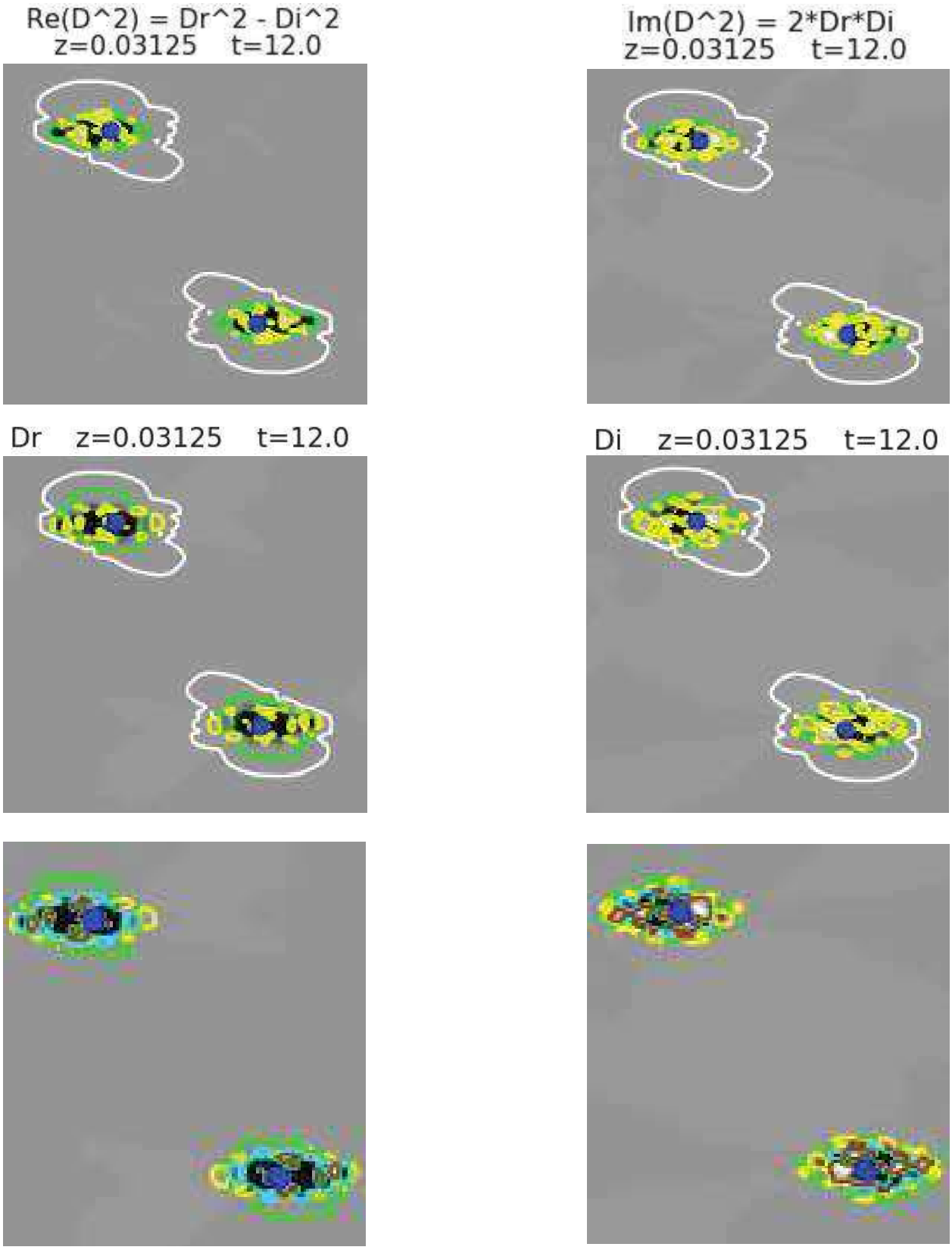

Figure 65: T = 16

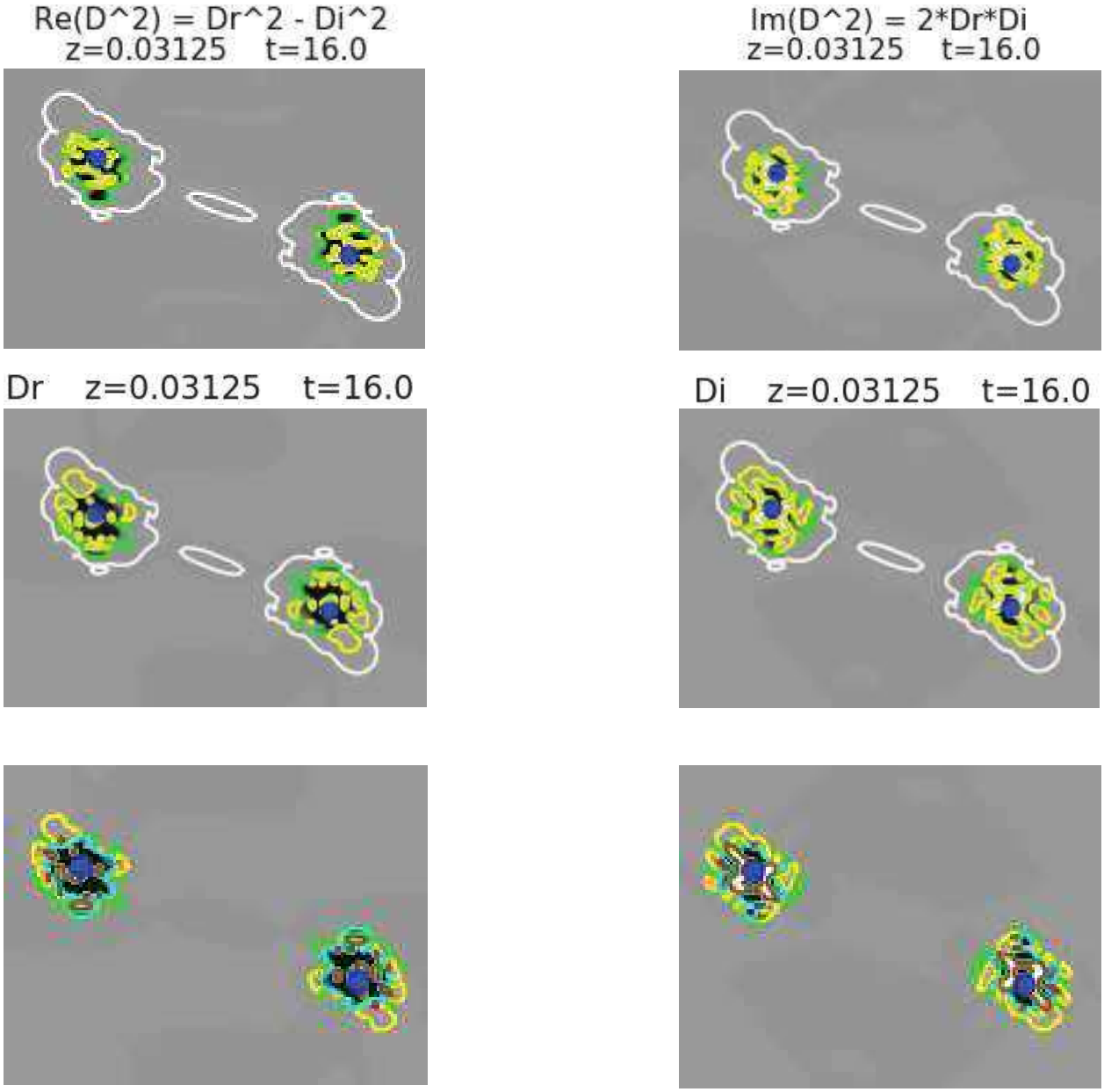

Figure 66, T = 20

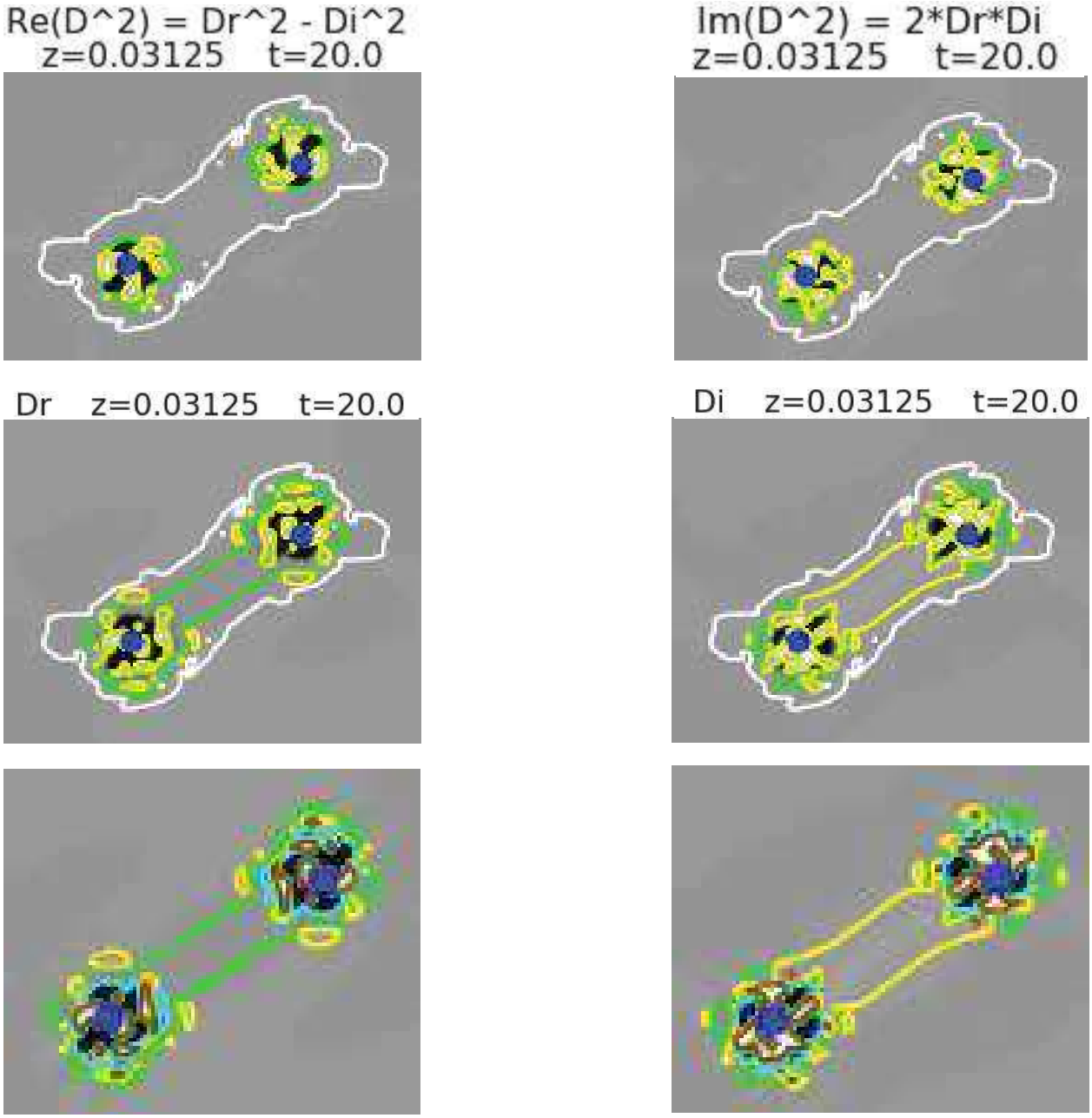

Figure 67, T = 24

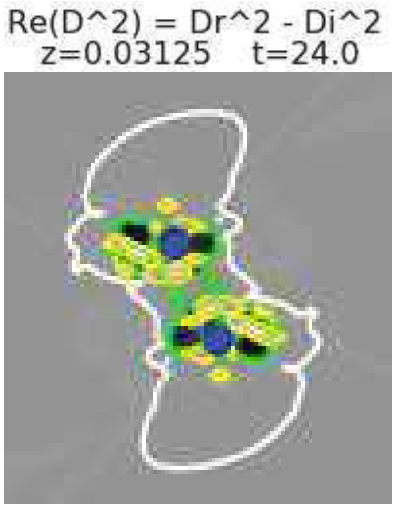

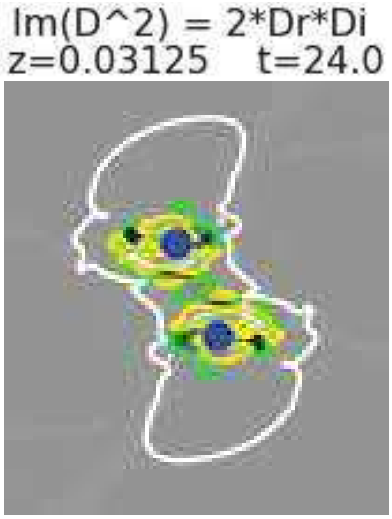

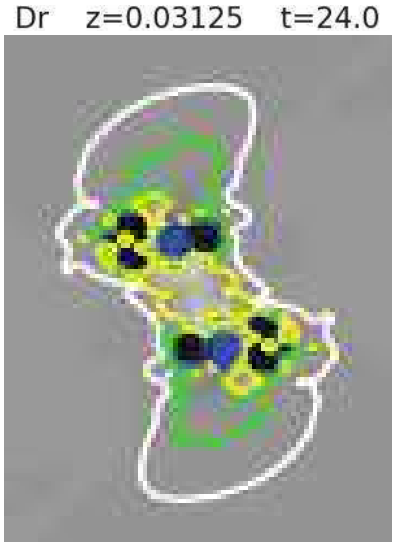

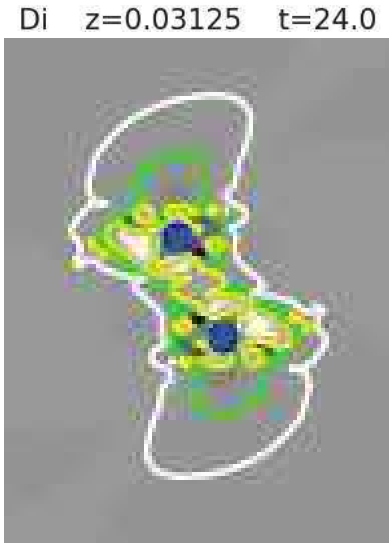

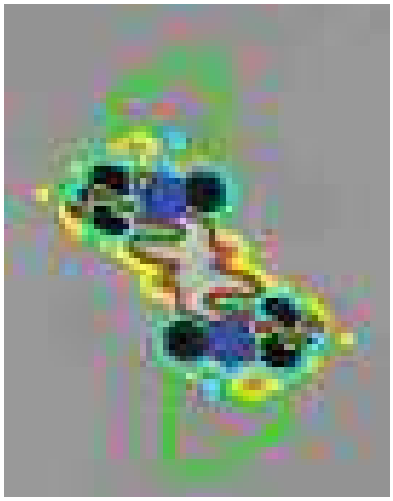

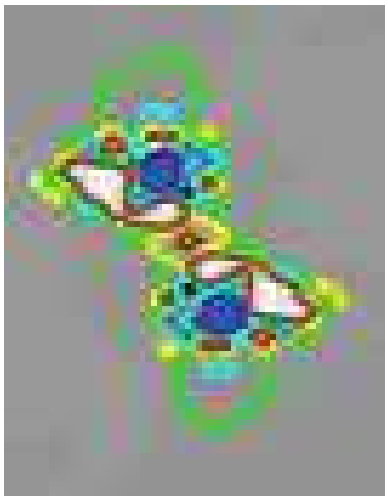

Figure 68: Assessing the validity of approximating the MOTSs of the initial BHs as a spherically symmetric surface and comparing these MOTSs with the white level–0.001 sets of |D|.

Legend:

- Blue circles: “Radius averaged” initial BH MOTSs
- Light Sky Blue circles: points of initial BH MOTSs calculated exactly from spherical coordinates corresponding to $z = 0.03 \pm 0.01$
- Blue dots: centroids of “radius averaged” initial BH MOTSs
- Light Sky Blue dots: centroids of initial BH MOTSs from exact calculation
- White Contours: Level 0.001 sets of |D|.
- Upper left, upper right, lower left and lower right plots: plots of |D| (log scale) at times T = 12, 16, 20, 24, respectively with magnified resolution

Figure 68: Plotting the MOTSs of the initial BHs

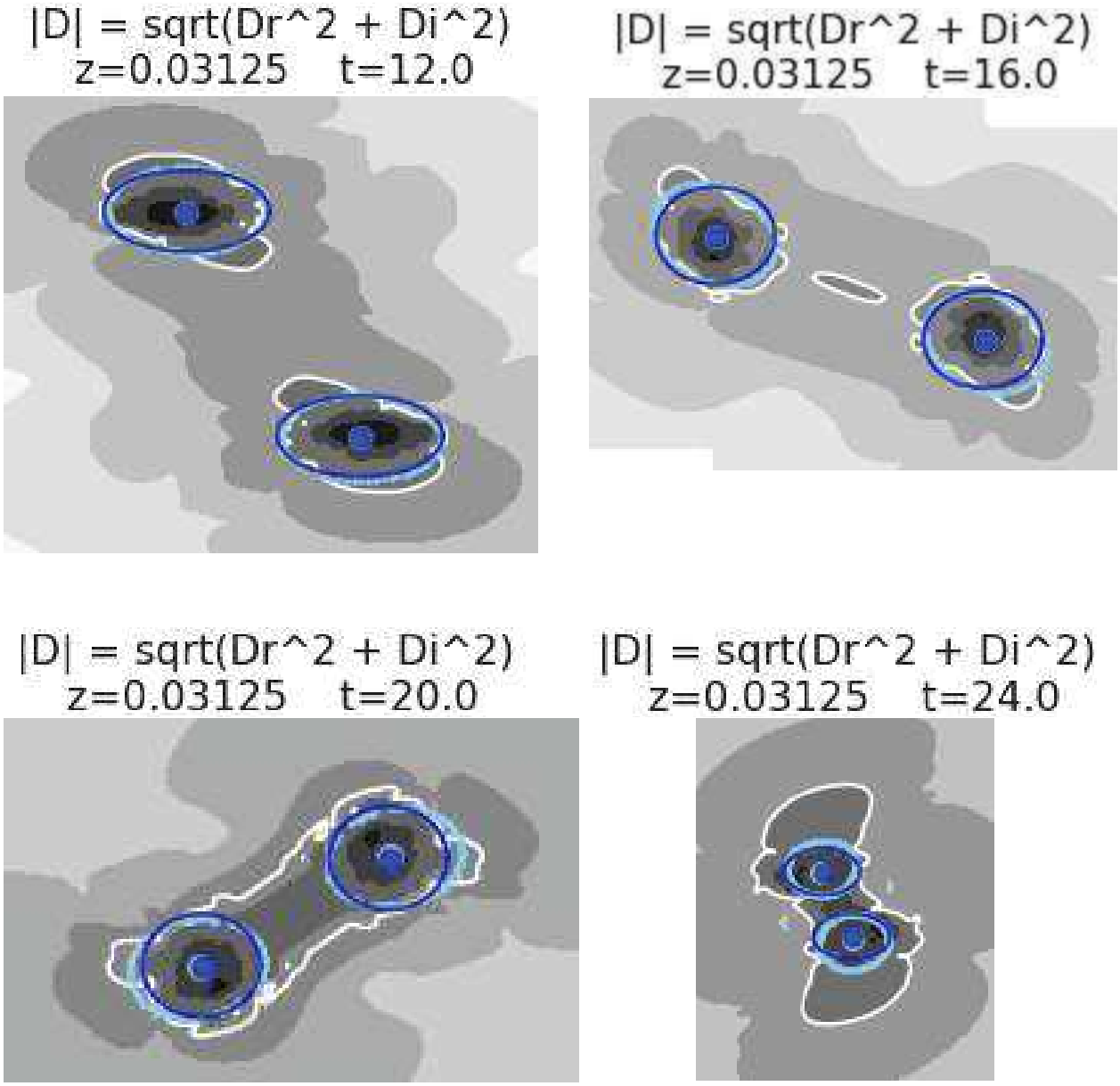

Figures 69-76: Comparing the inner and outer MOTSs, which formed after bifurcation, with the initial two MOTSs of the BHs.

Legend for Figures 69-76:

- Purple dots: points on the inner MOTS (for upper plot) or outer MOTS (for lower plot) calculated exactly. These points correspond to $z = 0.0 \pm 0.1$. The inner or outer MOTS are labelled in the plots.
- Regular Blue circles: "Radius averaged" initial BH MOTSs
- Light Sky Blue circles: points of initial BH MOTSs calculated exactly corresponding to $z = 0.03 \pm 0.01$
- Blue dots: centroids of "radius averaged" initial BH MOTSs
- Light Sky Blue dots: centroids of initial BH MOTSs from exact calculation
- White Contours: Level 0.001 sets of $|D|$
- Upper panel: plot of $|D|$ with superimposed inner MOTS.
- Lower panel: plot of $|D|$ with superimposed outer MOTS.

Figure 69: T = 19

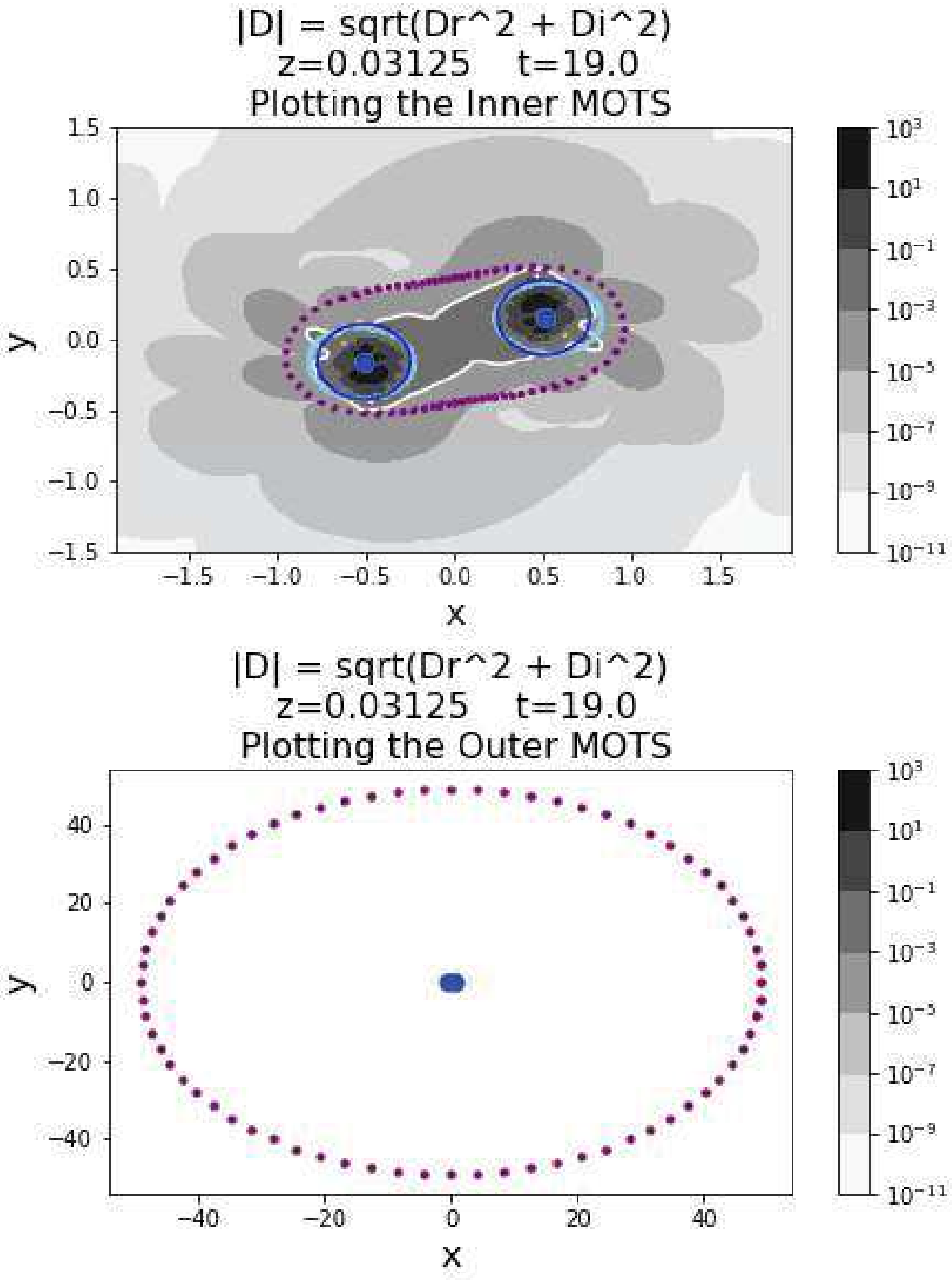

Figure 70: T = 20

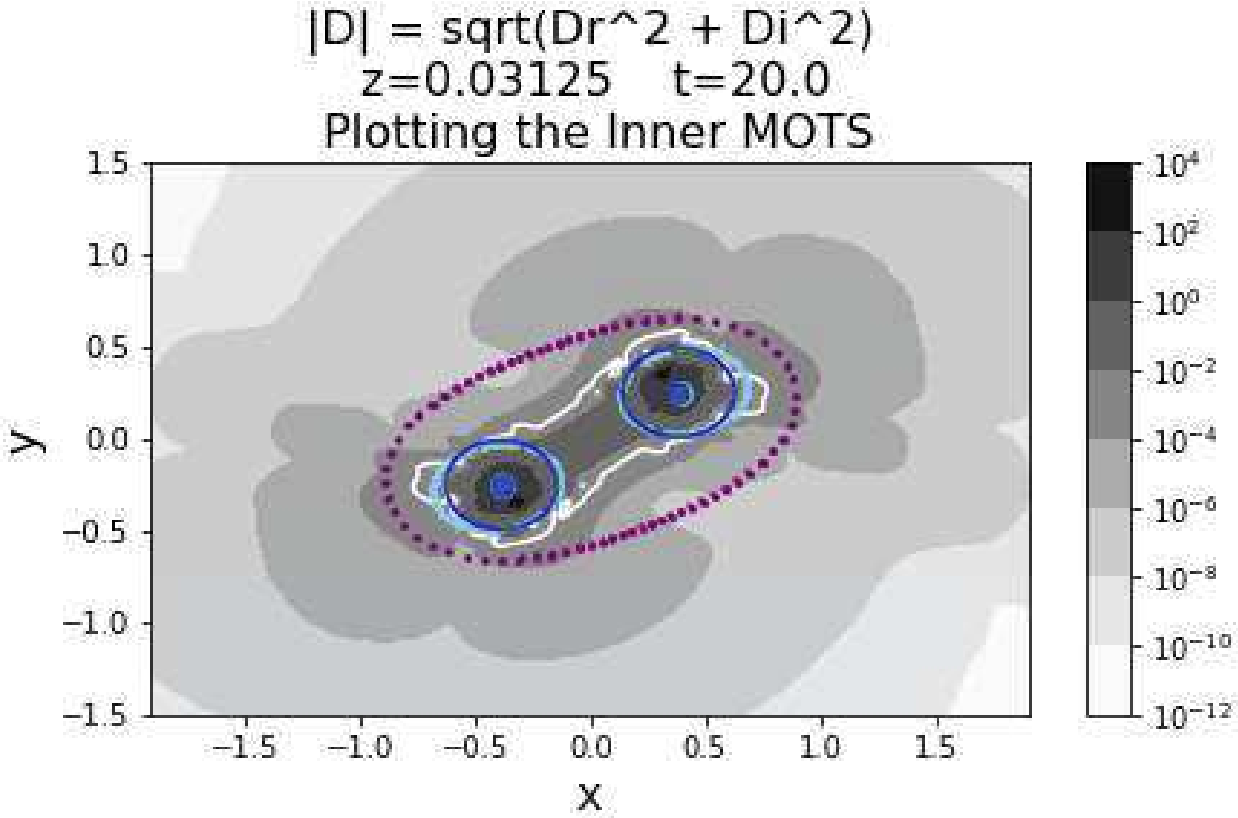

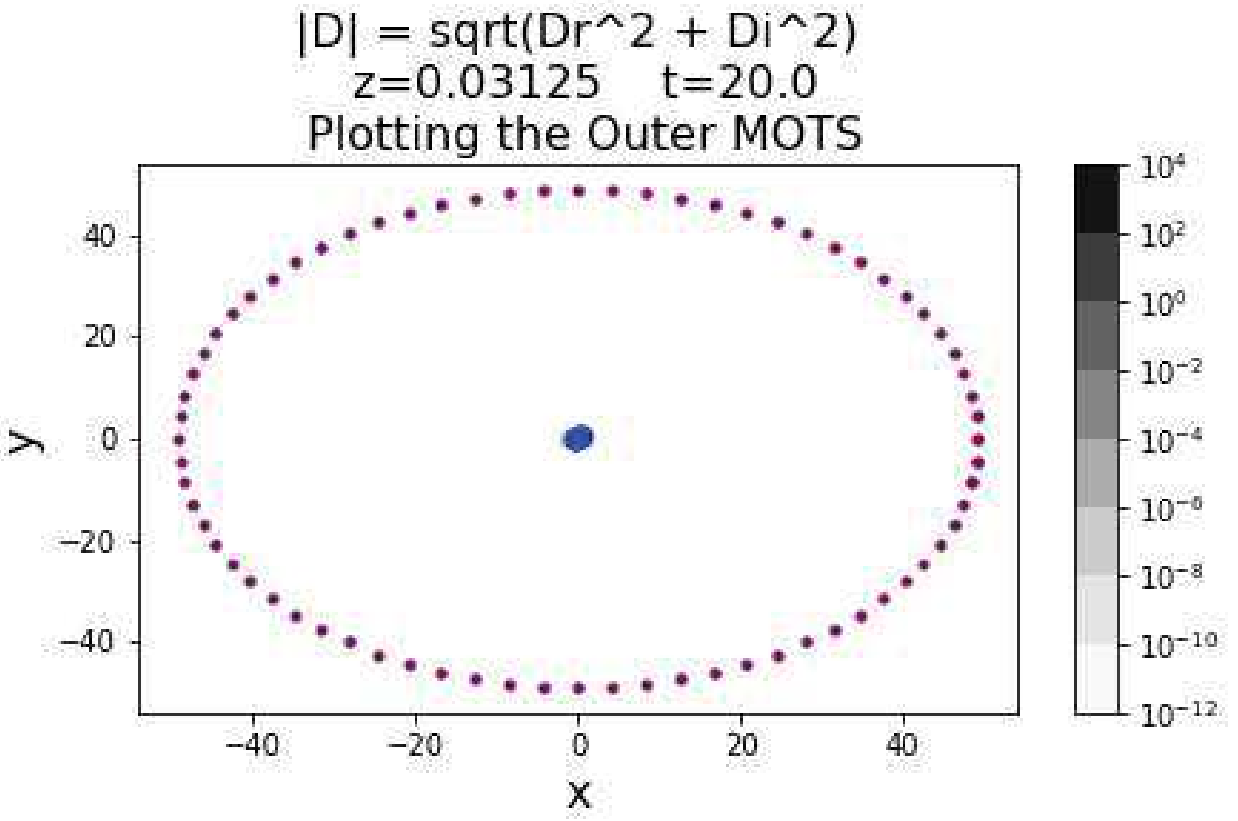

Figure 71: T = 21

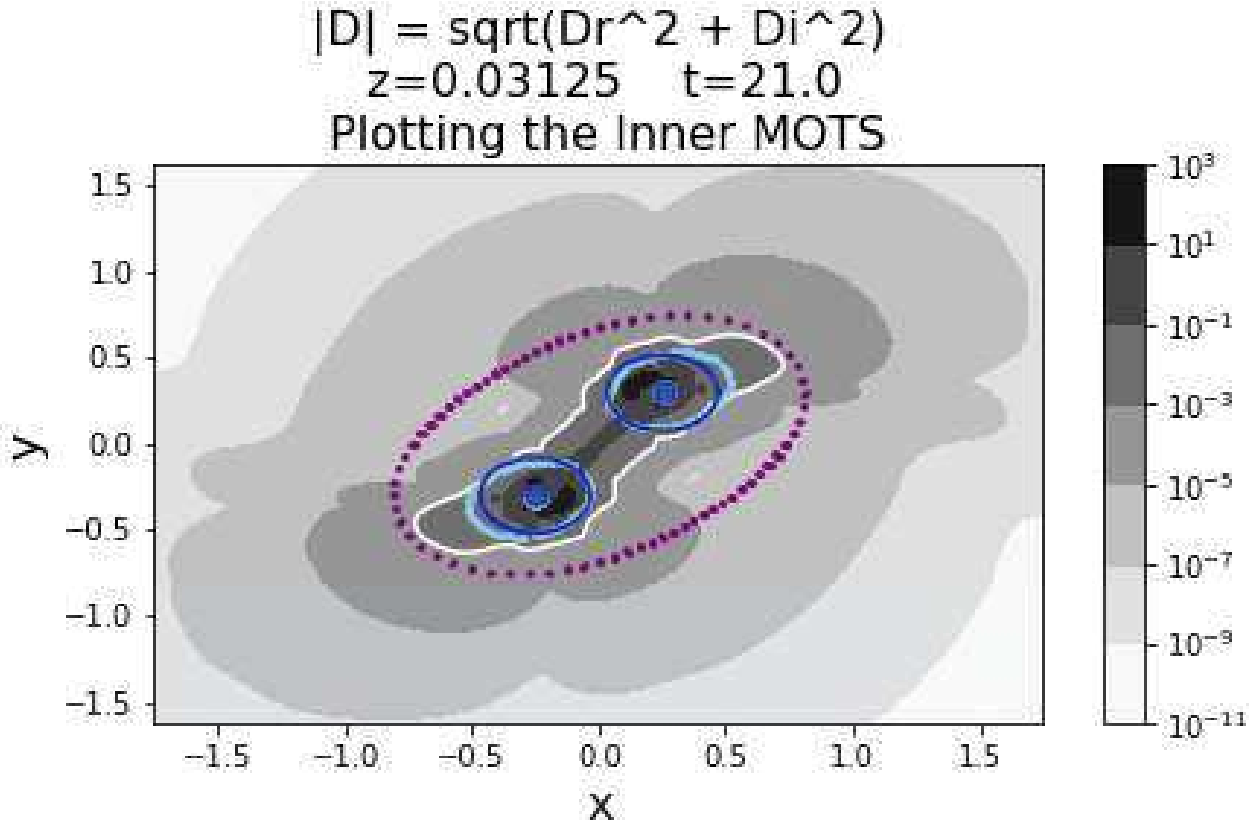

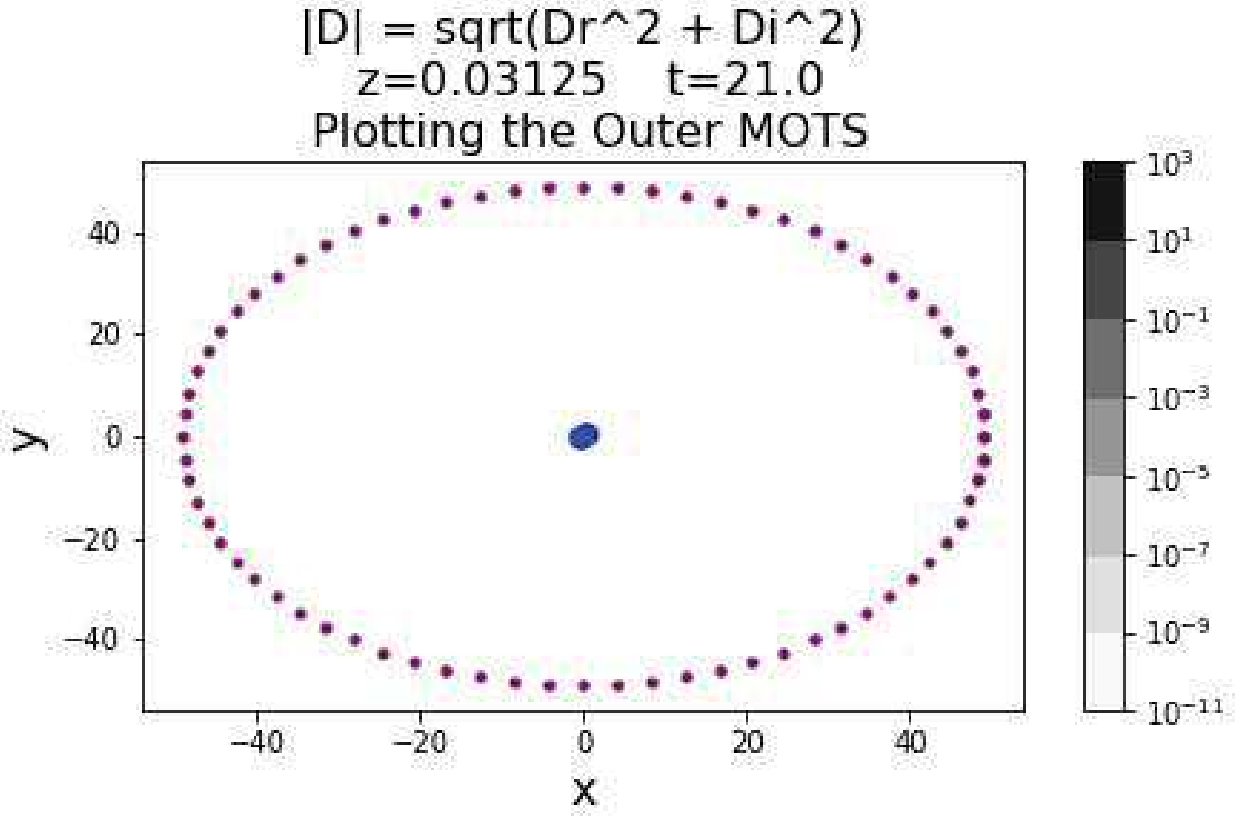

Figure 72: T = 22

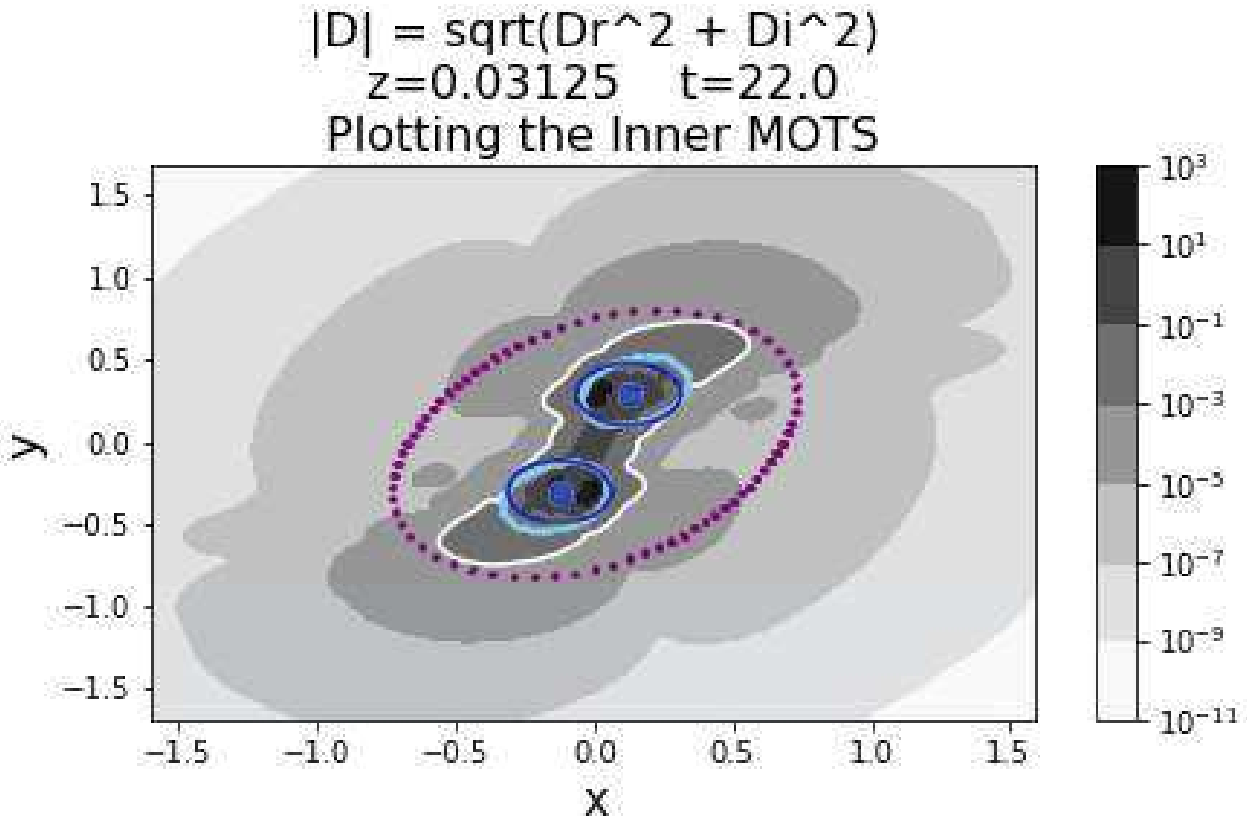

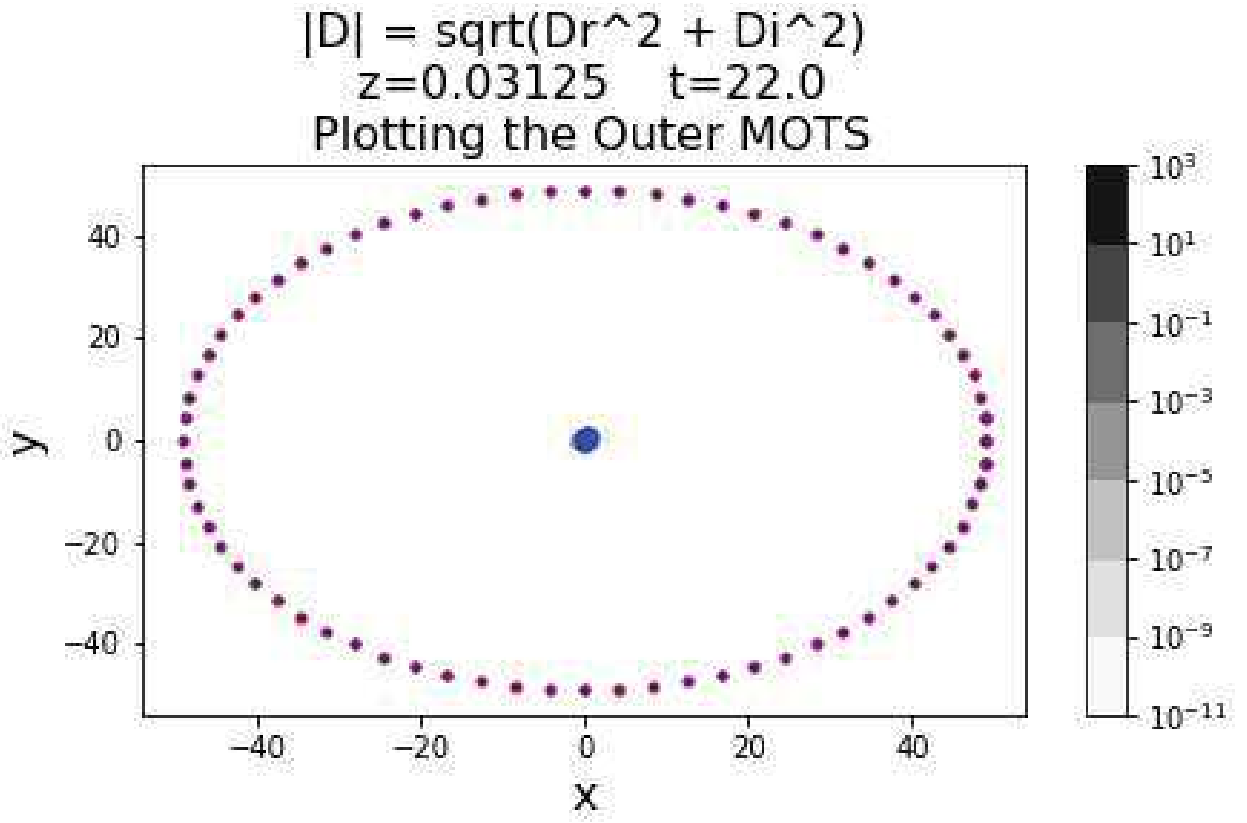

Figure 73: T = 23

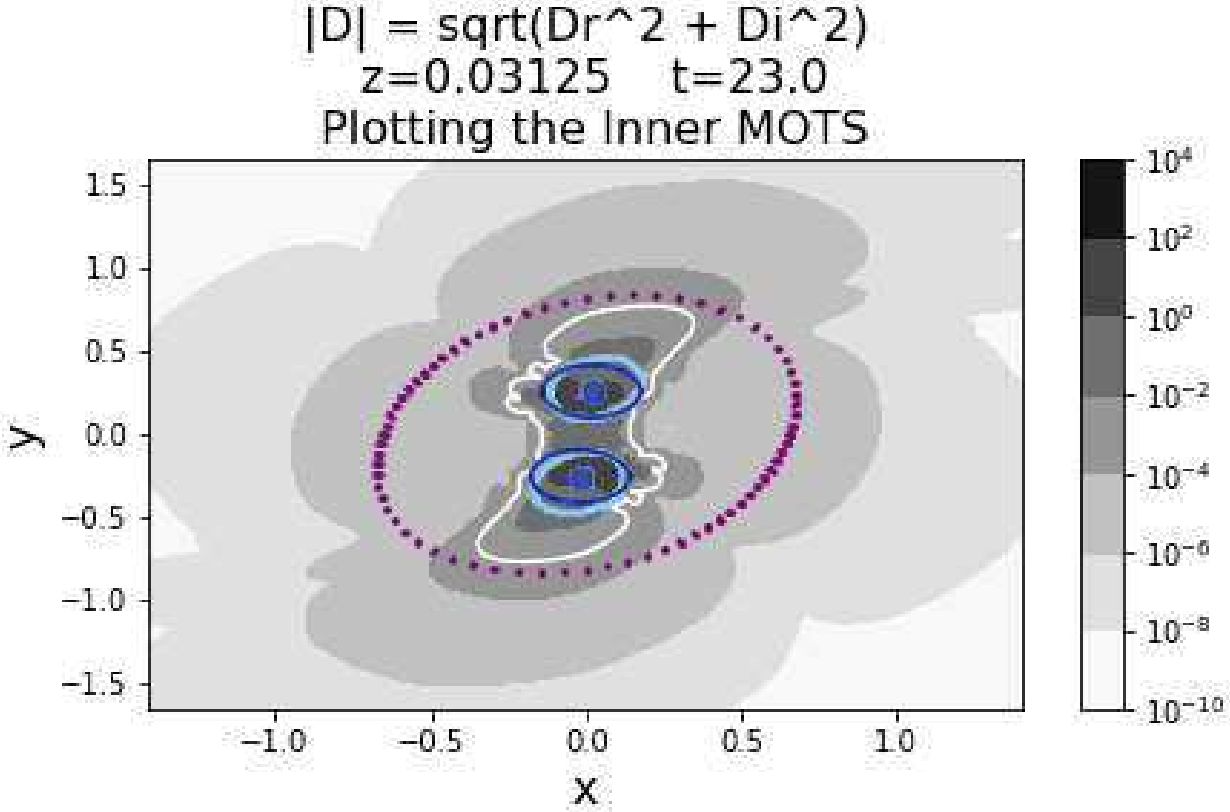

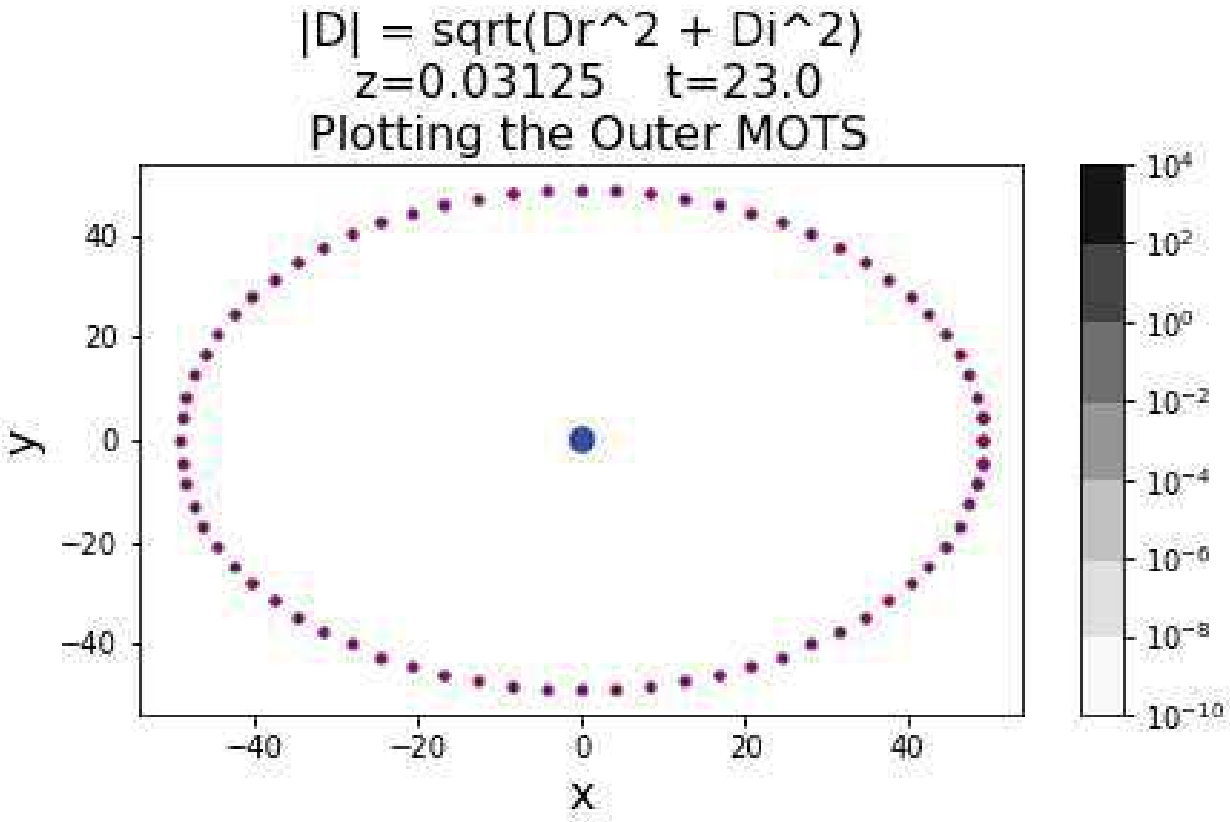

Figure 74: T = 24

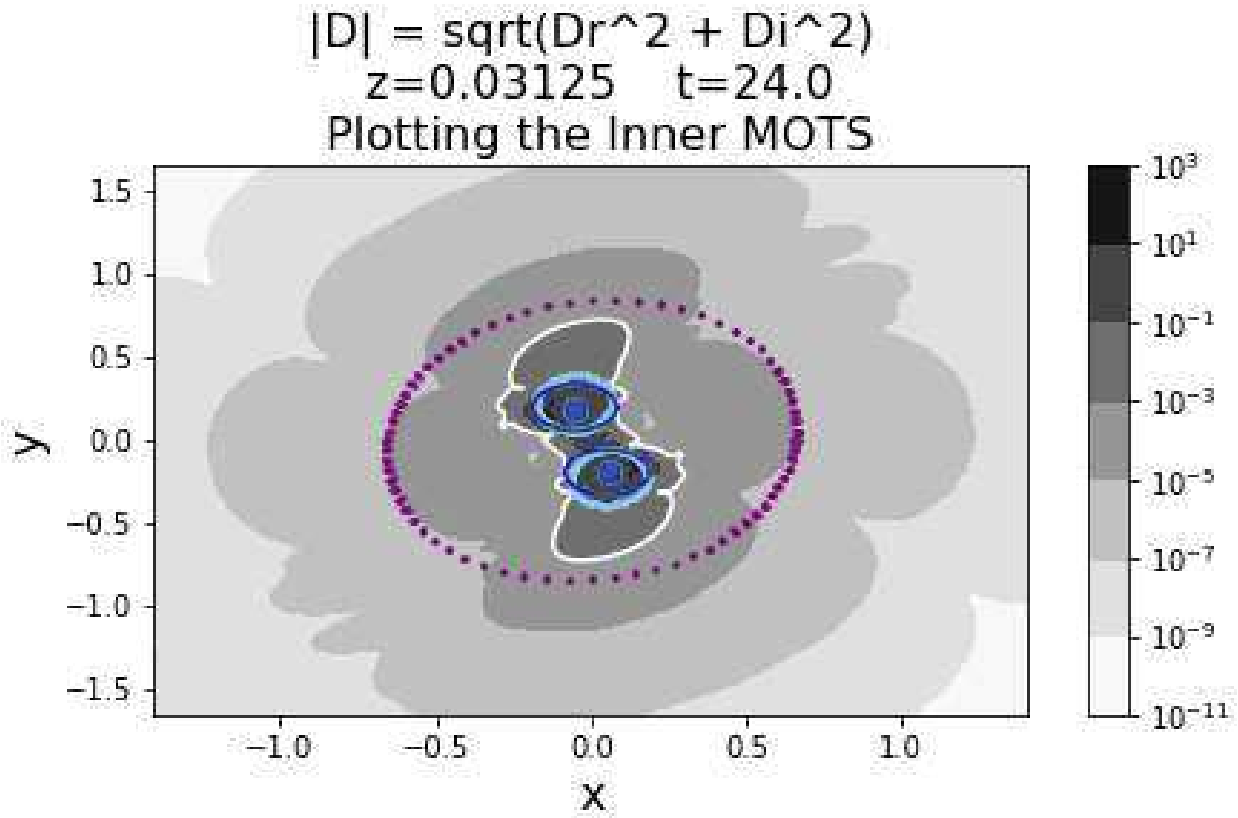

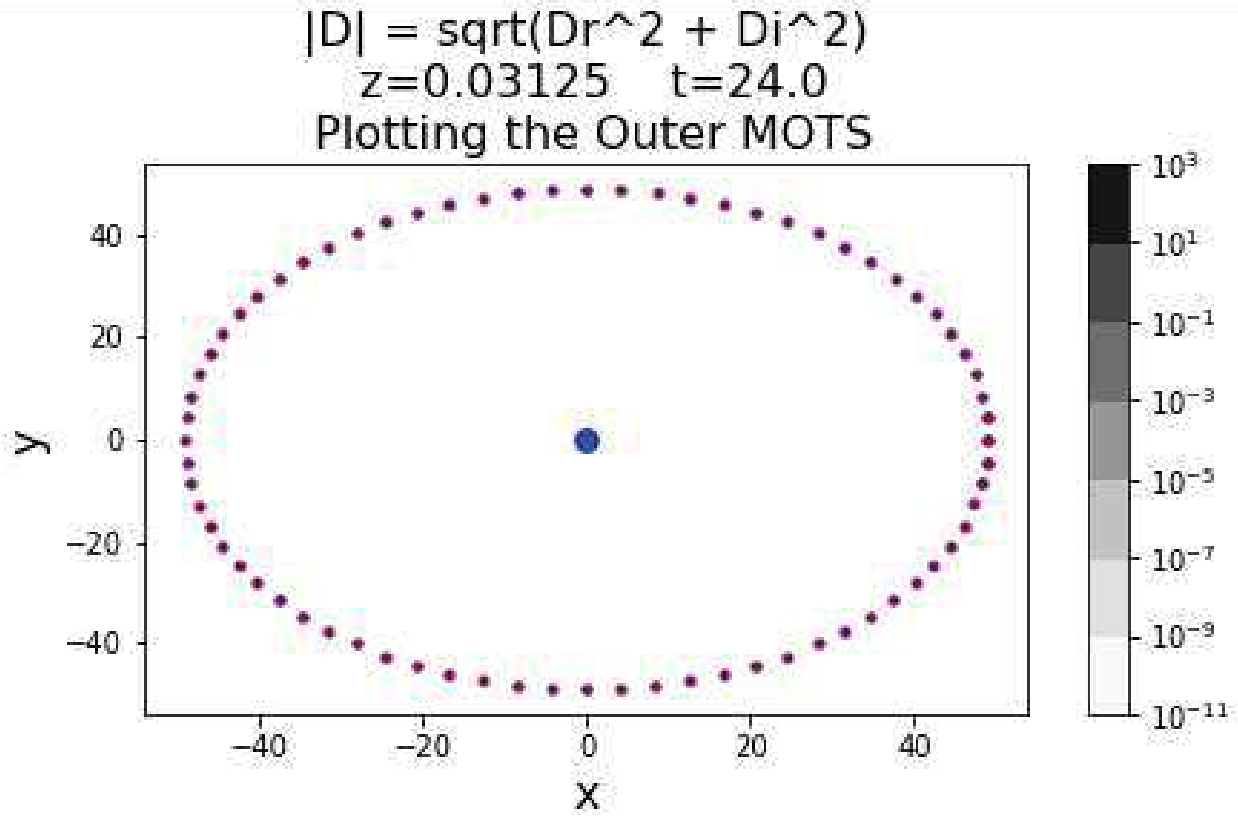

Figure 75: T = 25

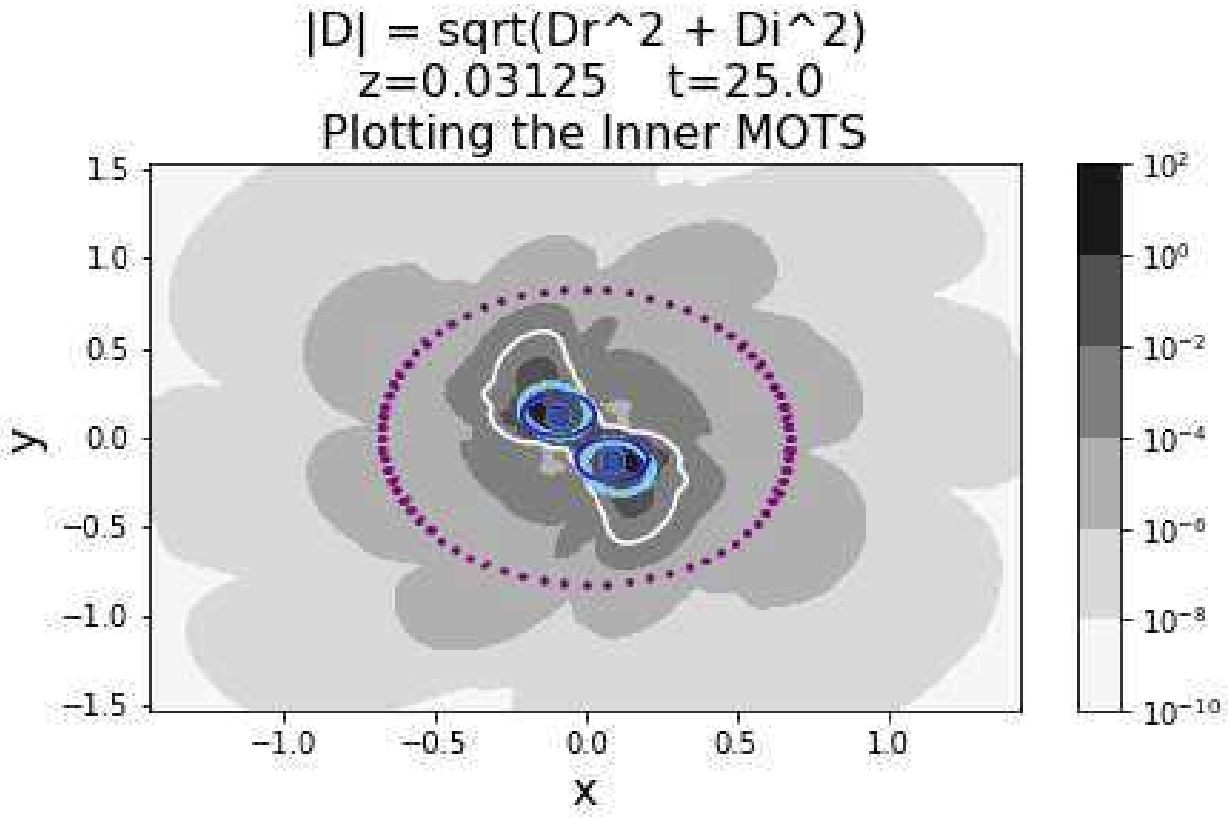

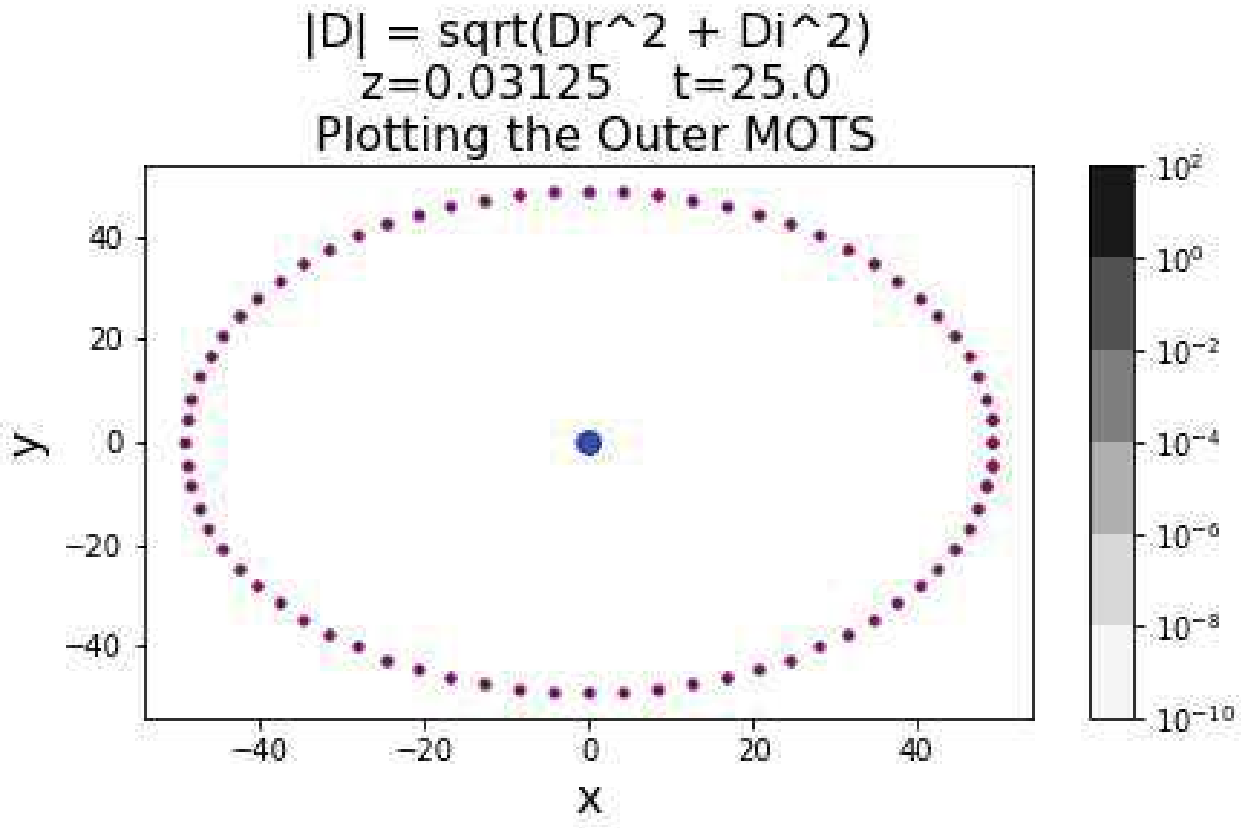

Figure 76: T = 26

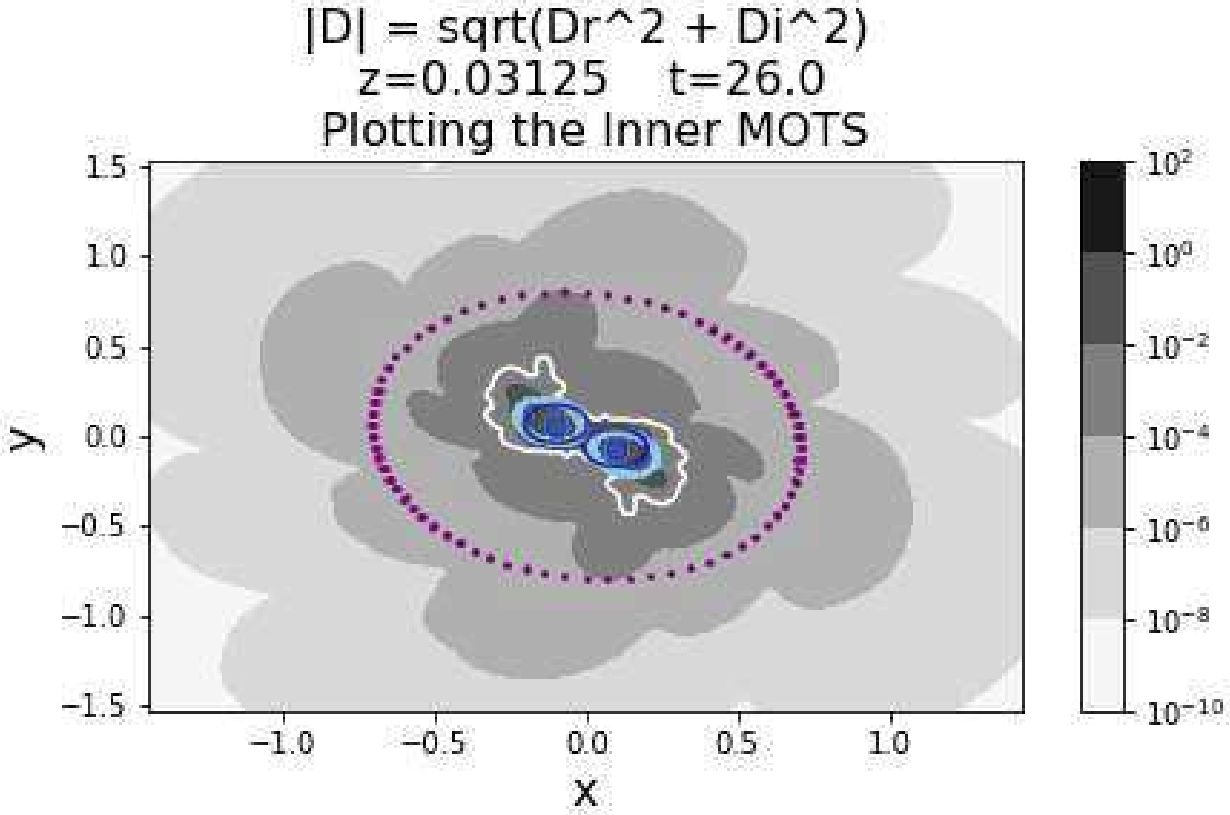

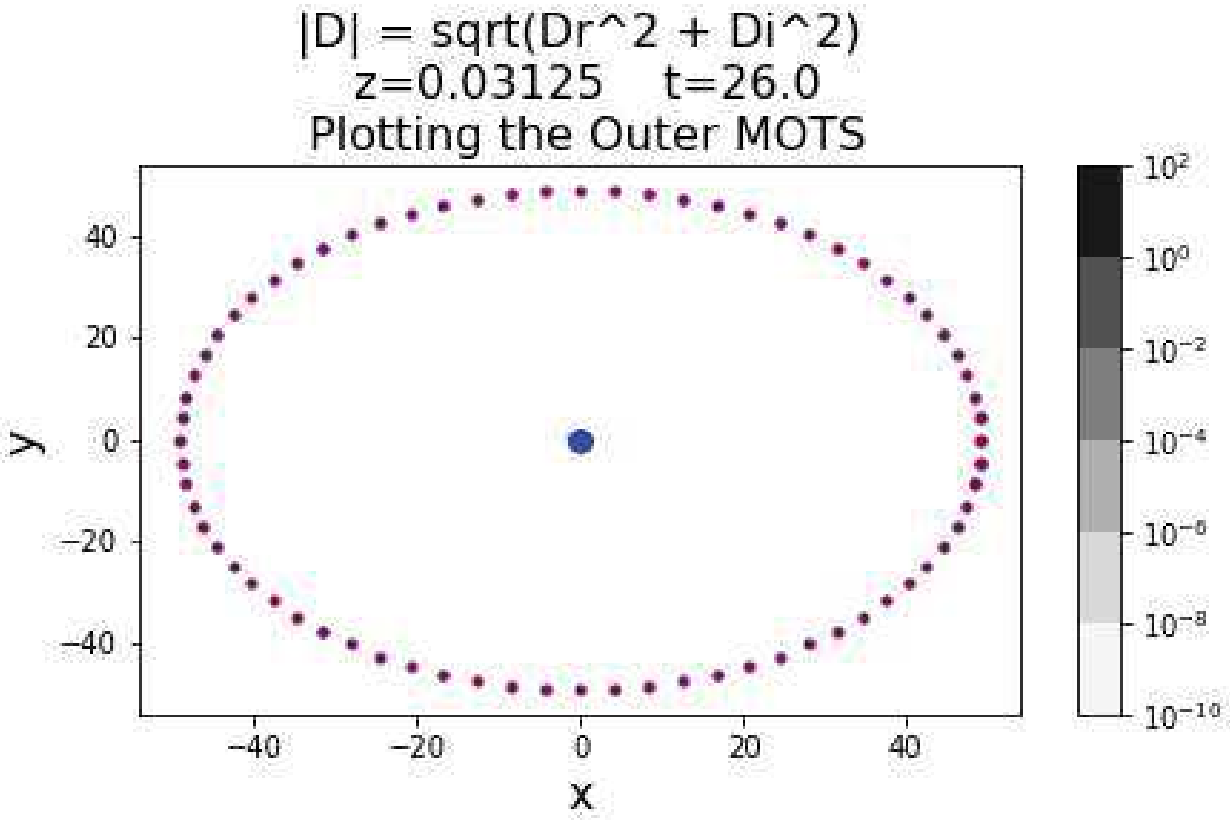

2.4 Discussion

Figures 1–34 plot the time evolution of the quantities $D_r = \mathrm{Re}\{D\}$ (lower left panel), and $D_i = \mathrm{Im}\{D\}$ (lower right panel) with deep pink level–0 sets of the quantities being plotted, and $|D| = \sqrt{D_r^2 + D_i^2}$ in a log and linear scale (upper left and right panel, respectively) with green, red and white level–ε curves of $|D|$ where $\varepsilon = 3 \times 10^{-4},\ 5 \times 10^{-4},\ 1 \times 10^{-3}$, respectively. The blue circles mark the radius averaged MOTSs and the blue dots denote the centroids of the MOTSs, and serve to mark the locations of the BHs through the numerical simulation. The radius averaged MOTSs were computed by forming a sphere centred at the centroid of the MOTS and whose radius was the average distance between the centroid and points on the MOTS. The (x, y) coordinates of this radius averaged MOTS with $z = 0.03125$ were then plotted as the blue circles in the figures. At early times, the level–5×10^{-4} sets of $|D|$ match closely with the radius-averaged MOTSs, as shown in the upper right–hand corners of Figures 1–6. For each $\varepsilon \in \{3 \times 10^{-4},\ 5 \times 10^{-4},\ 1 \times 10^{-3}\}$, at early times (e.g. $T = 0, \ldots, 12$ in Figures 1,...,13, upper left panels), the level–ε sets form pairs of simple closed curves, each of which contains the centroid of the MOTS of each of the two initial BHs. For $T = 13,\ 14,\ 15,\ 16$ (Figures 14–17, upper left panels), the level–ε sets form a third simple closed curve between the centroids of the MOTSs of the two initial BHs, which is centred at $(x, y) = (0, 0)$. The green level–3×10^{-4} sets begin to form their third simple closed curve at times $T = 13$ (Figure 14, upper left) and $T = 14$ (Figure 15, upper left), the red level–5×10^{-4} sets begin to form their third simple closed curve at time $T = 15$ (Figure 16, upper left), and the white level–1×10^{-3} sets begin to form their third simple closed curve at time $T = 16$ (Figure 17, upper left). For each $\varepsilon \in \{3 \times 10^{-4},\ 5 \times 10^{-4},\ 1 \times 10^{-3}\}$, the three simple closed curves of the level–ε sets, once formed, join together to form a single simple closed curve surrounding the centroids of the MOTSs of both BHs. The three green level–3×10^{-4} sets join at time $T = 16$ (Figure 17, upper left), the three red level–5×10^{-4} sets join at time $T = 17$ (Figure 18, upper left), and the three white level–1×10^{-3} sets also join at time $T = 17$ (Figure 18, upper left). After $T = 17$ (Figure 18-27, upper left), for each $\varepsilon \in \{3 \times 10^{-4},\ 5 \times 10^{-4},\ 1 \times 10^{-3}\}$, the level–$\varepsilon$ curves each form a single closed curve surrounding the 2 BHs. It follows that the level–ε curves for each $\varepsilon \in \{3 \times 10^{-4},\ 5 \times 10^{-4},\ 1 \times 10^{-3}\}$ at each T form an invariantly defined, foliation

invariant horizon that contains each separate BH at early times, and contains the merged BH at late times.

The evolution of the level–ε curves through the BBH merger in Figures 1–34 is reminiscent of the sequence of MOTS that take place during the head-on collision simulation in [50, 51]. In particular, in [50, 51] after the two separate initial BHs start to merge together, a third MOTS forms and bifurcates into an inner and outer surface. This bifurcation is also summarized in [31]. In our quasi-circular BBH merger simulations, as shown in Figures 13–21, this bifurcation can be compared to the third simple closed curve that forms as a subset of the level–ε sets of $|D|$ at times $T = 12, \ldots, 20$, where $\varepsilon \in \{3 \times 10^{-4},\ 5 \times 10^{-4},\ 1 \times 10^{-3}\}$. However our numerical studies are not precise enough to study the details of the bifurcation, as found in [31, 50, 51]. At late times (Figures 18-27), it also seems that the centroids of the MOTSs of the initial BHs do not merge, and that in Figures 28-34, the level–ε sets of $|D|$ for $\varepsilon \in \{3 \times 10^{-4},\ 5 \times 10^{-4},\ 1 \times 10^{-3}\}$ may track the MOTS found in [31], which overlap, but do not intersect at late times [31]. However, our simulations did not run to late enough times to make this clear. It was also found in [31], as previously noted, that at late times, provided the initial separation is small enough and the Lapse function is well-enough behaved numerically, the inner MOTS (previously denoted $\mathcal{S}_1$ and $\mathcal{S}_2$) approximated null surfaces, and became isolated horizons. It follows by what we described earlier that the Riemann tensor is algebraically special on $\mathcal{S}_1$ and $\mathcal{S}_2$ [4, 40], so the SPI, $D = I^3 - 27J^2$ vanishes on $\mathcal{S}_1$ and $\mathcal{S}_2$ [22, 55]. Thus, at late times, the level–ε sets of $|D|$ could well approximate these inner MOTS at late times, but more investigation is needed.

The upper left panels in Figures 1–34 provide strong evidence that for $\varepsilon \in \{3 \times 10^{-4},\ 5 \times 10^{-4},\ 1 \times 10^{-3}\}$, the level–$\varepsilon$ sets of $|D|$ track a unique geometric horizon, which can be identified by the level–0 set of the complex SPI, D, as indicated in (1.17). Notice that at early times (e.g., Figures 2 and 3 ($T = 1$ and $T = 2$ respectively)), the deep pink level–0 contours of D_r and D_i extend throughout the plots, indicating that the initial spacetime is locally Kerr at early times. Also at early times, comparing the panels with the plots for $|D|$ with the plots for D_r and D_i (in, e.g., $T = 9$ (Figure 10)), we see that a subset of the deep pink level–0 sets of D_r and level–0 sets of D_i enclose the two initial BHs and align very roughly with the two disjoint

simple closed curves of the level–ε sets of $|D|$ for $\varepsilon \in \{3 \times 10^{-4},\ 5 \times 10^{-4},\ 1 \times 10^{-3}\}$. At intermediate times, say at $T = 17$ (Figure 18), a subset of the deep pink level–0 sets of D_r and level–0 sets of D_i sets align roughly with the third simple closed curve, centered at $(x, y) = (0, 0)$ that forms in the level–ε sets from the log scale plots of $|D|$ (upper left panel). At late times, e.g. T = 25 (Figure 26), a subset of the deep pink level–0 sets for D_r and D_i lie in a region immediately surrounding the pair of BHs, and matches closely with the level–ε sets of $|D|$ for $\varepsilon \in \{3 \times 10^{-4},\ 5 \times 10^{-4},\ 1 \times 10^{-3}\}$ (each of which has formed a single simple closed curve surrounding the two merged BHs at this time). From $T = 20$ (Figure 21, lower left and right panels) through to $T = 42$ (Figure 34, lower left and right panels), the deep pink level–0 sets of D_r and D_i extend throughout the entire plotting region, indicating that at these late times, the final merged BH settles down to a Kerr spacetime, which is of Type **D** everywhere, so the SPI given by $D = I^3 - 27J^2$ vanishes everywhere. More detail on the comparison between the level–ε sets of $|D|$ and the level–0 sets of D_r and D_i will be given in Figures 52–55 and 60-63. Figures 1–34 provide evidence for the fact that the the level–ε sets track the geometric horizons through all stages of the BBH merger, including the time when the level–ε sets of $|D|$ start as disjoint simple closed curves surrounding each of the two separate BHs at early times, when the level–ε sets of $|D|$ are partitioned into three simple closed curves at intermediate times, and when the level–ε sets of $|D|$ form a single simple closed curve around both BHs at late times.

Within numerical accuracy, one could also say that these level–ε sets of $|D|$ do indeed approximate the level–0 sets detected by the SPI, $I^3 - 27J^2$. It remains to estimate the appropriate preferred value for ε. Observe that for
$\varepsilon \in \{3 \times 10^{-4},\ 5 \times 10^{-4},\ 1 \times 10^{-3}\}$, the level–$\varepsilon$ contours are very close to each other, showing that the level–ε sets vary continuously with ε. Observe also that if $\varepsilon_1 \leq \varepsilon_2$, then the 2D area enclosed by the level–ε_1 curve encloses the 2D area enclosed by the level–ε_2 curve, so the whitespace outside the level–ε curves in the upper right figures correspond to regions where locally $|D| < \varepsilon$ $(= 5 \times 10^{-4})$.

The log scale plots of $|D|$ in the upper left–hand panels of Figures 1–34 indicate that $|D|$ decreases on average with average distance from the centroids of the MOTSs. Thus, the plots of $|D|$ do have no global minima. However, Figures 35–63 indicate

that the plots of $|D|$ do have have local minima which approximately coincide with the level–0 sets of D_r and with the level–ε sets for ε between 3×10^{-4} and 1×10^{-3}. Figures 35–39 give 1D slice plots of $|D|$ vs y for selected fixed values of x at time $T = 12$, Figures 40–46 give 1D slice plots of $|D|$ vs y for selected fixed values of x at time $T = 16$ and Figures 47–51 give 1D slice plots of $|D|$ vs y for selected fixed values of x at time $T = 20$. Each of Figures 35–51 correspond to a fixed value of $x = x_0$ along which the slice plots were taken. In the upper panel of each of Figures 35–51, we display the contour plots of $|D|$ vs x and y, which is the same as in the log-scale plots in the upper left–hand corners of Figures 1–34. The green, red and white contours denote level–3×10^{-4}, level–5×10^{-4}, and level–1×10^{-3} sets of $|D|$, respectively and the blue points mark the centroids of the MOTSs. We also plot with green points the location of the local minima of the slice plots of $|D|$. The plots we consider when we compute the local minima are pictured in the lower panels. These plots are plots of $|D|$ when restricted to the domain $x = x_0 =$ constant. These plots are given at various resolutions to highlight the locations of the local minima of $|D|$. It is the value of x_0 that changes with each figure. In each of Figures 35–51, it is noted that many of the local minimum values of $|D|$ lie in the range $[1 \times 10^{-4}, 1.2 \times 10^{-3}]$, which is the range of ε of interest here. It is also noted in Figures 41–43 that the local minima of $|D|$, when considered along the constant x slice plots, happen to be traced out by the green level–3×10^{-4} curves.

In the upper left corner of Figures 52–55, we plot $|D|$ vs x and y with the green, red, and white level–3×10^{-4}, level–5×10^{-4}, and level–1×10^{-3} sets of $|D|$, respectively, along with the blue MOTS centroids as in the log-scale upper left panels of Figures 1–34. We indicate with green points the local minima of $|D|$, when taken along constant $x = x_0$ slice plots ($|D|$ vs y) for all possible values of x_0. Figures 52–55 correspond to times $T = 12,\ 16,\ 20$ and 24, respectively. The upper right plots in Figures 52–55 are also of $|D|$, with the same features as in the log scale plot in Figures 1–34 except, here, the green points indicate the local minima of $|D|$, when taken along constant $y = y_0$ slice plots ($|D|$ vs x) for all possible values of y_0. Comparing the upper left and upper right plots in Figures 52–55, we see that $|D|$ attains a local minimum value along the constant $x = x_0$ slice plots roughly when $|D|$ attains a local minimum value along constant $y = y_0$ slice plots. Thus, the local minima of $|D|$ along the constant

$x = x_0$ slice plots give a good indication of the true local minima of $|D|$. In the bottom panel of Figures 52–55, D_r is plotted, as in the lower left panel of plots in Figures 1–34, and its zeros are given by the deep pink contours.

At $T = 16$, in Figure 53, the local minima of $|D|$ trace the green level–3×10^{-4} sets in the region where the red level–5×10^{-4} and white level–1×10^{-3} sets form a simple closed curve around the origin. In Figures 56–59, we compare the local minima of $|D|$ along constant x slice plots with the green and white level–3×10^{-4} and level–1×10^{-3} sets of $|D|$, respectively. We observe that at time $T = 12$ and time $T = 16$, these local minima appear to track the green level–3×10^{-4} sets, while at later times, these local minima appear to track more closely the white level–1×10^{-3} sets. The top panel of each figure gives the plot of $|D|$ vs x and y in the original resolution, and the bottom panel gives a magnified resolution plot of $|D|$ for clarity.

In Figures 60–63, we compare the locations of the local minima of $|D|$ along with the level–0 sets of D_r at times $T = 12,\ 16,\ 20$, and 24, respectively. The blue centroids of the MOTSs are plotted for clarity. It is noted that the local minima of $|D|$ track very closely the level–0 sets of D_r at all times $T = 12,\ 16,\ 20,\ 24$. This indicates that D_r provides a dominant contribution to the quantity, $|D| = \sqrt{D_r^2 + D_i^2}$. The bottom panel provides a magnified resolution of the top panel, which plots the level–0 set of D_r along with the local minima of $|D|$. Because the local minima of $|D|$ track closely the level–0 sets of D_r and also the level–ε sets of $|D|$ for $\varepsilon = 3 \times 10^{-4}$ and $\varepsilon = 1 \times 10^{-3}$, it follows by transitivity that the level–0 sets of D_r closely approximate the level–ε sets of $|D|$ for both $\varepsilon = 3 \times 10^{-4},\ 1 \times 10^{-3}$.

The problem of finding level–0 sets of the complex D cannot be clearly resolved by analyzing $|D|$ because, as previously noted, $|D|$ is a positive definite quantity, and the discrete resolution imposed by the numerical simulation does not allow one to accurately find level–0 sets of $|D|$. Thus, to gain further insight into the geometric horizon through the BBH merger, it is therefore helpful to analyze quantities which change sign through a zero (e.g. D_r and D_i as described above). In each of Figures 64–67, we plot magnified views of the quantities $\mathrm{Re}\{D^2\} = D_r^2 - Di^2$ and $\mathrm{Im}\{D^2\} = 2 * D_r * D_i$ in the upper left panel and upper right panel, respectively, along with D_r in the middle and lower left panel and D_i in the middle and lower right panel. Figures 64–67 correspond to times $T = 12,\ 16,\ 20$ and 24, respectively. The white contours

in the upper and middle left and right panels are level–1×10^{-3} sets of $|D|$, as was also displayed in Figures 1–34. In each of the six panels, the yellow and green contours contours give the level–-0.01 and level–$+0.01$ sets of the quantities in question being plotted, respectively. In the lower left and lower right panels of each figure, we plot for clarity the level–-0.1 and level–$+0.1$ sets of the relevant quantites being plotted, respectively. By continuity, we know that a level–$+0.01$ and a level–-0.01 set straddle a level–0 set. However, the level–± 0.01 sets show that the corresponding nearby level–0 set legitimately corresponds to a level–0 set of the complex quantity, D. In all figures (at times $T = 12,\ 16,\ 20,\ 24$), the level–± 0.01 sets for D_r or D_i are contained within the interior(s) of the white level–1×10^{-3} sets. At times $T = 12$ and $T = 20$, the level–± 0.01 sets of D_r and D_i form two distinct regions, each of which surrounds each of the two initial BHs. At time $T = 20$, the green level–$+0.01$ set of D_r extends to form a simple closed curve around both BHs, which is contained within the white yellow $|D| = 1 \times 10^{-3}$ curve, while the yellow level–-0.01 set of D_i extends to form a simple closed curve around both BHs, inside the white level–1×10^{-3} sets of $|D|$. This indicates that the magnitude of $|D|$ is considerably higher than 0.01 inside the white level–0.001 sets of $|D|$, which demonstrates the uniqueness of the level–1×10^{-3} curves of $|D|$. At $T = 24$ the union of the level–± 0.01 curves of D_r and D_i form one "connected component" which surrounds both BHs. Since the yellow level–-0.01 sets of D_r (resp. D_i) are closely intertwined with the green level–$+0.01$ sets of D_r (resp D_i), there must be a surface surrounding the level–± 0.01 sets of D_r (resp D_i) through which D_r (resp. D_i) changes sign. These surfaces for D_r and D_i must exist near the white level–1×10^{-3} sets (or D_r and/or D_i could likely change sign on the white level–1×10^{-3} sets). Similarly, at times $T = 12,\ 16,\ 20,\ 24$, the white level–1×10^{-3} contour(s) also encloses the level–± 0.01 sets for the quantities $2 * D_r * D_i$ and $D_r^2 - D_i^2$. Thus, there must be a surface across which the quantity $2 * D_r * D_i$ (or $D_r^2 - D_i^2$) changes sign, which also occurs near the region where the white level–1×10^{-3} sets of $|D|$. Thus, Figures 64–67 verify that the level–zero set of the complex invariant D is best approximated by the level–1×10^{-3} sets of $|D|$.

In Figures 1–34 in the upper right–hand panel, we plot the value of $|D|$ and compared its level–5×10^{-4} sets with the radius averaged MOTSs. In computing the radius averaged MOTSs, we made use of the average radius of the MOTS. In Figure

68, we compare the radius averaged initial BH MOTS (plotted in blue) with points from the "actual" initial BH MOTS (plotted in a "thick" light sky blue line for clarity) whose z coordinate value was in the range $[0.02,\ 0.04]$. The upper left, upper right, lower left and lower right panels of Figure 68 are plots of the two different calculations for the AHs for times $T = 12,\ 16,\ 20$ and 24, respectively. It is clear from Figure 68 that the actual initial BH MOTS is a nearly spherical surface, so approximating the MOTS with its average radius is a reasonable approximation, particularly for illustration.

As previously noted in [50, 51, 31] and summarized here, the initial BH MOTSs are AHs at early times but between the times $T = 18$ and $T = 19$, a third surface forms and bifurcates into an inner and outer MOTS. It is the outer MOTS that forms the AH of the merger. In Figures 69–76, we plot, as before, the white level–1×10^{-3} set of $|D|$, the radius averaged and exact initial BH MOTS (plotted in regular blue and light sky blue) but here, we superimpose with purple dots the points on the exact inner (resp. outer) MOTSs whose corresponding z value lies in the range $[-0.1, 0.1]$. We find that shortly after the bifurcation (e.g. $T = 19, 20, 21$), the inner MOTS is not unreasonably approximated by the white level–1×10^{-3} (although this white level curve tracks more closely the initial BH MOTSs). The outer MOTS (which is the new AH) has an average radius which is roughly 50 times larger than the scale of the previous plots (i.e. the inner MOTS, the initial BH MOTS) and the various contours of $|D|$, D_r and D_i. Thus, from Figures 68–76, the white level–1×10^{-3} contours of $|D|$ well approximate the initial BH MOTSs at all times, but these initial BH MOTSs are only AHs before the bifurcation (i.e. $T = 18$ and before in the figures).

Note that in the bottom panels of Figures 69-76, the outermost MOTS (the AH) may appear to be ellipsoidal. However, this is simply an artifact of the appearance of the x and y scales. The horizontal and vertical range of this outermost MOTS are both roughly $[-40, 40]$, so the horizontal and vertical scales are actually quite similar to each other.

Therefore, Figures 1–76 provide strong evidence that one can define a unique smooth geometric horizon, given by the level–0 set of the complex invariant $D = I^3 - 27J^2$, which we have found is best approximated in the numerics by the level–1×10^{-3} sets of $|D|$.

Chapter 3

Conclusion

We have studied the algebraic properties of the Weyl tensor by plotting the real part, imaginary part, and magnitude of the complex scalar polynomial invariant $D = I^3 - 27J^2$ as it evolves through the quasi-circular orbit of two equal mass BHs, as presented in Figures 1–34. In the plots of the magnitude of D, $|D| = \sqrt{\mathrm{Re}\{D\}^2 + \mathrm{Im}\{D\}^2}$ in Figures 1–34, we marked the locations of the two initial BHs by tracking the centre and average radius of the MOTSs of the initial BHs. In plotting the MOTSs, we approximated the MOTS as a spherical surface. This turns out to be a valid approximation, as shown in Figure 68. On these plots, we also superimposed the level–3×10^{-4} sets in green, the level–5×10^{-4} sets in red, and the level–1×10^{-3} sets in white. We found that at early times, each such level set is partitioned into two disjoint simple closed curves, each of which contains one of the two centroids of the MOTSs of the 2 separate initial BHs. Then each level set, at some intermediate time, forms a third simple closed curve which is centred at the origin and positioned between the centroids of the MOTSs of the two initial BHs. This third simple closed curve expands in area as time increases, and eventually, the three simple closed curves partitioning the given level set merge and form one simple closed curve which contains the centroids of both initial BHs.

The plots for $|D|$ in Figures 1–34 provide strong evidence that the level sets of $|D|$ identify the geometric horizon. However, it is impossible to identify the level–0 sets of $|D|$ precisely, since $|D|$ is a sum of positive definite terms, so numerical errors and discrete resolution cause $|D|$ to be strictly positive. Thus, to further study the zeros of $|D|$, which would indicate the zeros of the complex quantity D, we found the local minima of $|D|$. In Figures 35–51, we obtained 1D "slice plots" of $|D|$ vs y for a fixed x coordinate value at selected times $T = 12,\ 16,\ 20$, and 24. We plotted the positions of the local minima of $|D|$ along these slice plots being considered in the upper panel of each of Figures 35–51. We then found and plotted the local minima

of $|D|$ along all slice plots obtained from Figures 35–51 and plotted the positions of these local minima with green points on the plots of $|D|$ vs x and y in the upper left panels of Figures 52–55. We repeated this procedure and located the local minima of $|D|$ as functions of x with fixed y coordinate. These local minimum positions from all slice plots with fixed y are plotted with green points on the plots of $|D|$ vs x and y in the upper right panels of Figures 52–55. By comparing the locations of the respective local minima of $|D|$, we saw that the locations of the local minima of $|D|$ along all constant x slice plots well approximate the locations of the overall local minima of $|D|$. We also noticed that the positions of the local minima of $|D|$ correspond closely to zeros of D_r, which are plotted in the lower panels of Figures 52–55. Figures 56–59 showed that a subset of the local minima whose corresponding $|D|$ values lie in the range $[1 \times 10^{-4},\ 1.2 \times 10^{-3}]$ track closely (or are traced by) the level–3×10^{-4} sets of $|D|$ at early times the level–1×10^{-3} sets of $|D|$ at late times. Figures 60–63 indicate that the local minima of $|D|$ also coincide very closely with the level–0 sets of D_r. Thus, the level sets of $|D|$ are well approximated by the local minima of $|D|$ and correspond closely to a subset of the level–0 sets of D_r.

Since $|D|$ is positive definite, its zeros cannot be traced by positive and negative level sets. Therefore, we have also analyzed quantities which change sign through a zero. We plotted $D_r = \mathrm{Re}(D)$ and $D_i = \mathrm{Im}(D)$ in Figures 1–34, with their respective level–0 contours in deep pink. We found that a subset of the level–0 sets of D_r and D_i approximates the level–ε sets of $|D|$ for each $\varepsilon \in \{3 \times 10^{-4},\ 5 \times 10^{-4},\ 1 \times 10^{-3}\}$ especially upon examination of the simple closed curves of the level–ε sets of $|D|$ centred at the origin, which forms at times $T = 13,\ 14,\ 15,\ 16$ in Figures 14–17, respectively. This provides more evidence that the given level–ε contours identify the sought after geometric horizon.

We examined the contours of D_r and D_i, and also of $2 * D_r * D_i$ and $D_r^2 - D_i^2$, more closely in Figures 64–67. We examined where the quantities being plotted are positive or negative by superimposing the level–$+0.01$ sets in green and level–-0.01 sets in yellow. We compared these level curves with the superimposed level–1×10^{-3} sets of $|D|$ in white in the upper and middle left and right panels. We found that at all times, both the positive and negative level sets are contained in the simple closed level–1×10^{-3} curve(s) of $|D|$ and both are clustered around the centroids of the

MOTSs of the initial BHs. Although the resolution is not ideal, it follows that there must exist four surfaces around the outside of the union of the level–± 0.01 contours along which the quantities D_r, D_i, $2 * D_r * D_i$, and $D_r^2 - Di^2$ respectively change sign. These four surfaces could be well approximated by the level–1×10^{-3} contours.

In Figures 68–76, we compare the white level–1×10^{-3} set of $|D|$ with the 4 MOTS, as described previously in [50, 51, 31] but plotted for this particular BBH merger for first time here. We find that at early times, the white level–1×10^{-3} set of $|D|$ closely approximates the AHs of the initial BHs while at later times, the AH, formed after the bifurcation, diverges from this level–1×10^{-3} set of $|D|$ quite substantially. However, this level–1×10^{-3} set does mimic closely the MOTSs from the initial BHs and the innermost MOTSs surrounding both BHs.

Therefore, in the binary black hole merger, as displayed in Figures 1–43, the algebraic structure of the Weyl tensor is clearly identified by the level–ε sets of $|D|$, and it is plausible that the level set with $\varepsilon = 1 \times 10^{-3}$ accurately identifies the geometric horizon.

Bibliography

[1] Lars Andersson, Marc Mars, Jan Metzger, and Walter Simon. The time evolution of marginally trapped surfaces. *Classical and Quantum Gravity*, 26(8):085018, Apr 2009.

[2] Lars Andersson, Marc Mars, and Walter Simon. Local existence of dynamical and trapping horizons. *Physical Review Letters*, 95:111102, Sep 2005.

[3] Lars Andersson, Marc Mars, and Walter Simon. Stability of marginally outer trapped surfaces and existence of marginally outer trapped tubes. *Advances in Theoretical and Mathematical Physics*, 12(4):853–888, 08 2008.

[4] Abhay Ashtekar, Christopher Beetle, and Jerzy Lewandowski. Geometry of generic isolated horizons. *Classical and Quantum Gravity*, 19(6):1195–1225, Mar 2002.

[5] Abhay Ashtekar, Miguel Campiglia, and Samir Shah. Dynamical black holes: Approach to the final state. *Physical Review D*, 88:064045, Sep 2013.

[6] Abhay Ashtekar and Gregory J. Galloway. Some uniqueness results for dynamical horizons, 2005.

[7] Abhay Ashtekar and Badri Krishnan. Dynamical horizons: Energy, angular momentum, fluxes, and balance laws. *Physical Review Letters*, 89:261101, Dec 2002.

[8] Abhay Ashtekar and Badri Krishnan. Dynamical horizons and their properties. *Physical Review D*, 68(10), Nov 2003.

[9] Abhay Ashtekar and Badri Krishnan. Isolated and dynamical horizons and their applications. *Living Reviews in Relativity*, 7(1), Dec 2004.

[10] John Baker, Manuela Campanelli, and Carlos O. Lousto. The lazarus project: A pragmatic approach to binary black hole evolutions. *Physical Review D*, 65(4), Jan 2002.

[11] Marsha J. Berger and Joseph Oliger. Adaptive mesh refinement for hyperbolic partial differential equations. *Journal of Computational Physics*, 53(3):484–512, March 1984.

[12] Ivan Booth. Black-hole boundaries. *Canadian Journal of Physics*, 83(11):1073–1099, Nov 2005.

[13] Ivan Booth and Stephen Fairhurst. Isolated, slowly evolving, and dynamical trapping horizons: Geometry and mechanics from surface deformations. *Physical Review D*, 75(8), Apr 2007.

[14] Steven Brandt and Bernd Brügmann. A simple construction of initial data for multiple black holes. *Physical Review Letters*, 78:3606–3609, May 1997.

[15] Alan Coley. Classification of the weyl tensor in higher dimensions and applications. *Classical and Quantum Gravity*, 25(3):033001, Jan 2008.

[16] Alan Coley and S. Hervik. Discriminating the weyl type in higher dimensions using scalar curvature invariants. *General Relativity and Gravitation*, 43:2199–2207, 2011.

[17] Alan Coley and Sigbjørn Hervik. Higher dimensional bivectors and classification of the weyl operator. *Classical and Quantum Gravity*, 27(1):015002, Dec 2009.

[18] Alan Coley, Sigbjørn Hervik, and Nicos Pelavas. Spacetimes characterized by their scalar curvature invariants. *Classical and Quantum Gravity*, 26(2):025013, Jan 2009.

[19] Alan Coley, Nicholas Layden, and David D. McNutt. An invariant characterization of the quasi-spherical szekeres dust models. *General Relativity and Gravitation*, 51(12):164, 2019.

[20] Alan Coley and David D. McNutt. Horizon detection and higher dimensional black rings. *Classical and Quantum Gravity*, 34(3):035008, Jan 2017.

[21] Alan Coley and David D. McNutt. Identification of black hole horizons using scalar curvature invariants. *Classical and Quantum Gravity*, 35(2):025013, Dec 2017.

[22] Alan Coley, David D. McNutt, and Andrey A. Shoom. Geometric horizons. *Physics Letters B*, 771:131–135, Aug 2017.

[23] Alan Coley, Robert Milson, Vojtech Pravda, and Alena Pravdová. Classification of the weyl tensor in higher dimensions. *Classical and Quantum Gravity*, 21(7):L35–L41, Mar 2004.

[24] Alan Coley, Robert Milson, Vojtech Pravda, and Alena Pravdová. Vanishing scalar invariant spacetimes in higher dimensions. *Classical and Quantum Gravity*, 21(23):5519–5542, Nov 2004.

[25] Gregory B. Cook. Three-dimensional initial data for the collision of two black holes. ii. quasicircular orbits for equal-mass black holes. *Physical Review D*, 50(8):5025–5032, Oct 1994.

[26] Olaf Dreyer, Badri Krishnan, Deirdre Shoemaker, and Erik Schnetter. Introduction to isolated horizons in numerical relativity. *Physical Review D*, 67(2), Jan 2003.

[27] Benjamin P. Abbott et al. Binary black hole mergers in the first advanced ligo observing run. *Physical Review X*, 6(4), Oct 2016.

[28] Benjamin P. Abbott et al. Observation of gravitational waves from a binary black hole merger. *Physical Review Letters*, 116:061102, Feb 2016.

[29] Frank Löffler et al. The einstein toolkit: a community computational infrastructure for relativistic astrophysics. *Classical and Quantum Gravity*, 29(11):115001, May 2012.

[30] Richard A. Matzner et al. Geometry of a black hole collision. *Science*, 270(5238):941–947, Nov 1995.

[31] Christopher Evans, Deborah Ferguson, Bhavesh Khamesra, Pablo Laguna, and Deirdre Shoemaker. Inside the final black hole: Puncture and trapped surface dynamics, 2020.

[32] Eric Gourgoulhon and José Luis Jaramillo. A 3+1 perspective on null hypersurfaces and isolated horizons. *Physics Reports*, 423(4-5):159–294, Feb 2006.

[33] Anshu Gupta, Badri Krishnan, Alex B. Nielsen, and Erik Schnetter. Dynamics of marginally trapped surfaces in a binary black hole merger: Growth and approach to equilibrium. *Physical Review D*, 97(8):084028, Apr 2018.

[34] José Louis Jaramillo, Rodrigo P. Macedo, Philipp Mösta, and Luciano Rezzolla. Towards a cross-correlation approach to strong-field dynamics in Black Hole spacetimes. *AIP Conference Proceedings*, 1458(1):158–173, 2012.

[35] José Luis Jaramillo. An introduction to local black hole horizons in the 3+1 approach to general relativity. *International Journal of Modern Physics*, 20(11), 2011.

[36] José Luis Jaramillo, Marcus Ansorg, and Nicolas Vasset. Application of initial data sequences to the study of black hole dynamical trapping horizons. *AIP Conference Proceedings*, 1122(1):308–311, May 2009.

[37] José Luis Jaramillo, Rodrigo P. Macedo, Philipp Mösta, and Luciano Rezzolla. Black-hole horizons as probes of black-hole dynamics. I. Post-merger recoil in head-on collisions. *Physical Review D*, 85:084030, Apr 2012.

[38] José Luis Jaramillo, Rodrigo P. Macedo, Philipp Mösta, and Luciano Rezzolla. Black-hole horizons as probes of black-hole dynamics. II. Geometrical insights. *Physical Review D*, 85:084031, Apr 2012.

[39] David Kastor and Jennie Traschen. Cosmological multi-black-hole solutions. *Physical Review D*, 47(12):5370–5375, Jun 1993.

[40] Jerzy Lewandowski and Tomasz Pawlowski. Quasi-local rotating black holes in higher dimension: geometry. *Classical and Quantum Gravity*, 22(9):1573–1598, Apr 2005.

[41] David D. McNutt and Alan Coley. Geometric horizons in the kastor-traschen multi-black-hole solutions. *Physical Review D*, 98(6), Sep 2018.

[42] David D. McNutt, Malcolm MacCallum, Daniele Gregoris, Adam Forget, Alan Coley, Paul-Christopher Chavy-Waddy, and Dario Brooks. Cartan invariants and event horizon detection, extended version, 2017.

[43] Robert Milson, Alan Coley, Vojtech Pravda, and Alena Pravdová. Alignment and algebraically special tensors in lorentzian geometry. *International Journal of Geometric Methods in Modern Physics*, 02(01):41–61, Feb 2005.

[44] Philipp Mösta, Lars Andersson, Jan Metzger, Béla Szilágyi, and Jeffrey Winicour. The merger of small and large black holes. *Classical and Quantum Gravity*, 32(23):235003, Dec 2015.

[45] Ken-ichi Nakao, Tetsuya Shiromizu, and Sean A. Hayward. Horizons of the kastor-traschen multi-black-hole cosmos. *Physical Review D*, 52:796–808, Jul 1995.

[46] Roger Penrose. Gravitational collapse and space-time singularities. *Physical Review Letters*, 14:57–59, Jan 1965.

[47] Daniel Pook-Kolb, Ofek Birnholtz, José Luis Jaramillo, Badri Krishnan, and Erik Schnetter. Horizons in a binary black hole merger i: Geometry and area increase, 2020.

[48] Daniel Pook-Kolb, Ofek Birnholtz, José Luis Jaramillo, Badri Krishnan, and Erik Schnetter. Horizons in a binary black hole merger ii: Fluxes, multipole moments and stability, 2020.

[49] Daniel Pook-Kolb, Ofek Birnholtz, Badri Krishnan, and Erik Schnetter. Existence and stability of marginally trapped surfaces in black-hole spacetimes. *Physical Review D*, 99(6):064005, Mar 2019.

[50] Daniel Pook-Kolb, Ofek Birnholtz, Badri Krishnan, and Erik Schnetter. Interior of a binary black hole merger. *Physical Review Letters*, 123(17), Oct 2019.

[51] Daniel Pook-Kolb, Ofek Birnholtz, Badri Krishnan, and Erik Schnetter. Self-intersecting marginally outer trapped surfaces. *Physical Review D*, 100(8), Oct 2019.

[52] Vaishak Prasad, Anshu Gupta, Sukanta Bose, Badri Krishnan, and Erik Schnetter. News from horizons in binary black hole mergers, 2020.

[53] Erik Schnetter, Scott H. Hawley, and Ian Hawke. Evolutions in 3d numerical relativity using fixed mesh refinement. *Classical and Quantum Gravity*, 21(6):1465–1488, Feb 2004.

[54] Erik Schnetter, Badri Krishnan, and Florian Beyer. Introduction to dynamical horizons in numerical relativity. *Physical Review D*, 74(2):024018, Jul 2006.

[55] Hans Stephani, Dietrich Kramer, Malcolm MacCallum, Cornelius Hoenselaers, and Eduard Herlt. *Exact solutions of Einstein's field equations, second edition.* Cambridge University Press; Cambridge, 2003.

[56] Jonathan Thornburg. Finding apparent horizons in numerical relativity. *Physical Review D*, 54:4899–4918, Oct 1996.

[57] Jonathan Thornburg. Event and apparent horizon finders for 3+1 numerical relativity, 2005.